12-2012

Charge-Lattice-Spin Interactions in Molecule-Based Magnets

Tatiana Vladimir Brinzari
tbrinzar@utk.edu

To the Graduate Council:

I am submitting herewith a dissertation written by Tatiana Vladimir Brinzari entitled "Charge-Lattice-Spin Interactions in Molecule-Based Magnets." I have examined the final electronic copy of this dissertation for form and content and recommend that it be accepted in partial fulfillment of the requirements for the degree of Doctor of Philosophy, with a major in Chemistry.

Janice L. Musfeldt, Major Professor

We have read this dissertation and recommend its acceptance:

Ziling Xue, Robert J. Harrison, Veerle M. Keppens

Accepted for the Council:
Carolyn R. Hodges

Vice Provost and Dean of the Graduate School

(Original signatures are on file with official student records.)

Charge-Lattice-Spin Interactions in Molecule-Based Magnets

A Dissertation Presented for the

Doctor of Philosophy Degree

The University of Tennessee, Knoxville

Tatiana Vladimir Brinzari

December 2012

Acknowledgments

I would like to express deep and sincere gratitude to my advisor Professor Janice L. Musfeldt whose guidance, advice, patience and encouragement had an invaluable input in my PhD degree and my professional growth. Her dedication to students, care and support helped me in all the time of my graduate studies at the University of Tennessee.

I am grateful to Professors Ziling Xue, Robert Harrison and Veerle Keppens for serving on my committee and reviewing my work.

I wish to acknowledge all the members of our research group: Jinbo Cao, Ram Rai, Luciana Vergara, Xiaoshan Xu, Jessica White, Qi Sun, Özge Günaydın-Şen, Peng Chen, Brian Holinsworth, Ken O'Neal, Dipanjan Mazumdar and Henok Mikre for their help, encouragement, and collaboration. I am especially indebted to Xiaoshan Xu and Luciana Vergara who generously spent their time teaching me a lot of physics. Their patience and support are very much appreciated.

I would also like to thank John Schlueter, Jamie Manson, John Singleton, Mike Whangbo, Jason Haraldsen, Alexander Litvinchuk, Dmitry Smirnov, Li-Chun Tung, Yongjie Wang, Jia Liu, Younghee Kim, Greg Halder and Chuan Tian for the excellent collaboration during these years.

I am grateful to all the faculty and staff of the Chemistry Department who shared their knowledge with me and helped in variety of ways during my graduate program.

I also thank the American Physical Society, the American Chemical Society,

Wiley-VCH, Macmillan Publishers Ltd., Springer Science and Business Media, IOP Publishing Ltd., Elsevier, and the corresponding authors for the kind permission to reproduce selected figures from their articles.

Finally, I would like to express special thanks to my family for their support and encouragement throughout my study.

Abstract

Many of the most attractive properties of multifunctional materials can be traced to the competition between charge, structure, and magnetism. The discovery that these interactions can be tuned with various physical stimuli has accelerated interest in their behavior under extreme conditions. In this dissertation I present a spectroscopic investigation of several model molecule-based magnets under external stimuli of magnetic field and temperature. The compounds of interest include $M^{II}[N(CN)_2]_2$ (M=Mn, Co) and $[Ru_2(O_2CMe)_4]_3[Cr(CN)_6]$. These materials are attractive for their subtle interplay between electronic, magnetic and structural degrees of freedom offering both physical property tunability and models with which to carry out fundamental studies of coupling phenomena. The vibrational properties of $Mn[N(CN)_2]_2$ reveal the magnetoelastic coupling through the quantum critical transition at 30.4 T that drives the system from the canted antiferromagnetic to the fully polarized state. The local lattice distortions, manifested in systematic phonon frequency shifts, suggest a combined MnN_6 octahedra distortion + counter-rotation mechanism that reduces antiferromagnetic interactions and accommodates the developing field-induced state. Work on $Co[N(CN)_2]_2$ combines high field Raman and infrared spectroscopies to explore the effect of the chemical tuning on lattice dynamics and coupling processes in a ferromagnet. In addition to a large anisotropy, our studies uncover electron-phonon coupling as a field-driven avoided crossings of the low-lying Co^{2+} electronic excitation with the ligand phonons and a magnetoelastic effect that signals a flexible local CoN_6

environment under external field. Finally, we employ vibrational spectroscopies to probe spin-lattice interactions in the $[Ru_2(O_2CMe)_4]_3[Cr(CN)_6]$ metamagnet. In applied field, correlation between the vibrational response, the displacement patterns, and local lattice distortions reveals magnetoelastically-active $[Cr(CN)_6]^{3-}$ octahedral units and rigid $[Ru_2(O_2CMe)_4]^{+}$ paddle wheel dimers as the system is driven away from the antiferromagnetic ground state. At the same time, variable temperature studies show pronounced changes in modes connected with the $[Cr(CN)_6]^{3-}$ octahedra, demonstrating the overall softness of this moiety and its readiness to adapt to a new physical environment. These findings deepen our understanding of coupling in multifunctional materials and demonstrate the tunability of competing interactions under extreme conditions.

Contents

List of Tables

List of Figures

List of Symbols and Abbreviations

α	Absorption coefficient
α^p	Molecular polarizability
B	Magnetic field (T)
$B(\omega)$	Source intensity
c	Speed of light, $c = 2.99{\cdot}10^8$ m·s^{-1}
c_{ij}	Elastic constants
D	Anisotropy
D	Displacement field or dimensionality
D_e	Dissociation energy
d	Sample thickness
E	Energy or electric field
ε	Dielectric function
ε_0	Vacuum permittivity, $\varepsilon_0 = 8.85{\cdot}10^{-12}$ F·m^{-1}
g	g-factor
$\mathcal{H}$	Hamiltonian
H	Magnetic field strength (A·m^{-1})
h	Planck constant, $h = 6.62{\cdot}10^{-34}$ J·s
h_s	Sample concentration
I	Intensity
J	Exchange constant

j	Current density
κ	Extinction coefficient
k	Force constant or wavevector
k_B	Boltzmann constant, $k_B = 1.38{\cdot}10^{-23}$ J·K^{-1}
λ	Magnetostriction
λ'	Coupling constant
λ_w	Wavelength
l	Sample length
M	Magnetization or transition moment integral
M	Metal ion
m	Mass or order of diffraction
μ	Dipole moment or magnetic permeability
μ'	Reduced mass
μ_B	Bohr magneton, $\mu_B = 9.27{\cdot}10^{-24}$ J·T^{-1}
μ_0	Vacuum permeability, $\mu_0 = 4\pi \cdot 10^{-7}$ H·m^{-1}
$\widetilde{N}$	Complex index of refraction
N	Number of atoms or slits
n	Index of refraction or vibrational quantum number
ν	Frequency (s^{-1})
P	Polarization
Q	Vibrational coordinate
Q_i^0	Vibrational amplitude
R	Reflectance
R_s	Grating resolution
ρ^{ext}	Charge density
r	Distance/bond length

σ	Optical conductivity
S	Spin angular momentum
$\mathcal{T}$	Transmittance
T	Temperature
T_{C}	Transition temperature of ferromagnetism
T_{N}	Transition temperature of antiferromagnetism
T_{SP}	Spin-Peierls transition temperature
t	Time
V	Volume
U	Potential energy
x	Displacement from equilibrium position
z	Number of nearest neighbors
ψ	Wavefunction
ω	Wavenumber (cm^{-1}) or angular frequency
ACS	American Chemical Society
AFM	Antiferromagnetic
BEDT-TTF	Bis(ethylendithio)tetrathiafulvalene
dca	Dicyanamide
2,3-dmpyH	2,3-dimethylpyridinium
DTA	Dithiazolyl
DTDA	Dithiadiazolyl
DTGS	Deuterated triglycine sulfate
EM	Electromagnetic radiation
ESR	Electron spin resonance
FM	Ferromagnetic
FTIR	Fourier transform infrared

H_2TPP	Tetraphenylporphyrin
IR	Infrared
LANL	Los Alamos National Laboratory
LIESST	Light-induced excited spin-state trapping
MB	Mößbauer spectroscopy
MCT	Mercury cadmium telluride
Me	Methyl group (-CH_3)
MW	Microwave
NHMFL	National High Magnetic Field Laboratory
NMR	Nuclear magnetic resonance
PAC	Perturbed angular correlation
PM	Paramagnetic
SF	Spin-flop
tcm	Tricyanomethanide
TCNE	Tetracyanoethylene
tmphen	3,4,7,8-tetramethyl-1,10-phenanthroline
TTF	Tetrathiafulvalene
UPS	Ultraviolet photoelectron spectroscopy
UV-Vis	Ultraviolet-visible
XAFS	X-ray absorption fine structure
XPS	X-ray photoelectron spectroscopy

Chapter 1

Introduction: Molecule-Based Solids as Models for Novel Magnetism and Functionality

Magnetic materials have fascinated mankind since their discovery by the ancient Greeks and the early application in a "South pointing" compass by the Chinese. [1,2] The technological importance and ubiquitous use of magnets in telecommunication, magnetic recording, acoustic devices and medical imaging prompts contemporary research with focus on enhancement of existing materials and search for novel compounds with important magnetic and unique cooperative physical properties.

Historically, the field of magnetic materials has been confined to metals, their alloys and/or metal oxides. These so-called classical magnets are composed of atoms or ions of the transition- or lanthanide metals, for instance Fe, Co, Fe_3O_4, CrO_2, $Nd_2Fe_{14}B$, and have their active spins residing on the corresponding d- or f- orbitals. [2] Close proximity of magnetic centers gives rise to strong magnetic interactions governed by direct exchange, superexchange, and dipole-dipole interactions.

These materials are technologically important due to the very high magnetic ordering temperatures however, they are mechanically brittle, heavy, insoluble and require energy-expensive fabrication methods. [2, 3]

Molecule-based magnets are an expanding class of materials that are fundamentally different from conventional metal- and oxide-based magnets. These systems are constructed from the discrete molecular units/components assembled together by ionic, covalent, hydrogen bonding and/or van der Waals interactions. [3–5] The extraordinary richness of molecular chemistry along with simpler solution-based synthetic methodologies provide unprecedented opportunities for manipulation and design of specific materials with desired magnetic properties. Moreover, the latter can be extended to combine magnetic phenomena with low density, solubility, mechanical flexibility, porosity, biocompatibility, optical, and electrical properties thus enabling the development of advanced multifunctional devices. [2–6]

Since the discovery of bulk magnetism in molecular solids, a vast number of compounds with intriguing crystal architectures and interesting properties have been revealed. [2,4–6] These novel magnets span from purely organic compounds with unpaired electron spins localized on p-orbitals to hybrid organic/inorganic complexes where electrons reside on p and/or d-levels and to d-orbital-based inorganic coordination compounds. The hybrid materials can be generally classified into two main groups. In the first, metal ions and the organic moieties carry unpaired electrons and contribute to the observed magnetism. In the second, ligands are not intrinsically magnetic and act as effective superexchange pathways between spin-carrying metal centers. Extensive research in magnetic phenomena of molecular species has led to realization of 0-dimensional (0D), 1D, 2D, 3D magnetically ordered systems (i.e. ferromagnets, ferrimagnets, antiferromagnets, weak ferromagnets) enabling the discovery of (i) room temperature magnetism, [7–11] (ii) photoinduced magnetism, [12,13] (iii)

materials with spin-crossover and charge-transfer induced spin transitions, [14–18] (iv) compounds with large negative magnetization, [19, 20] (v) single-molecule and single chain magnets, spin ladders (Fig. 1.1). [21–27] Many of these systems are particulary attractive for fundamental studies of quantum magnetism. From being a curiosity and challenge for chemists, the field of molecule-based magnetism has grown into an interdisciplinary area were collaboration between chemists, physicists and material scientists is essential to design, characterize and apply novel compounds displaying new types of cooperative physical phenomena.

A large class of solids consists of purely organic-based magnets fabricated from stable organic radicals. The most studied examples are presented by nitronyl nitroxide, dithiadiazolyl/dithiazolyl, and verdazyl families of radicals (Fig. 1.2). [4, 5, 28] The rich chemistry of organic substitute groups led to discovery of a wide spectrum of magnetic systems exhibiting ferromagnetism, antiferromagnetism, weak ferromagnetism, geometric frustration, and the spin-Peierls transition. [4,5,28] In addition to organic magnets, materials that combine both organic components and metal ions received considerable attention after the discovery of $[Fe^{III}(C_5Me_5)_2][TCNE]$ - the 0D molecule-based ferromagnet with a 4.8 K ordering temperature. [29, 30] The subsequent search for cooperative magnetism in the TCNE (TCNE = tetracyanoethylene) family of compounds resulted in the discovery of $V(TCNE)_x{\cdot}y(CH_2Cl_2)$ ($x \simeq 2$, $y \simeq 1/2$) - an organic-based room temperature magnet with $T_C \simeq 400$ K (Fig. 1.1(a)). [10,11] A series of $M(TCNE)_x$ (M = Mn, Fe, Co, Ni) materials as well numerous other compounds employing TCNE radical anion (for instance, [MnTPP][TCNE]·solvent family, H_2TPP = tetraphenylporphyrin) also display interesting magnetic properties. [5, 6] Finally, inorganic coordination compounds, especially the Prussian blues, constitute an important class of magnetic solids. This large family of materials with general formula $M_x[M'(CN)_6]_y{\cdot}nH_2O$ (Fig. 1.2) displays a variety of physical

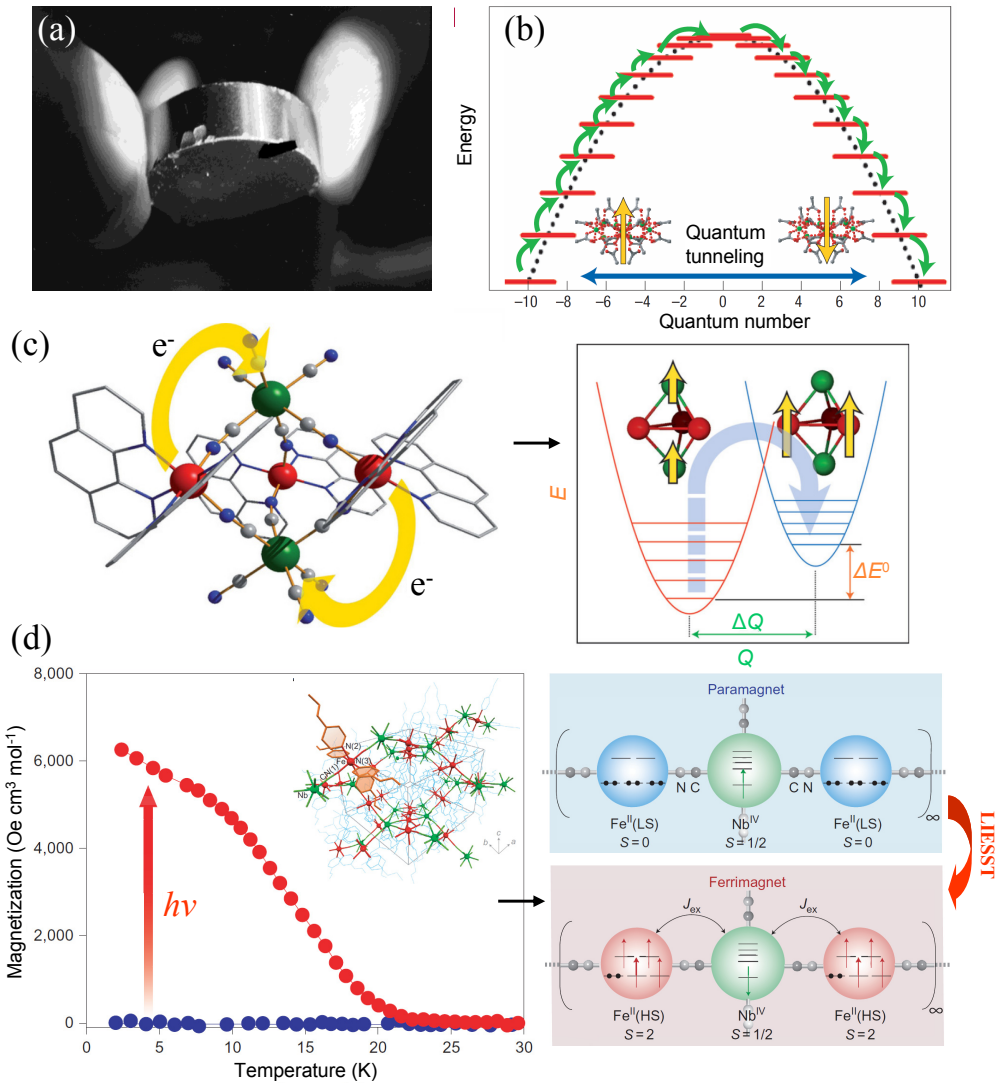

Figure 1.1: Representative examples of magnetic phenomena in molecule-based materials. (a) Room temperature magnet $V(TCNE)_x$ attracted to Co_5Sm magnet. Reprinted (Fig. 2) with permission from Ref. [11] [K. I. Pokhodnya *et al.*, Adv. Mater. **12**, 410 (2000)]. Copyright (2000) WILEY-VCH. (b) Quantum effects in single-molecule magnet $[Mn_{12}O_{12}(O_2CCH_2C(CH_3)_3)_{16}(CH_3OH)_4]$. Reprinted (Fig. B1a) by permission from Macmillan Publishers Ltd: [Nature Materials, http://www.nature.com/nmat], Ref. [25] [L. Bogani and W. Wernsdorfer, Nature Mater. **7**, 179 (2008)]. Copyright (2008). (c) A schematic of charge-transfer induced spin transition in $[Fe(tmphen)_2]_3[Os(CN)_6]_2$. [16, 17] Reprinted (Fig. 1, 2) by permission from Macmillan Publishers Ltd: [Nature Chemistry, http://www.nature.com/nchem], Ref. [17] [R. Sessoli, Nature Chem. **2**, 346 (2010)]. Copyright (2010). (d) Light induced spin-crossover magnetism in $Fe_2[Nb(CN)_8](4\text{-pyridinealdoxime})_8{\cdot}2H_2O$). Reprinted (Fig. 1c, 3a, 4b) by permission from Macmillan Publishers Ltd: [Nature Chemistry, http://www.nature.com/nchem], Ref. [18] [S. Ohkoshi, *et al.*, Nature Chem. **3**, 564 (2011)]. Copyright (2011).

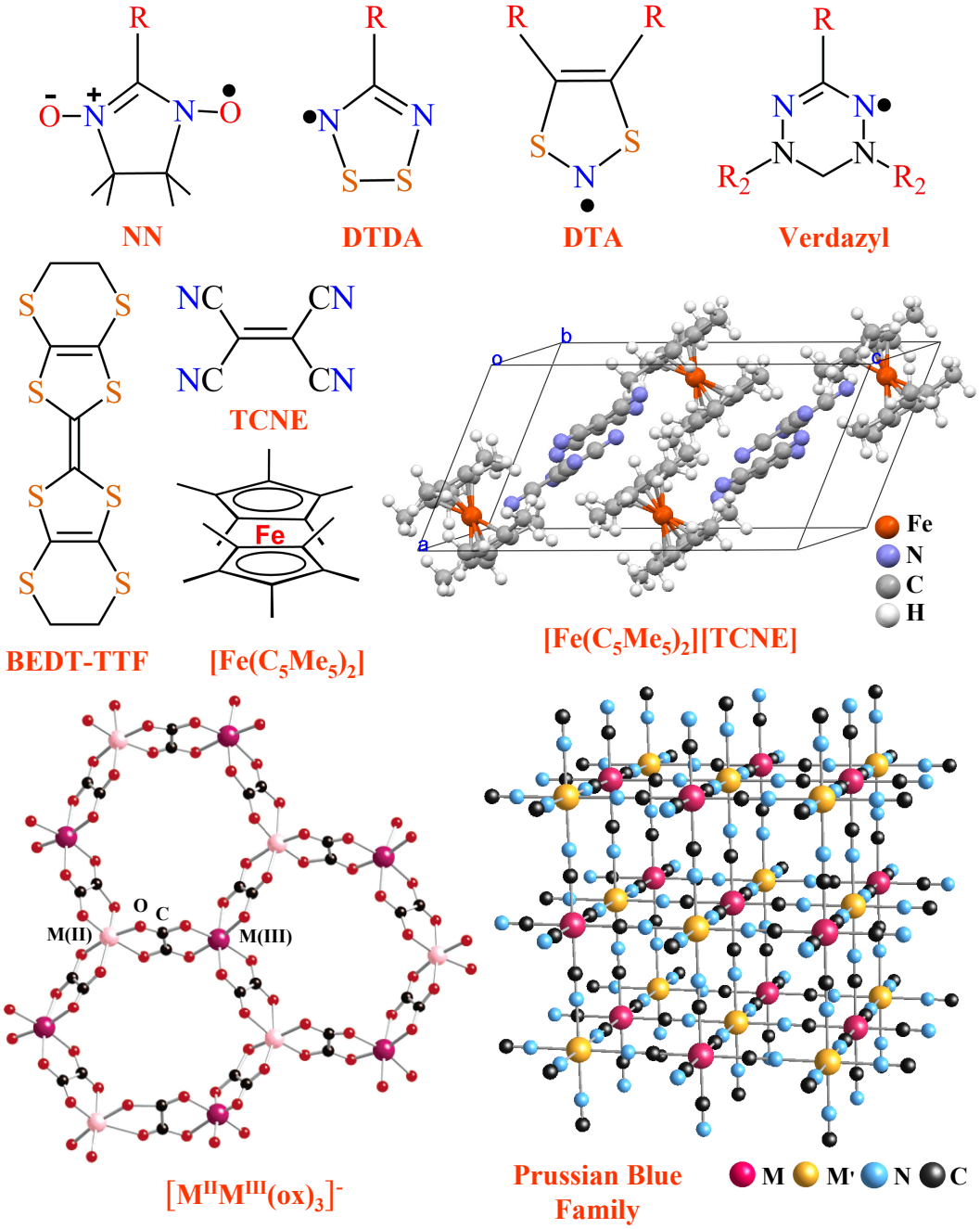

Figure 1.2: Examples of molecular building blocks and representatives of molecule-based magnets. NN = nitronyl nitroxide, DTDA = dithiadiazolyl, DTA = dithiazolyl, TCNE = tetracyanoethylene, BEDT-TTF = bis-(ethylendithio)tetrathiafulvalene. [4, 5, 30–32] $[M^{II}M^{III}(ox)_3]^-$ structure: Reprinted with permission from Ref. [31] [K. S. Min *et al.*, Inorg. Chem **44**, 8433 (2005)]. Copyright (2004) American Chemical Society.

properties that can be tuned with metal substitution. [7,33] Perhaps the most spectacular among these compounds are mix-valent $V^{II/III}[Cr^{III}(CN)_6]_{0.86}\cdot 2.8H_2O$ and $KV^{II}[Cr^{III}(CN)_6]\cdot 2H_2O$ ferrimagnets with magnetically ordered states above room temperature (T_C = 315 and 376 K, respectively). [8,34] Besides rich properties like room temperature magnetism, metamagnetism, photomagnetism, spin-crossover and ferroelectric ferromagnetism, the Prussian blue family also displays a broad spectrum of optical, electrical, and gas storage properties. [7,33,35] Similarly to Prussian blue analogs, the family of mixed metal oxalates $[M^{II}M^{III}(C_2O_4)_3]^-[XR_4]^+$ (M^{II} = Mn, Fe, Co, Ni, Cu; M^{III} = Cr, Fe) attracted a lot of attention as they display ferro- and ferrimagnetic ordering with T_C between 6 and 48 K. [5, 36, 37] Importantly, substitution of electronically "inactive" organic cations $[XR_4]^+$ with other functional groups offers unique opportunities to couple several desired properties for instance, magnetic and electrical phenomena. Such a combination of magnetic and electronic properties was realized in $[BEDT\text{-}TTF]_3[MnCr(C_2O_4)_3]$ (BEDT-TTF = bis(ethylendithio)tetrathiafulvalene) composed of sheets of ferromagnetic bimetalic oxalato complex and layers of conducting BEDT-TTF cations. [38] This discovery of ferromagnetic organic metal opened an intriguing class of molecule-based ferromagnetic conductors. [38,39] Taken together, these examples of molecule-based magnets varying from organic to hybrid, to inorganic materials demonstrate enormous opportunities in direct engineering of novel materials with predefined chemical and physical properties.

Despite a growing number of molecule-based magnets and their extensive investigation, the comprehensive understanding of their structure-property relationships is still far from complete. The targeted fabrication of next generation magnetic devices with tunable properties and coupled functionality requires fundamental investigation of the charge-lattice-spin interactions. In fact, the interplay between electronic,

magnetic, lattice and/or orbital degrees of freedom is at the heart of many exotic properties of multifunctional materials. As an example, in organic charge transfer salts, iron chalcogenides, and transition metal oxides like manganites or cobaltites, the existence of multiple competing interactions gives rise to rich phase diagrams where close proximity or simultaneous occurrence of, for instance, magnetic, charge ordered insulating, metallic, and superconducting states offers unprecedented opportunities to tune properties and produce novel phenomena. [40–43] Figure 1.3 provides several examples of phase diagrams for representative materials displaying strong coupling over various degrees of freedom. [41, 44, 45]

Many of these complex materials exhibit quantum critical points - one of the subjects of this work, although our interest is in the magnetically driven phase transitions. An example of such a field-driven transition is shown in Fig. 1.4(a) for $BaCuSi_2O_6$ quantum magnet where the applied field acts to reduce the singlet-triplet spin gap giving rise to novel magnetic order above the quantum critical field B_c. [46] Besides quantum critical transitions, the external field also drives a cascade of phase transformations in a variety of functional materials like, multiferroic oxides. [47–49] Figure 1.4(b) displays an example of $B-T$ phase diagram for $Ni_3V_2O_8$ where competing correlations and near degenerate ground states are tuned with applied field. These examples demonstrate that magnetic field is an important physical variable that induces interesting states and gives rise to exotic phenomena commonly found in extreme environments.

Molecule-based materials offer unique opportunities to investigate the interplay between charge, structure, and magnetism and for bottom-up understanding of their multifunctional behavior. [4, 5, 39] Their richness and flexibility of discrete building blocks are particularly attractive to couple functionality and tune properties by external stimuli like, temperature, pressure and magnetic field. Their low mag-

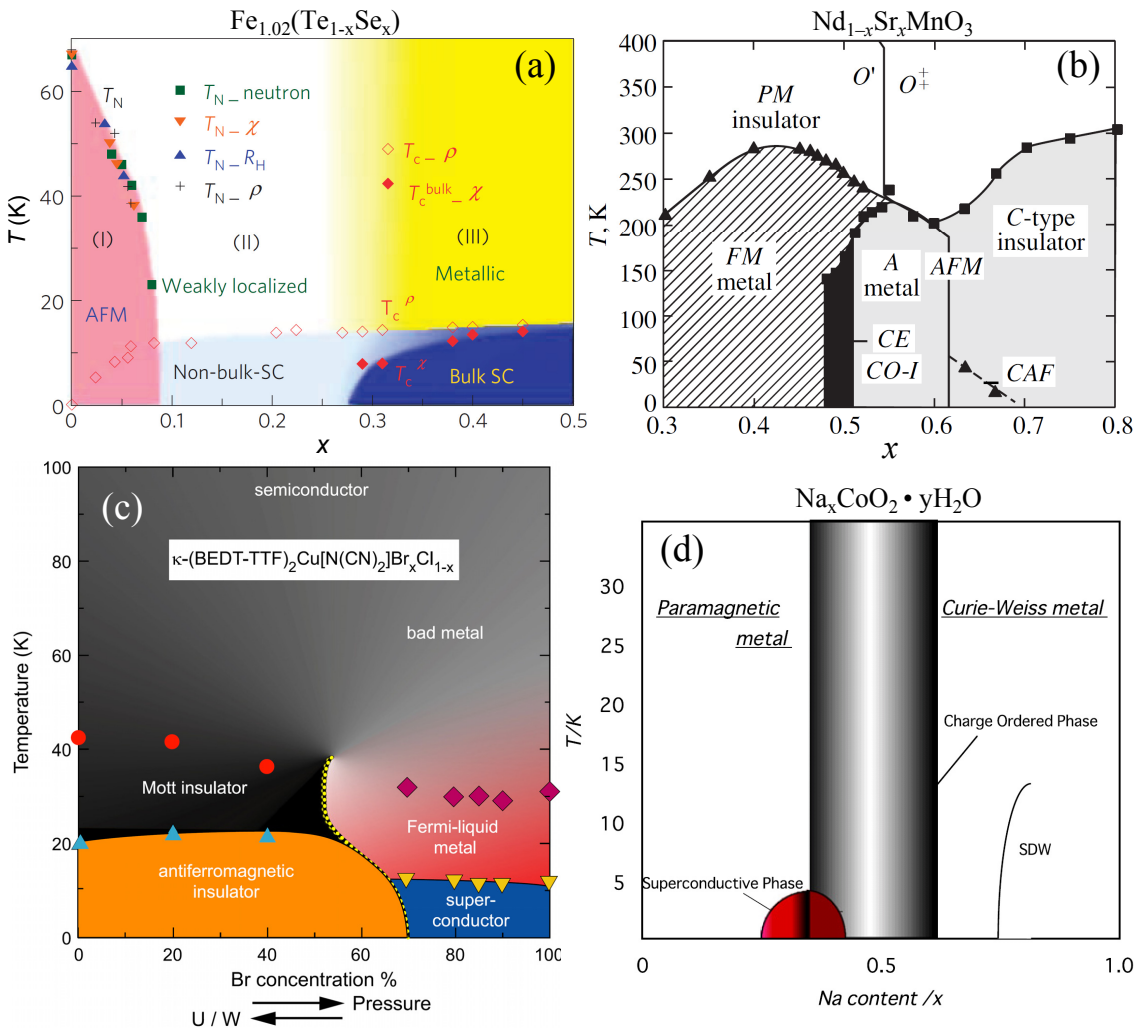

Figure 1.3: Complex phase diagrams for materials with strong competing interactions and tunable ground states under chemical or physical pressure. (a) $Fe_{1.02}(Te_{1-x}Se_x)$. Reprinted (Fig. 1) by permission from Macmillan Publishers Ltd: [Nature Materials, http://www.nature.com/nmat], Ref. [44] [T. J. Liu *et al*, Nature Mater. **9**, 716 (2010)]. Copyright (2010). (b) $Nd_{1-x}Sr_xMnO_3$. Reprinted (Fig. 8) with permission from Ref. [45] [S. M. Dunaevskiĭ, Phys. Solid State, **46**, 193 (2004)]. Copyright (2004) MAIK Nauka/Interperiodica with permission from Springer Science and Business Media. (c) κ-$(BEDT\text{-}TTF)_2Cu[N(CN)_2]Br_xCl_{1-x}$. Reprinted (Fig. 6) with permission from Ref. [41] [M. Dressel, J. Phys.: Condens. Matter **23**, 293201 (2011)]. Copyright (2011) IOP Publishing Ltd. (d) $Na_xCoO_2{\cdot}yH_2O$. Reprinted (Fig. 1) with permission from Ref. [50] [M. Ohkawa, Physica B **405**, 3057 (2010)]. Copyright (2010) Elsevier.

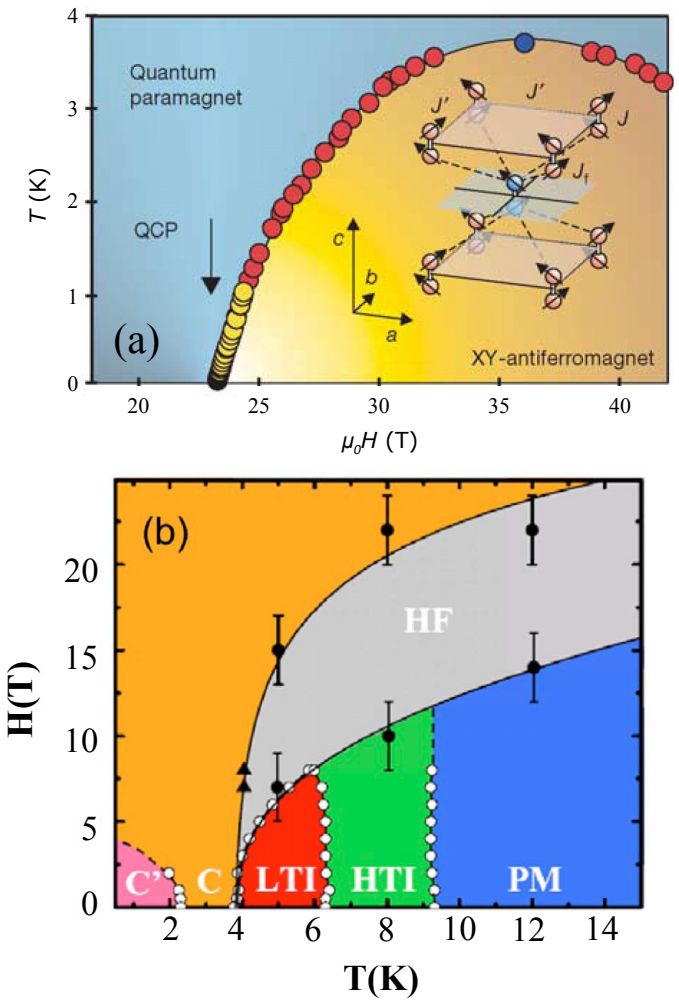

Figure 1.4: $B-T$ phase diagrams for selected materials emphasizing their complex magnetic transitions in the low temperature regime. (a) $BaCuSi_2O_6$ quantum magnet. Reprinted (Fig. 1) by permission from Macmillan Publishers Ltd: [Nature Materials, http://www.nature.com/nature], Ref. [46] [S. E. Sebastian *et al*, Nature **441**, 617 (2006)]. Copyright (2006). (b) $Ni_3V_2O_8$ multiferroic. Reprinted (Fig. 2b) with permission from Ref. [47] [R. C. Rai *et al.*, Phys. Rev. B **74**, 235101 (2006)]. Copyright (2006) by the American Physical Society.

netic energy scales are well-suited to investigating field-driven phase transitions and charge-lattice-spin interactions at moderate fields. [51–54] Taken together, these characteristics make molecular magnetic solids highly attractive for investigation of microscopic aspects of structure-property relationships in complex systems. Moreover, molecule-based magnets can be used as model systems to test new theories and provide fundamental insight into the behavior of other multifunctional materials, like oxides where higher energy scales render similar physical processes inaccessible to conventional powered and pulsed magnets. As an example, the moderate exchange energies of copper halide spin ladder (2,3-dmpyH)$_2$CuBr$_4$ (2,3-dmpyH = 2,3-dimethylpyridinium) provide an elegant way to gain insight into the fundamental physics of copper oxide materials and thus deepen our understanding of their quantum spin behavior and high temperature superconductivity. [27, 55]

The structure-property relationships in materials of interest are typically probed by a variety of complementary techniques. A combination of bulk magnetic, electrical, and structural probes, such as magnetization, specific heat, resistivity, x-ray/neutron diffraction, and magnetostriction measurements are generally employed to map out different phases and establish correlations with chemical and physical tuning. These probes however, provide only an average macroscopic response. As an example, magnetostriction measurements bring insight into the behavior of the lattice constants in different magnetic regimes however, lack information on the microscopic signatures of magneto-structural correlations and their role in fundamental phase transitions and quantum critical phenomena. In contrast, investigation of magnetoelastic interactions with more sensitive microscopic methods using for instance, diverse spectroscopic techniques, provides information not only on local structure deformations and atomic displacements but also reveals dynamic nature of this interaction. The profound investigation of the local lattice interactions and mi-

croscopic aspects of the charge-lattice-spin coupling will bring deeper understanding of the foundational behavior of complex matter, and moreover will help to design and manipulate the technologically important materials and their properties.

Spectroscopy is a versatile and powerful tool for the investigation of physical phenomena of complex materials. It offers studies over a broad energy range and probes a variety of elementary and collective excitations. Optical methods play a key role in investigation of electronic, magnetic, lattice and orbital degrees of freedom and provide crucial information on both, static and dynamic effects. As an example, crystal field effects, charge and orbital ordering, short-range correlations and evolution of new phases, magnetic, ferroelectric and structural transitions are widely studied by optical techniques. [16, 40, 41, 56–63] Furthermore, coupling phenomena for instance, electron-phonon, crystal field-magnon and magnon-phonon interactions are of fundamental interest as they provide insight into intrinsic properties of solids. [40,61,62,64,65] Finally, combining optical spectroscopy with temperature, pressure, electric and magnetic fields opens new possibilities to control and manipulate delicate balance between competing states, tune system properties, and elucidate microscopic aspects of structure-property relationships.

In this dissertation, I employ infrared and Raman spectroscopy for investigation of several 3D molecule-based magnets as a function of temperature and magnetic field. Compounds of interest include $M^{II}(dca)_2$ (M = Mn, Co, dca = dicyanamide, $N(CN)_2^-$) and $[Ru^{II/III}{}_2(O_2CMe)_4]_3[Cr^{III}(CN)_6]$ magnets. The scientific questions concentrate on lattice dynamics and charge-lattice-spin interactions in these materials. Our findings are summarized in Table 1.1.

$Mn(dca)_2$, $Co(dca)_2$, and $[Ru_2(O_2CMe)_4]_3[Cr(CN)_6]$ attracted our attention as systems that display a series of field and temperature driven transitions including antiferromagnetic, ferromagnetic, and ferrimagnetic ordering transitions, a spin-flop,

Table 1.1: Scientific problems and important findings in this dissertation

Model Compound	Scientific Problem	Our Findings
$Mn(dca)_2$	• Quantum critical transition • Spin-lattice coupling: a) Field-driven quantum phase transition from AFM → PM state b) Temperature-driven AFM → PM transformation at $T_N = 15.85$ K	• Quantum critical point at 30.4 T, $J \simeq -1.0$ K, completed $B-T$ phase diagram • Lattice dynamics analysis: calculated frequencies and assignment of vibrational modes • Magnetoelastic interactions through the quantum phase transition: MnN_6 O_h distortions + octahedra counter-rotation → to accommodate new developing magnetic state • No phonon sensitivity to 15.85 K Néel transition → inherently weak spin-phonon coupling
$Co(dca)_2$	• Chemical tuning • Co^{2+} zero-field splitting • Charge-lattice-spin coupling: a) High field tuning of competing interactions b) Temperature-driven FM → PM transition at $T_C = 9$ K	• Large Co^{2+} anisotropy, $D = 12 \pm 4$ cm^{-1} • Vibrational excitation profile similar to Mn analog with overall harder lattice • Electron phonon coupling: field-driven avoided crossings of Co^{2+} excitation with phonons • Magnetoelastic interactions at high field: local structure deformations of Co^{2+} environment • Intrinsically weak spin-phonon coupling → no vibrational sensitivity to 9 K Curie temperature
$(Ru_2)_3Cr$	• Spin-lattice interactions: a) Magnetically-driven AFM → Metamagnetic → SF/PM transitions b) AFM → PM phase transition at $T_C = 33$ K • Low temperature lattice dynamics	• Intersublattice coalescence transition displays a purely magnetic origin • Flexible lattice in high magnetic fields away from the AFM state: magnetoelastically-active $[Cr(CN)_6]^{3-}$ octahedral blocks and rigid $[Ru_2(O_2CMe)_4]^+$ paddle wheel dimers • No signatures of spin-phonon interactions thought the 33 K magnetic ordering transition • Variable temperature investigation affirms overall flexibility of Cr^{3+} environment → adaptable $[Cr(CN)_6]^{3-}$ under external stress • Strengthened intersublattice hydrogen-bonding-like interactions at low temperature may foster lattice stabilization

FM-ferromagnetic, AFM-antiferromagnetic, PM-paramagnetic, SF-spin-flop
$(Ru_2)_3Cr = [Ru_2(O_2CMe)_4]_3[Cr(CN)_6]$

a quantum phase transition, and a metamagnetic transformation with a spin coalescence of the two interpenetrating lattices. These materials display a subtle interplay between electronic, magnetic and structural degrees of freedom that can be tuned by chemical or physical means and are therefore well suited to extended investigations of competing interactions. Spectroscopic investigation is employed to provide a direct probe of the lattice dynamics in these chemically related compounds, to explore extensive coupling phenomena, and to reveal the role of the local structural effects on magnetic properties and exchange coupling between spin carriers. The molecule-based magnets of interest are used as model compounds to acquire a comprehensive view of the charge-lattice-spin interactions and get fundamental insight into the microscopic aspects of these phenomena.

The remainder of the dissertation is organized as follows: the second Chapter presents a literature survey of model molecule-based magnets, fundamentals of magnetoelastic coupling and its manifestation in complex materials. Chapter 3 discusses the basics of infrared and Raman techniques, interaction of light with solids, and the sample preparation and characterization. Chapter 4 presents our investigation and results on $Mn(dca)_2$ magnet with focus on quantum critical transition and magneto-structural correlations. Chapter 5 is devoted to charge-lattice-spin interactions in $Co(dca)_2$ ferromagnet. Chapter 6 details the magneto-vibrational and temperature investigation of $[Ru_2(O_2CMe)_4]_3[Cr(CN)_6]$ compound, with the goal of understanding the lattice dynamics, intersublattice interaction, and interplay between magnetic and structural degrees of freedom. Finally, Chapter 7 summarizes my work.

Chapter 2

Literature Survey

2.1 $M(dca)_2$ and $[Ru_2(O_2CMe)_4]_3[Cr(CN)_6]$ Molecule-Based Magnets

2.1.1 Dicyanamide ligand and the family of $M(dca)_2$ compounds

For an inorganic or hybrid inorganic/organic molecule-based magnet, the contribution to the observed magnetism generally comes from both the metal and organic/inorganic ligand. Metal ions play a role of the spin carriers while nonmagnetic ligands provide effective superexchange paths between metal magnetic centers.[1] The selection of an appropriate intermediary linkage that controls the superexchange between metal sites is the key step in the design of molecular magnetic solids. In a simplest scenario, shorter ligands with greater conjugation provide stronger coupling between metal centers. [66] Perhaps, one of the most widely used ligands in the field of molecular magnetism is the cyanide, CN^-. The most famous polycyano complexes

[1] Here, we only focus on diamagnetic ligands that do not carry unpaired spins.

are Prussian blue analogs $M_x[M'(CN)_6]_y \cdot nH_2O$ where several members of this family were found to be magnetically ordered at temperatures as high as 376 K. [7–9] In addition to cyanide, larger pseudohalide ligands such as dicyanamide (dca = $N(CN)_2^-$) and tricyanomethanide (tcm = $(C(CN)_3^-$) have been attracting a lot of attention. [66–68] These pπ electronic conjugated systems are promising candidates in providing effective exchange pathways between magnetic ions. While both ligands can be used in engineering of molecular magnets, dca-based compounds were shown to posses largely enhanced magnetic properties, as compared to materials build with tcm ligand. The latter is partially due to the shorter M-NCN-M connections offered by dca (Fig. 2.1) relative to longer M-NCCCN-M superexchange pathways achieved with tcm linkage.

A fascinating property of the dca ligand is its ability to coordinate to a metal ion in a variety of ways. Figure 2.1 displays several different coordination modes of the dca. [67] Monodentate and bidentate coordination via nitrile N atom is the most commonly found however, numerous other compounds with different coordination types are also observed. The tridentate coordination **(5)** via two nitrile nitrogens and central amide nitrogen leads to the formation of the $M(dca)_2$ type complexes that are the focus of my work.

A series of $3d$ transition metal $M^{II}(dca)_2$ (M = V, Cr, Mn, Fe, Co, Ni, Cu) compounds have been prepared and shown to be magnetically ordered with transition temperatures in the range of 1.7-47 K. [67–76] First $M(dca)_2$ materials were synthesized and investigated in mid 1960s by Köhler and co-workers [77] and have been latter re-examined by several research teams worldwide due to their intriguing magnetic and magnetostructural correlations. [69–76]

The isostructural family of α-$M(dca)_2$ compounds can be described as distorted rutile-like three-dimensional (3D) structures that crystallize in the orthorhombic

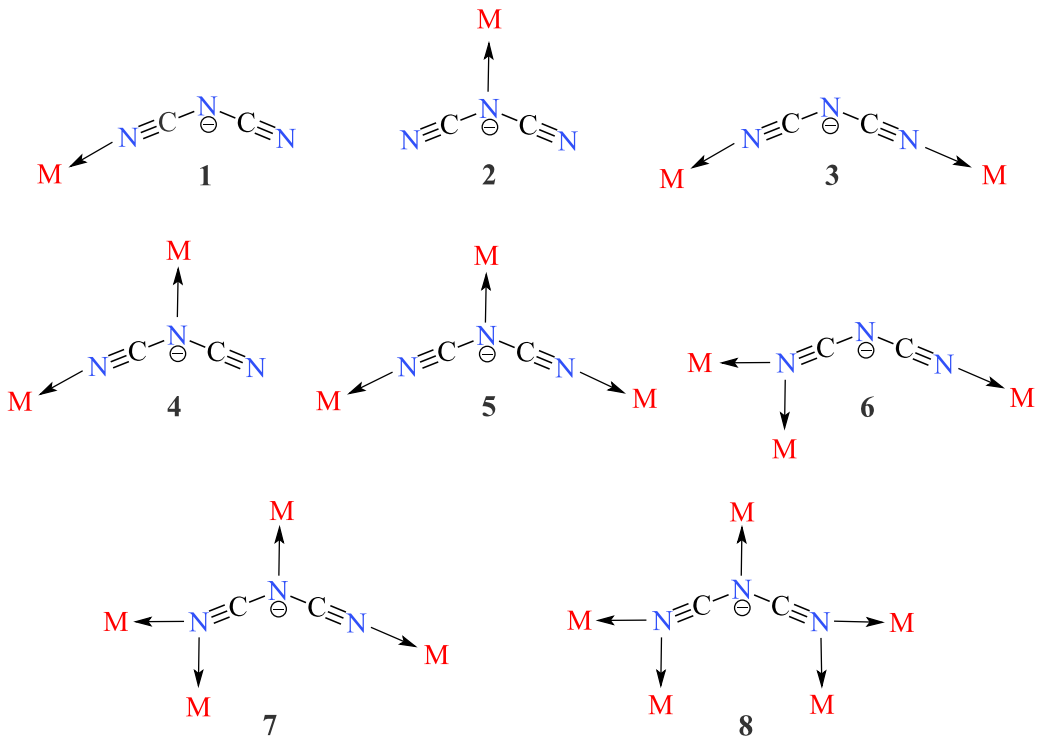

Figure 2.1: Chemical drawings of the dca coordination modes. [67]

space group P*nnm*.[2] [69] The M^{2+} ion resides in the center of an axially elongated octahedron with dca ligands coordinated via nitrile nitrogens in the equatorial plane and via amide nitrogens in the axial direction. The long axes of the MN_6 octahedra lye in the *ab* plane and are successively tilted/rotated around the *c* axis. Interestingly, among the known members of the dca family, the MnN_6 octahedron displays the largest tetragonal distortion as compared to Fe, Co and Ni (Mn-N_{eq} = 2.181 (2) Å, MnN_{ax} = 2.302 (2) Å at room temperature). [68] The Cu analog displays a considerable Jahn-Teller distortion with 1.979 (3) and 2.473 (4) Å values for equatorial and axial bonds, respectively. [70] The structure of these compounds may also be viewed as 1D "chains" of metal-dicyanamide-metal rhombic-shaped units (parallel to *c* axis) connected to the adjacent chains via M-N_{amide} linkages to form a 3D ex-

[2]V and Cr analogs are considered to be isostructural based on X-Ray powder diffraction data.

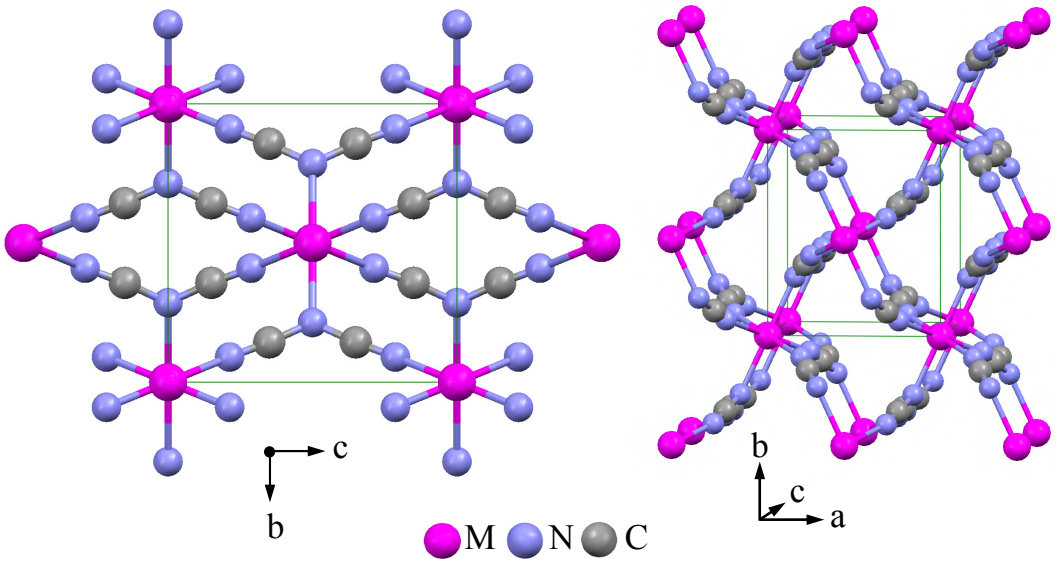

Figure 2.2: The 3D rutile-like structure of α-M(dca)$_2$. [71]

tended network. (Fig. 2.2). There are considerable distortions in the 3D network; their origin was suggested to arise from the $\pi - \pi$ interactions across neighboring dca ligands in ab plane. [71]

Magnetostructural correlations in the M(dca)$_2$ series have received sustained attention due to their interesting magnetic properties that can be tuned with metal substitution. [69–76] For instance, V, Cr, Mn, and Fe materials were found to posses non-collinear antiferromagnetic ordering, whereas ferromagnetic behavior was observed for α-Co, Ni and Cu compounds. Small spin canting in the case of V, Cr, Mn, Fe is attributed to single-ion or exchange anisotropy. [68, 75] To explain magnetic interactions in this family of compounds, a superexchange model with four nearest-neighbor exchange pathways was proposed. [70, 71] From a structural point of view, there are three pathways J_a, J_b and J_c along a, b, and c axes, respectively, and one J_d in the diagonal plane. (Fig. 2.3). [71] For each M center there are two equivalent J_a, J_b, J_c and eight J_d. J_c is a combination of both, direct and superexchange interactions. The strongest and shortest nearest-neighbor magnetic-exchange interaction J_d

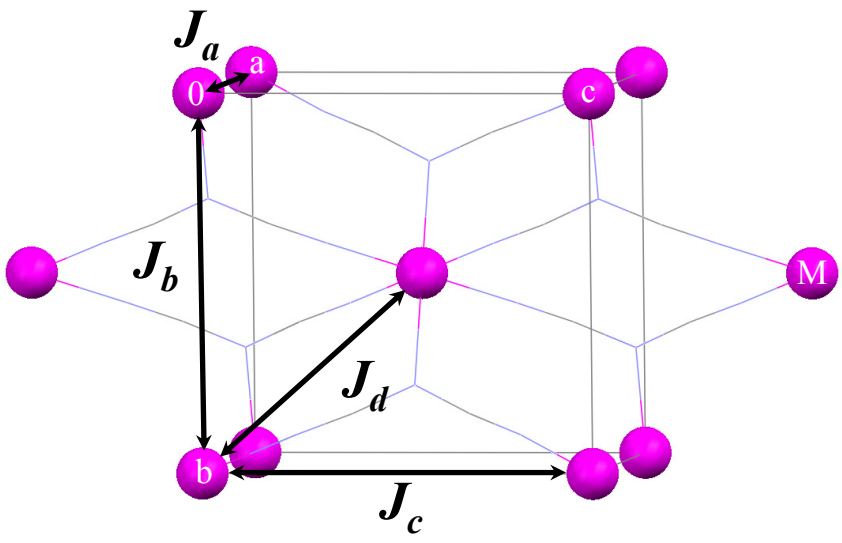

Figure 2.3: Schematic representation of four magnetic-exchange pathways in α-M(dca)$_2$. As an example, in Mn(dca)$_2$ $J_d = 6.07$ Å, $J_a = 6.11$ Å, $J_b = 7.27$ Å and $J_c = 7.56$ Å. [70, 71]

proceeds through the Mn-N≡C-N-Mn linkage. [70, 73]. Although several experimental and theoretical studies addressed the origin of the observed magnetism in M(dca)$_2$ family of compounds, the question of why V, Cr, Mn, Fe are canted antiferromagnets whereas Co, Ni, Cu display ferromagnetic behavior still remains open. [67, 70–73, 76] Subtle competition between antiferromagnetic (AFM) and ferromagnetic (FM) interactions is clearly present in these materials and thus, fundamental understanding of the interplay between various degrees of freedom (i.e electronic, magnetic, elastic) is needed to shine light on behavior of these molecule-based magnets. In this work we bring more insight into this problem through the investigation of charge-lattice-spin interactions in two representatives of this family of compounds, Mn(dca)$_2$ antiferromagnet and Co(dca)$_2$ ferromagnet. Some additional details on their magnetic properties are discussed below.

Mn(dca)$_2$ antiferromagnet

Manganese dicyanamide develops a long range AFM order below the Néel temperature $T_{\mathrm{N}} = 15.85$ K. Two manganese sublattices (defined by the corner (0,0,0) and center (1/2,1/2,1/2) ions) have non-collinear spin arrangements with spin orientation primarily along the a axis and small uncompensated moment along b. [73, 74] The spin canting angle is estimated to be 0.05° and $\mu_{ferro} = 0.002\ \mu_B$. [73, 75] The weak AFM interactions are mediated by the dca ligands with J extracted from the heat capacity measurements $J/k_B = -0.78$ K (single-J Hamiltonian convention). [73] Low magnetic field investigations revealed a spin-flop transition at $B_{sf} = 0.48$ T ($T = 0$ K). Figure 2.4 displays the $B - T$ magnetic field diagram. [74] From the experimental values of B_{sf} and J, the anisotropy of the system is estimated to be $D/k_B = 4 \cdot 10^{-3}$ K. The anisotropy in the magnetic ground state arises as a result of the zero-field splitting of the ground term. For the Mn^{2+} ($S = 5/2$) ion in the octahedral environment the ground state is six-fold degenerate $^6A_{1g}$. The effects of the tetragonal distortion and second-order spin-orbit coupling act to split the spin sextet into three Kramers doublets: $|\pm 1/2\rangle$, $|\pm 3/2\rangle$, and $|\pm 5/2\rangle$. Since value of D is small, at low temperatures all three doublets are thermally populated, thus corresponding to an effective $S' = 5/2$ system. The latter is in agreement with the value of the manganese moment $\mu = 4.61/5\ \mu_B$ found from low temperature neutron powder diffraction studies. [73, 75]

The structural investigation of $Mn(dca)_2$ shows systematic volume decrease of the unit cell and no evidence of structural phase transition down to 4.6 K. [73] The a and b axes display monotonic compression down to $\simeq$ 10 K after which a axis reverses direction and expands at even lower temperatures. On the contrary, c axis was found to exhibit initial expansion with behavior reversal towards compression below 10 K. The origin of this behavior may be related to the development of long

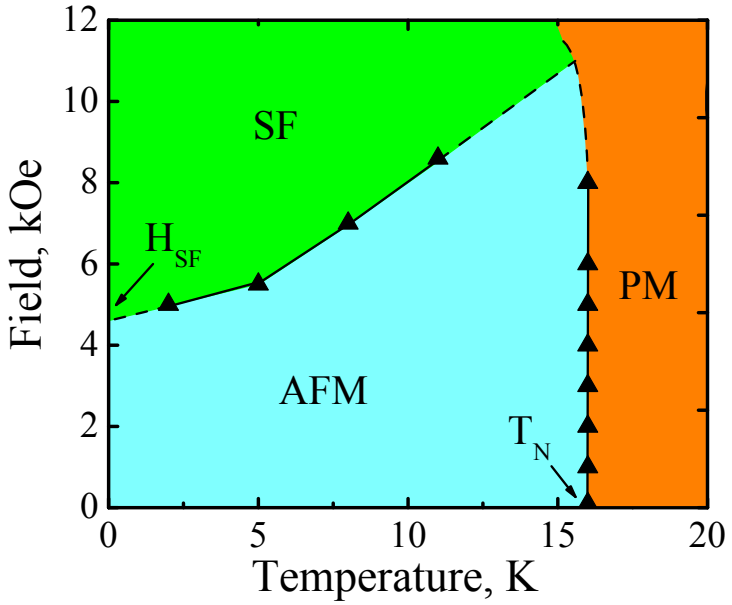

Figure 2.4: $Mn(dca)_2$ field-temperature phase diagram displaying paramagnetic/antiferromagnetic and antiferromagnetic/spin-flop boundaries. Adapted (Fig. 7) with permission from Ref. [74] [J. L. Manson *et al.*, Chem. Mater. **13**, 1068 (2001)]. Copyright (2001) American Chemical Society.

range magnetic order below 15.85 K however, additional magneto-structural investigations are required to bring more insight into these correlations. The local structure deformations are characterized by a less tetragonally distorted octahedra and their decreased tilting in the *ab* plane. [73]

$Co(dca)_2$ ferromagnet

Extensive investigation of α-$Co(dca)_2$ ferromagnet shows the development of long range magnetic order below the 9 K Curie temperature. Neutron diffraction studies reveal collinear structure with spin direction along the c axis. At low temperatures, a reduced magnetic moment of 2.67 (5) μ_B is observed, corresponding to an electronic g-factor of 5.34 and effective spin number $S' = 1/2$. These values are attributed to the effects of large anisotropy and Kramers doublet formation at low temperature. [69,78] At high temperature, material displays an effective spin of $S' = 3/2$ and $g = 2.49$.

One unusual phenomenon in α-Co(dca)$_2$ is its low value of coercive field ($\simeq$ 800 Oe) as compared to the Ni analog ($\simeq$ 7000 Oe). Typically the opposite behavior is expected based on larger single-ion anisotropies characteristic of Co^{2+} compounds. [68,69] As in the case of Mn(dca)$_2$, the strongest superexchange interaction proceeds through the diagonal direction M-NCN-M. Magnetic specific heat data combined with various theoretical models revealed J/k_B values in the range of 2.8-5.2 K (single-J Hamiltonian convention). [79]

Low temperature structural investigations down to 9 K magnetic ordering temperature, showed behavior that is overall similar to Mn(dca)$_2$ in terms of local deformations, volume and unit cell parameters (a and b axes contraction, c axis expansion). [73, 80] Below T_C, magneto-structural correlations were revealed. Magnetostriction effect was evident through the subtle changes in the volume and lattice parameters. [75] Most notable changes are observed in the thermal behavior of the a axis with contraction by 0.0005(2) Å and $\Delta L_a/L_a = -8 \cdot 10^{-5}$ from 9 to 6.5 K.

Pressure studies of α-Co(dca)$_2$ also showed intriguing magnetostructural correlations. [72] Lattice compression leads to a significant suppression of the Curie temperature suggesting a transition from FM to AFM exchange, as a consequence of magnetic orbital overlap changes achieved by the flexible lattice. [72]

Finally, an interesting fact characteristic to Co(dca)$_2$ is the existence of two distinct phases for this material, α(pink)- and β(blue)-phase. While α-phase is isostructural to other members of M(dca)$_2$ family with Co ion residing in an octahedral arrangement, β-phase is considered to have a tetrahedral geometry around Co centers, similar to the diamagnetic Zn(dca)$_2$ analog. [69,81] The β-phase shows canted AFM behavior below $T_{N1} = 8.9$ K and has a second transition at $T_{N2} = 2.7$ K, attributed to spin reorientation. [69]

2.1.2 Paddle-wheel mixed valent $[Ru_2(O_2CR)_4]^+$ cation and diruthenium 3D molecule-based magnets

The discovery of the metal-metal multiple bonding in $[Re_2Cl_8]^{2-}$ by Cotton *et al.* in 1964 led to a considerable interest in these type of compounds and since then numerous compounds with triple, quadruple and even quintuple bonds were synthesized. [82–85] The electron rich metal-metal complexes are attracting a lot of attention due to their intriguing chemistry and structural aspects and also due to their potential applications for instance, in magnetic and optoelectronic devices. [83] Dinuclear carboxylates metal-metal bonded compounds of the type $M_2(O_2CR)_4$ or $M_2(O_2CR)_4L_1L_2$ have been extensively investigated for a large number of ligands and metals (M = V^{2+}, Cr^{2+}, Cu^{2+}, Mo^{2+}, Tc^{3+}, $Ru^{2.5+}$, Rh^{2+}, W^{2+}, Re^{3+}, Os^{3+}). [83,86] Among these, the $[Ru_2(O_2CR)_4]^+$ species displays the most unusual and unique electronic properties that arise from the three unpaired electrons in its ground state.

The D_{4h} diruthenium tetracarboxylate cation $[Ru_2(O_2CR)_4]^+$ has a $\sigma^2\pi^4\delta^2\pi^{*2}\delta^{*1}$ electronic configuration where three unpaired electrons reside on nearly degenerate π^* and δ^* molecular orbitals and result in a quadruplet $S = 3/2$ ground state (Fig. 2.5). [86] Both Ru atoms are known to be crystallographically and magnetically equivalent with the unpaired electrons fully delocalized between both metal centers and thus can be referred to as $Ru_2{}^{5+}$ species. Large zero-field splitting on the order of $\simeq 60$ cm^{-1} arise from strong Ru spin-orbit coupling effects and is a characteristic signature of diruthenium carboxylates. [87] Structurally, Ru_2 complexes adopt a so-called paddlewheel arrangement, originally found in copper(II) acetate with four ligands bridging two metal atoms (Fig. 2.5). [83,87,88] The many advantages of the diruthenium paddlewheel unit, such as its stability, lability and availability of axial sites for coordination, combined with high Ru_2 spin state, make it an extremely useful building block in construction of large molecule assemblies and extended networks.

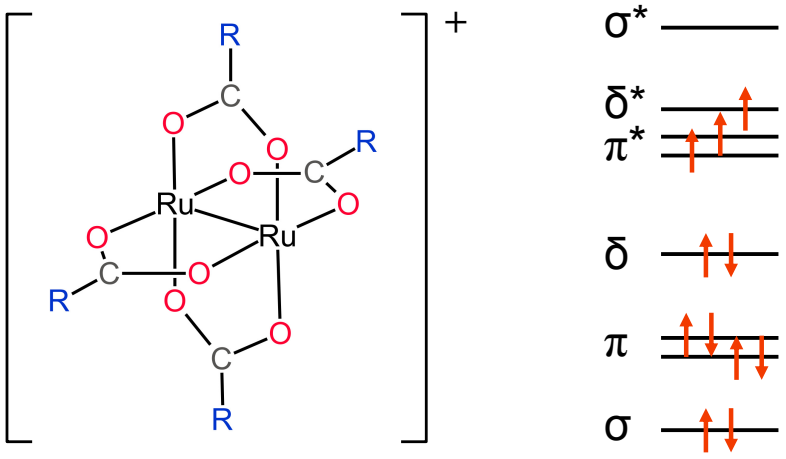

Figure 2.5: Paddle-wheel structure of diruthenium tetracarboxylate cation $[Ru_2(O_2CR)_4]^+$ and its simplified energy level diagram. [83, 86]

The variety of synthesized complexes with alkyl, aryl, alkoxy groups display interesting magnetic, electronic, catalytic, biological and mesomorphic properties. [88]

Recently, in the search for novel molecule-based magnets, a new approach to incorporation of diruthenum units into 3D network was taken by Miller and coworkers. [89] A family of compounds with a general formula $[Ru_2(O_2CMe)_4]_3[M^{III}(CN)_6]$ (Me = CH_3 and M = Mn, Cr, Fe, Co), where paddle-wheel ruthenuim blocks are linked together through the transition metal hexacyanides $[M^{III}(CN)_6]^{3-}$, were synthesized and characterized. [51, 89, 90] Cr, Fe, and Co compounds are isomorphous body centered cubic structures and most interestingly, have two interpenetrating lattices. The Mn analog is stable only below -20 °C. Magnetic investigations reveal AFM interactions in the Cr compound and signatures of long range FM ordering in Fe complex. In addition to acetate derivatives, *tert*-butyl and formate groups were also utilized and resulted in the formation of new two-dimensional (2D) and 3D molecule-based magnets, respectively. [90–93] Taken together these materials present an interesting class of compounds where structural and magnetic properties can be chemically tuned by carboxylate or metal hexacyanide substitution. Moreover,

promising physical tuning in analogy with Prussian blue molecule-based magnets is also anticipated. [94, 95] In this work we will use spectroscopic tools to probe magnetostrucutral interactions and lattice dynamics of $[Ru_2(O_2CMe)_4]_3[Cr(CN)_6]$ under the extreme conditions of high magnetic field and low temperature.

The exotic magnetic properties of $[Ru_2(O_2CMe)_4]_3[Cr(CN)_6]$ derive from its unusual crystal structure. The compound has a body-centered cubic structure (space group $Im\bar{3}m$) with two identical interpenetrating lattices (Fig. 2.6). A single sublattice consists of alternating $[Ru_2(O_2CMe)_4]^+$ and $[Cr(CN)_6]^{3-}$ units with Cr^{III} ions residing at the corners of the cubic unit cell ($a = 13.376$ Å) and linked by CN-bridges to $Ru_2^{II/III}$ dimers at the twelve cubic edges (Fig. 2.6(a, b)). [51,89] The second sublattice resides in the open space of the first sublattice (Fig. 2.6(c)). Each Cr^{III} center of $[Cr(CN)_6]^{3-}$ and each mixed-valent $Ru_2^{II/III}$ unit of $[Ru_2(O_2CMe)_4]^+$ has a spin S=3/2. Previous magnetic studies also demonstrated a large zero-field splitting $D \simeq 69$ cm^{-1} ($D/k_B \simeq 100$ K) associated with $[Ru_2(O_2CMe)_4]^+$. As a result of the large D the $[Ru_2(O_2CMe)_4]_3[Cr(CN)_6]$ behaves as an effective S′=1/2 system at low temperatures. [89] Below the 33 K ordering temperature the system can be described by the AFM intrasublattice coupling $J_c \simeq 1.5$ meV ($J/k_B = 17.4$ K) between neighboring Cr and net Ru_2 moments, that results in the ferrimagnetic arrangement of each sublattice, and a weak AFM intersublattice coupling $K_c \simeq 5 \cdot 10^{-3}$ meV ($K_c/k_B = 0.06$ K). [96,97] Due to the weak coupling between sublattices, application of a small magnetic field acts to align the sublattice moments above the metamagnetic transition $B_c \simeq 0.08$ T. [98] Figure 2.7 displays the temperature dependence of the critical field B_c marking the antiferromagnetic-paramagnetic phase boundary. Theoretical calculations also predict a spin-flop transition at $B_{sf} \approx 80$ T for a single-lattice compound above which higher magnetic fields should bring the system to the fully polarized state. [96] Pressure studies also reveal intriguing results of a reversible

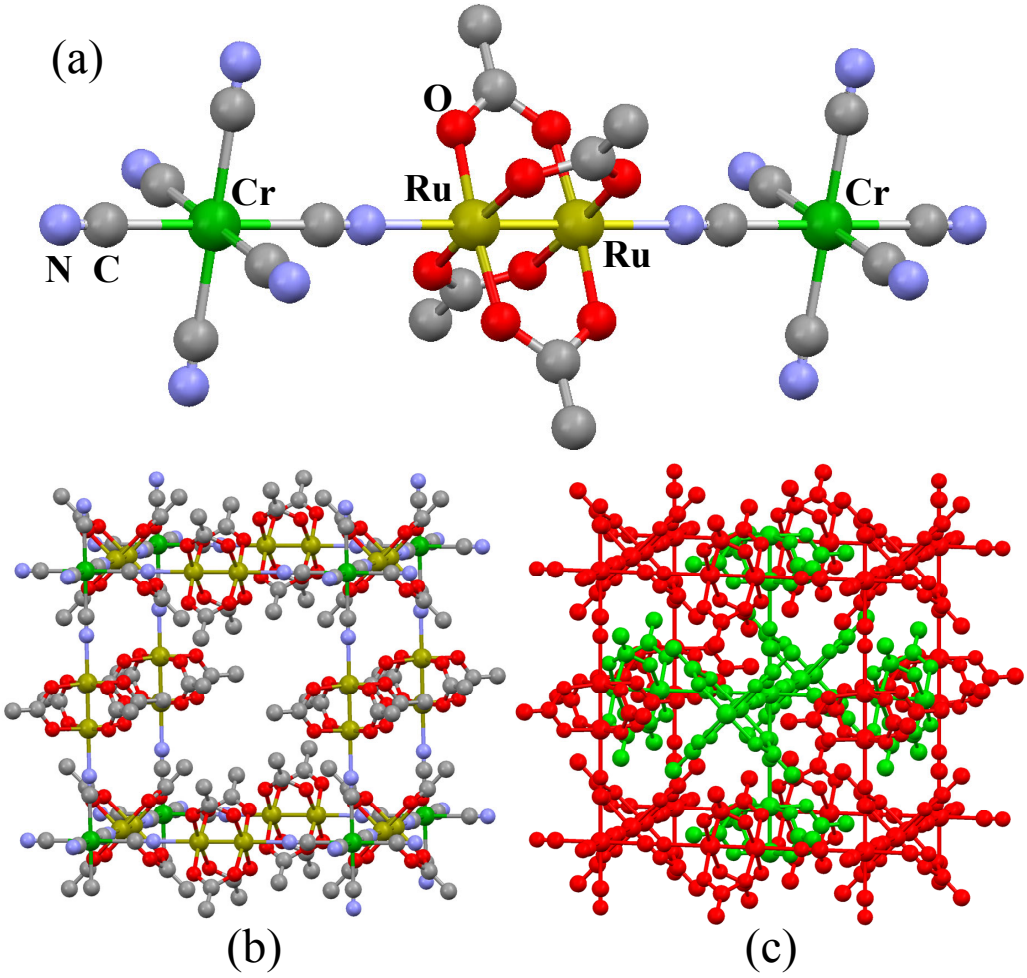

Figure 2.6: (a) Representative Cr^{III} - $Ru_2^{II/III}$ - Cr^{III} structural linkage along with (b) single, non-interpenetrating sublattice and (c) two interpenetrating lattices (red and green) of a body-centered cubic $[Ru_2(O_2CMe)_4]_3[Cr(CN)_6]$. [51, 89] Hydrogen atoms are omitted for clarity.

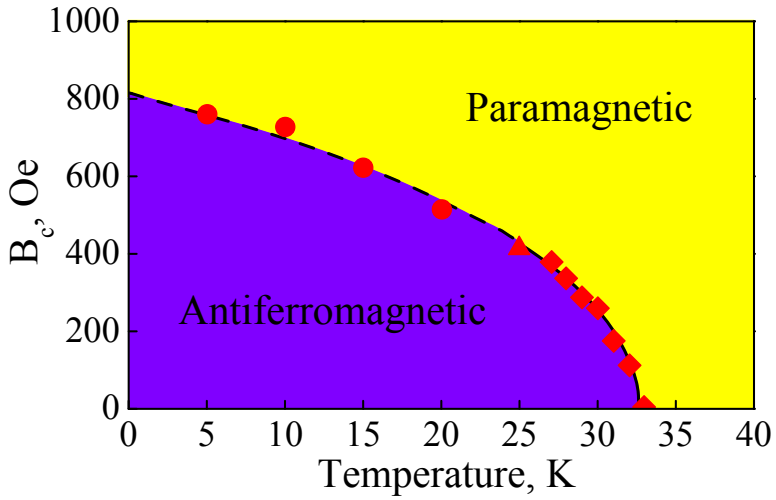

Figure 2.7: $[Ru_2(O_2CMe)_4]_3[Cr(CN)_6]$ $B_c - T$ phase diagram. The ▲ indicates the tricritical point where the first order transition intersect with second order transition. The lines guide the eye. Adapted (Fig. 4) with permission from Ref. [98] [W. W. Shum *et al.*, J. Phys. Chem. C **112**, 7936 (2008)]. Copyright (2008) American Chemical Society.

lattice contraction with proposed cubic to tetragonal structural transition, collapse of intersublattice coalescence transition, and an effective $Ru_2^{II/III}$ high-spin $\rightarrow$ low-spin transformation. [99, 100] Taken together, these findings indicate importance of the spin-lattice interactions in $[Ru_2(O_2CMe)_4]_3[Cr(CN)_6]$ magnet, and the essential role of external stimuli in probing coupling phenomena and system tuning between different ground states.

Table 2.1 summarizes the most important energy scales of the materials investigated in this work.

2.2 Magnetoelastic Coupling

Magnetoelastic phenomenon is a subject of intensive theoretical and experimental studies due to its fundamental importance and wide application in design of functional materials for magneto-optical storage, magnetostrictive actuators, transducers,

Table 2.1: Important energy scales of the compounds of interest

Material	Type of exchange	Ordering temperature	Exchange constant	Anisotropy, D/k_B	Critical field
$Mn(dca)_2$	AFM	15.85 K	$J/k_B = -0.78$ K	$4{\cdot}10^{-3}$ K	$B_{sf} = 0.48$ T
$Co(dca)_2$	FM	9 K	$J/k_B \simeq 4$ K	-	-
$(Ru_2)_3Cr$	AFM	33 K	$J/k_B \simeq 17.4$ K $K_c/k_B \simeq 0.06$ K	100 K	$B_c \simeq 0.08$ T $B_{sf} \simeq 80$ T

oscillators and sensors. [101–104] Magnetoelastic coupling is an intrinsically complex process that arises due to the dependence of the interactions between magnetic centers on interatomic distances. As a consequence, the magnetic and elastic degrees of freedom are coupled. For instance, a sample's shape and dimensions can be affected by the its magnetic state, and/or magnetic properties can be sensitive to mechanical stress. [102, 103]

One result of magnetoelastic coupling is the well known property of magnetostriction, deformation of the sample that reduces the total energy (which is the sum of the magnetic and elastic energy) of the material. In a magnetic material, the main energies that vary with the state of strain are: elastic, magnetostatic, anisotropy, and isotropic exchange energy. The anisotropy energy may include anisotropic exchange, dipole-dipole interaction, and anisotropy due to the crystal-field effects. [104, 105]

Strain dependence of three magnetic energies gives rise to magnetostriction $\delta l/l$:

$$\delta l/l = [l(B) - l(0T)]/l(0T) = \lambda_f + \lambda_{anisotrpic} + \lambda_{isotropic}, \tag{2.1}$$

where l is the length of a sample, and λ_f, $\lambda_{anisotropic}$, and $\lambda_{isotropic}$ are the form effect, anisotropic and isotropic parts of the (forced) magnetostriction, respectively. The form effect is a result of the strain dependence of the magnetostatic energy and arises

purely from the shape of the sample. [105]

The dependence of the anisotropy energy on strain gives rise to linear magnetostriction, originally discovered by Joule (1842) in iron sample exposed to magnetic field. [103] In general, the application of a magnetic field to a ferromagnetic material below its ordering temperature results in the magnetostrictive effect associated with successive growth of energetically favorable domains and rotation of domain vectors towards the field direction. As a result of their strain dependence both, the anisotropy and magnetostatic energies change and accompany this alignment process. On the contrary, no substantial changes in the isotropic exchange energy take place. Thus, magnetostriction at low fields, below technical saturation, is usually dominated by strain dependence of anisotropy and magnetostatic energies. [103–105]

The specific expression for λ that depends on the direction of measurement and the orientation of magnetization $\overrightarrow{\mathbf{M}}$, can be derived for each specific crystal symmetry. [102–104] For instance, in case of cubic crystals (ex. iron, nickel) the directional dependence of the λ can be expressed as:

$$\lambda = \lambda^{\alpha,0} + \lambda^{\gamma,2}(\alpha_x^2\beta_x^2 + \alpha_y^2\beta_y^2 + \alpha_z^2\beta_z^2 - 1/3) + 2\lambda^{\varepsilon,2}(\alpha_x^2\alpha_y^2\beta_x^2\beta_y^2 + \alpha_y^2\alpha_z^2\beta_y^2\beta_z^2 + \alpha_x^2\alpha_z^2\beta_x^2\beta_z^2), \tag{2.2}$$

where $\lambda^{\alpha,0}$ is the isotropic magnetostriction (considered to be small at low fields) and $\lambda^{\gamma,2}$, $\lambda^{\varepsilon,2}$ describe the anisotropic magnetostriction. α_i and β_i are the direction cosines of the magnetization and of the strain measurement direction with respect to the crystalline axes. Higher order terms can be added to this equation if necessary.

Magnetostriction that arises from the strain dependence of the isotropic exchange interactions is known as volume magnetostriction or exchange magnetostriction. This effect is associated with the field-induced change in the spontaneous magnetization (i.e change in $\overrightarrow{\mathbf{M}}$ magnitude rather than its direction relative to the crystal axes). The expression for the volume magnetostriction can be derived if the elastic and

magnetic energy densities are known. [103] For a case of a ferromagnetic cubic crystal, the magnetic energy density is given as:

$$E_{magn} = -NzJ_{ij}(r)\langle \mathbf{S_i} \cdot \mathbf{S_j} \rangle \tag{2.3}$$

$$= -Nz\left[(J_{ij})_0 + r_0\left(\frac{dJ_{ij}}{dr}\right)_0 \frac{1}{3}\frac{\delta V}{V_0} + \frac{1}{2}r_0^2\left(\frac{d^2J_{ij}}{dr^2}\right)_0\left(\frac{1}{3}\frac{\delta V}{V_0}\right)^2\right]\langle \mathbf{S_i} \cdot \mathbf{S_j} \rangle, \tag{2.4}$$

where J_{ij} is the exchange integral for a nearest neighbor atoms with distance r apart (further neighbors are neglected here), z is the number of nearest neighbors, N is the number of atoms per unit cell, and r_0 is the distance in absence of magnetism. The elastic energy density can be written in terms of elastic constants $c_{ij}(c^\alpha)$:

$$E_{el} = \frac{c_{11} + 2c_{12}}{6}\left(\frac{\delta V}{V_0}\right)^2. \tag{2.5}$$

Minimizing the sum of $E_{magn} + E_{el}$ with respect to $\delta V/V_0$ (small magnetic contribution ($(\delta V/V_0)^2$ term) to the elastic constants is neglected), the volume magnetostriction becomes:

$$\frac{\delta V}{V_0} = \lambda^{\alpha,0} = \frac{r_0 N z}{c^\alpha}\frac{dJ_{ij}}{dr}\langle \mathbf{S_i} \cdot \mathbf{S_j} \rangle. \tag{2.6}$$

Forced volume magnetostriction is related to the changes in the spin-spin correlation function under strong external fields. Initial application of a magnetic field to a ferromagnet will result in the alignment of the magnetic moments without affecting $\langle \mathbf{S_i} \cdot \mathbf{S_j} \rangle$ function, however, once the technical saturation is achieved, higher magnetic field will strengthen the parallel orientation of the magnetic moments and thus, lead to an increase in the exchange magnetostriction. If the correlation between spins is absent (i.e $\langle \mathbf{S_i} \cdot \mathbf{S_j} \rangle = 0$), then no exchange magnetostriction will be observed, as for example in the paramagnetic state. [103]

In addition to forced (field-induced) magnetostriction, there is also a sponta-

neous magnetostriction associated with lattice deformation when a sample is cooled through the long range ordering temperature (T_C) at zero field. For exchange magnetostriction, the correlation function $\langle \mathbf{S_i} \cdot \mathbf{S_j} \rangle$ starts to growth on the approach to T_C and eventually reaches a maximum at $T = 0$ K. The resulting change in the exchange energy leads to lattice deformation. [106]

Equation (2.6) can also be applied to antiferromagnets, with $\langle \mathbf{S_i} \cdot \mathbf{S_j} \rangle = -\mathbf{S_i}\mathbf{S_j}$ at T<T_N (Néel temperature). What makes antiferromagnets different however, is that even at $T = 0$ K the exchange energy is field dependent, as compared to ferromagnets where at $T = 0$ K saturation is achieved. [103, 107] The latter makes studies of antiferromagnetic materials at low temperatures and high magnetic fields especially attractive.

Magnetoelastic coupling probed by optical spectroscopy

A magnetostriction measurement is a well-known and accepted technique to study magnetostructural correlations in magnetic materials, however magnetostriction is a bulk technique that relies on the average information about atomic displacements. Investigation of magnetoelastic phenomena with focus on local structure, for instance with optical spectroscopy, offers unique opportunities to reveal on microscopic level which atomic displacements are important in observed macroscopic properties.

Spectroscopy is a highly sensitive technique in investigation of coupling phenomena between multiple degrees of freedom. One of the most well known and studied examples where the interaction between magnetic moments and lattice phonons results in the magnetoelastic transition, is the spin-Peierls system. [108, 109] Here, the magnetoelastic coupling between the (quasi) one-dimensional antiferromagnetic spin-1/2 Heisenberg chains and three dimensional phonon system leads to lattice dimerization and opening of an energy gap in the magnetic excitation spectrum.

The gain in the magnetic energy outweighs the energy loss associated with lattice distortion. First observed in 1975 in the complex Cu spin-1/2 chain system TTF-$CuS_4C_4(CF_3)_4$, this area of research received renewed attention with its discovery in the simpler inorganic compound $CuGeO_3$. [109, 110] The spin-phonon interaction through the phase transition in $CuGeO_3$ was extensively studied with Raman and infrared spectroscopies. [111–115] The magnetoelastic effect is manifested through the appearance of several new modes (folded from a boundary of the Brillouin zone to its center due to lattice dimerization) below the transition temperature (T_{SP}) and pronounced changes in phonon lineshapes and frequencies. As an example, Fig. 2.8 displays optical response of $CuGeO_3$ below $T_{SP} = 14$ K. New vibrational modes in 100-800 cm^{-1} region are evident in the low temperature dimerized phase. At the same time, highly asymmetric shape of the 106 cm^{-1} peak is a signature of a Fano type coupling to the magnonlike continuum of states. [112,115,116] The spectroscopic studies of pressure and magnetic field effect on $CuGeO_3$ affirm strong magnetostructural correlations manifested in an increase of the spin-Peierls transition temperature under compression, and splitting or intensity suppression of the zone boundary folded phonons upon application of strong external fields. [117–120]

Spin-lattice coupling is a primary mechanism in relieving the geometrical frustration of pyrochlore antiferromagnets. The degeneracy of the ground state is removed through a spin-driven Jan-Teller mechanism that results in a symmetry-lowering lattice distortion, reminiscent of the spin-Peierls transition. [121,122] The chromium oxide spinels ACr_2O_4 (A=Mg, Zn, Cd, Hg) received sustained attention in this regard. [123–129]. These materials enter the antiferromagnetic ordered state at temperatures on the order of 10 K with accompanied cubic to tetragonal/orthorhombic structural transition and corresponding strong splitting of the infrared active phonons. An unusually large splitting of the $T_{1u}(2)$ phonon (ex. $ZnCr_2O_4$ $\Delta\omega = 11$ cm^{-1}), as

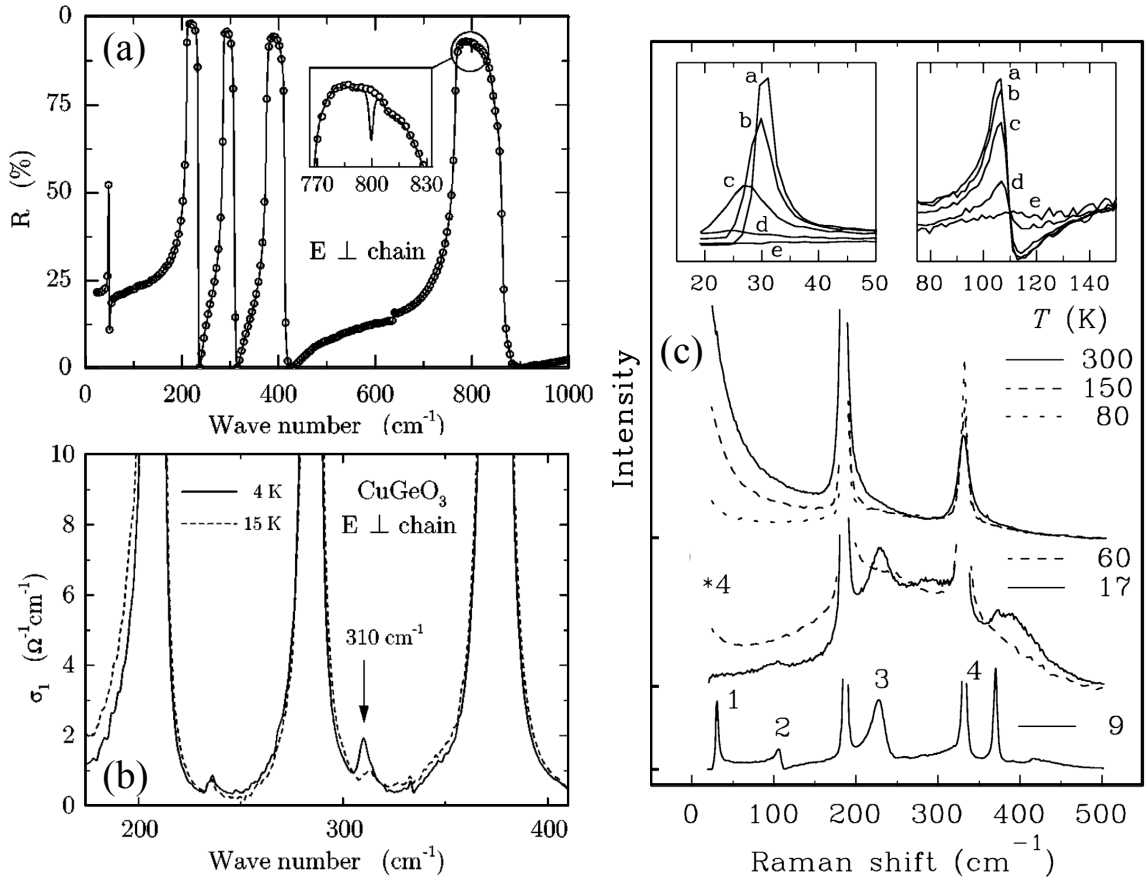

Figure 2.8: (a) and (b) Reflectivity and conductivity spectra of single-crystal $CuGeO_3$ above (15 K - circles/dashed line) and below (4 K - solid line) the spin-Peierls transition. Folded phonons of the dimerized lattice appear at around 800 and 310 cm^{-1}. Reprinted (Fig. 4, 5) with permission from Ref. [115] [A. Damascelli *et al.*, Phys. Rev. B **61**, 12063 (2000)]. Copyright (2000) by the American Physical Society. (c) Variable temperature Raman spectra with four new distinct peaks in the low temperature phase. Peaks 1 and 3 are of magnetic origin, whereas 2 and 4 are phonons activated by structural transition. The insets display a detailed temperature behavior of 32 and 106 cm^{-1} features at T = 9 (a), 11 (b), 13 (c), 15 (d), 17 K (e). Reprinted (Fig. 1) with permission from Ref. [112] [P. H. M. van Loosdrecht *et al.*, Phys. Rev. Lett. **76**, 311 (1996)]. Copyright (1996) by the American Physical Society.

compared to moderate changes in other modes ($\Delta\omega \leq 0.2$ cm^{-1}), was attributed to considerable spin-phonon coupling in this material (Fig. 2.9). Similar behavior was found for Cd analog with $\Delta\omega = 10$ cm^{-1} and for several other Cr spinels. [126, 128] The analysis of the $T_{1u}(2)$ temperature dependence revealed the onset of the magnetoelastic effect long before the transition temperature T_N. It manifests itself in the phonon frequency deviation from the anharmonic behavior and pronounced softening below $\simeq 100$ K (Fig. 2.9).

The idea that in magnetic materials the phonon frequency is sensitive to the correlation of the nearest neighbor spins was emphasized in late 1960's by Baltensberger and Helman. [130] For a displacement x from the equilibrium position, the total potential energy of the crystal in the harmonic approximation can be written as:

$$U = \frac{1}{2}k_0x^2 + \sum_{i,j} J_{i,j}(x)\langle \mathbf{S_i} \cdot \mathbf{S_j}\rangle. \tag{2.7}$$

The second term provides a magnetic contribution to the potential energy and arises due to the dependence of the exchange integral J on structural parameters and its modulation by lattice vibrations. From (2.7) the second derivative with respect to x gives an expression for the force constant, k:

$$\frac{d^2U}{dx^2} = k = k_0 + \sum_{ij} \frac{d^2J_{ij}}{dx^2}\langle \mathbf{S_i} \cdot \mathbf{S_j}\rangle. \tag{2.8}$$

The phonon frequency ω is now written as:

$$\omega^2 = \omega_0^2 + \frac{4J''}{m}\langle \mathbf{S_i} \cdot \mathbf{S_j}\rangle, \tag{2.9}$$

where m is ion mass and $J'' = d^2J_{ij}/dx^2$. Equation 2.9 can be expanded to give:

$$\omega \approx \omega_0 + \lambda'\langle \mathbf{S_i} \cdot \mathbf{S_j}\rangle. \tag{2.10}$$

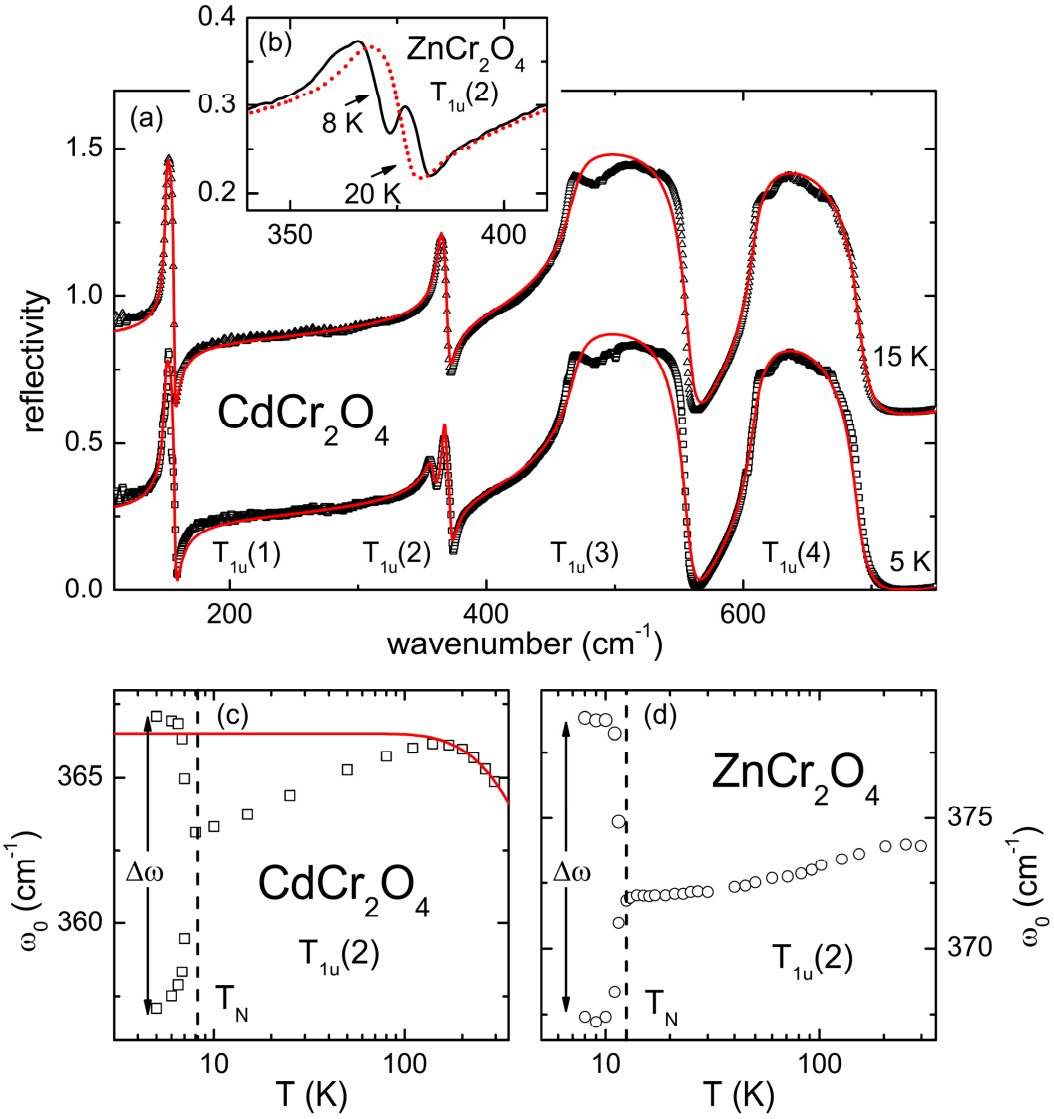

Figure 2.9: (a) $CdCr_2O_4$ reflectivity spectra above and below T_N. (b) Close up view of the $ZnCr_2O_4$ $T_{1u}(2)$ mode demonstrating its splitting below the magnetic ordering temperature. (c) and (d) Frequency versus temperature behavior of the $T_{1u}(2)$ mode for the $CdCr_2O_4$ and $ZnCr_2O_4$, respectively. Reprinted (Fig. 4) with permission from Ref. [128] [Ch. Kant *et al.*, Phys. Rev. B **80**, 214417 (2009)]. Copyright (2009) by the American Physical Society.

Here, ω_0 is the frequency in absence of spin-phonon coupling and $\lambda' = 2J''/(m\omega_0)$ is the coupling constant. [125, 131–133] The expression (2.10) was employed in case of $ZnCr_2O_4$ and $CdCr_2O_4$ to extract the spin-phonon coupling constants in high temperature regime. The spin correlation functions were determined from the magnetic heat capacity and susceptibility data. The resulting coupling constants were found to be large with $\lambda' \simeq 4 - 6.2$ and $3.3 - 3.9$ cm^{-1} for $ZnCr_2O_4$ and $CdCr_2O_4$, respectively. [125, 128] An additional support for the strong spin-phonon coupling mechanism in $T_{1u}(2)$ phonon behavior is provided by the analysis of its vibrational pattern. The assignment suggests chromium displacement that strongly modulates Cr-Cr distances and consequently the exchange interaction J between these magnetic centers. Thus, chromium spinels are excellent illustrative examples of sensitivity of microscopic techniques in probing short-range spin correlations above magnetic ordering transitions and associated magnetoelastic coupling effects.

Besides spin-Peierls systems and spinel oxides, the interplay between spin and lattice degrees of freedom have been attracting considerable attention in other complex compounds for decades. It has been shown to be an important aspect of behavior and properties in variety of technologically important materials, for instance in binary metal oxides MO (M = Cu, Mn, Co, Ni), [132, 134, 135] perovskite manganites $RMnO_3$ (R = rare earth), [136–139] layered ruthenates $(Sr,Ca)_{n+1}Ru_nO_{3n+1}$ (n = number of Ru-O layers/unit cell), [140, 141] and multiferroics $CuFeO_2$, $BiFeO_3$, $EuTiO_3$, RMn_2O_5 (R = Dy, Eu, Bi). [142–146] The large spin-lattice coupling in these materials does not necessarily result in the static deformation of the crystal, but may have a dynamic nature where modulations of magnetic moments couple to lattice vibrations. The latter is true for example in chromium-based spinels, multiferroic manganites, and many other magnetic materials listed above. The optical spectroscopy was demonstrated to be an extremely useful technique in uncovering

local origin of magnetoelastic effects and particulary important in revealing dynamic interactions.

A remarkable signature of the magnetoelastic phenomena is in the variety of forms that it can manifest itself, for instance, through magnetostriction and magnetostructural transitions (as in CoO, Mn_3O_4, $ZnCr_2O_4$), [125, 128, 134, 147, 148] spin-phonon interactions (as in MnF_2, $GaFeO_3$, $DyMn_2O_5$, $ZnCr_2O_4$), [125, 131, 146, 149] magnon-phonon coupling (as in La_2CuO_4, $KCoF_3$, $CoCl_2{\cdot}2H_2O$), [65, 150, 151] and electromagnons (as in $RMnO_3$, RMn_2O_5 (R = Tb, Gd, Y)) [152, 153]. Magnetoelastic coupling plays a crucial role in the exotic properties of many complex materials where it drives interesting phase transitions, stabilizes grounds states and offers unique opportunities for manipulation and control of competing interactions by applied external parameters, such as magnetic field, pressure, temperature and/or strain.

Among available physical stimuli, studies in high magnetic fields provide one the most direct ways of probing magnetostructural correlations in novel materials. Simultaneous application of external field and optical excitation such as in magneto-optical spectroscopy has been demonstrated to be an extremely useful and revealing technique for probing spin-lattice interactions in variety of complex compounds. Numerous studies on oxides, coordination polymers and single-molecular magnets uncovered interesting coupling effects and important relationships between magnetic configurations and atomic displacements that accompany and/or facilitate development of new states. [54, 141, 146, 154–157]

Chapter 3

Methods

3.1 Introduction: Infrared and Raman Spectroscopy Fundamentals

Spectroscopy is the study of the interaction between matter and electromagnetic (EM) radiation. When an atom/molecule/solid is subject to EM radiation, several types of interactions such as, absorption, emission, reflection and/or scattering can take place. A transfer of energy from the EM field to a sample can occur only if $\Delta E = h\nu$ condition is satisfied. Here, ΔE is the energy difference between two quantized states, h is Planck constant and ν is the frequency of the radiation. As an example, in an absorption process, this transfer will result in energy increase of an absorbing

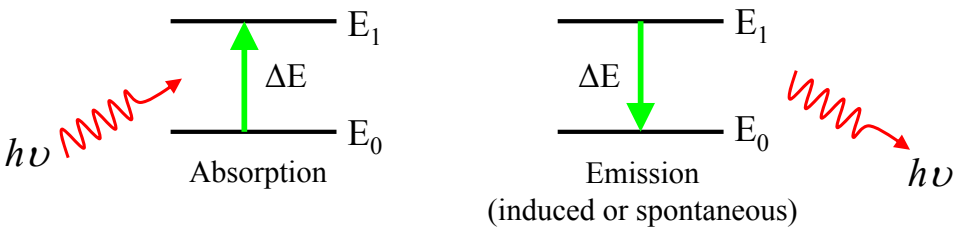

Figure 3.1: Schematic representation of an absorption and emission process.

Table 3.1: Common spectroscopic techniques and their origin

Type of spectroscopy	Frequency range, cm^{-1}	Origin
NMR	10^{-2}-10^{-4}	Transitions between nuclear spin levels in magnetic field
ESR	1-10^{-2}	Transitions between electron spin levels in magnetic field
MW	10^{2}-1	Transitions between rotational levels
IR, Raman	10^{4}-10^{2}	Transitions between vibrational levels
UV-Vis, UPS	10^{6}-10^{4}	Valence electrons transitions
X-Ray (XPS, XAFS)	10^{8}-10^{6}	Core electrons transitions
γ-Ray (MB, PAC)	10^{10}-10^{8}	Nuclear processes

NMR (Nuclear magnetic resonance), ESR (Electron spin resonance), MW (Microwave), IR (Infrared), UV-Vis (Ultraviolet-visible), UPS (Ultraviolet photoelectron spectroscopy), XPS (X-ray photoelectron spectroscopy), XAFS (X-ray absorption fine structure), MB (Mößbauer spectroscopy), PAC (Perturbed angular correlation). Adapted from reference [158]

material from the ground state E_0 to the specific excited state E_1. In emission, reverse process takes place - return from an excited level to the gound/lower lying energy state (Fig. 3.1). [158,159] The magnitude of ΔE is characteristic of the origin of the transition. Table 3.1 lists various spectroscopic techniques associated with different regions of the EM spectrum and the energies of typical physical processes.

NMR and ESR transitions are induced by the oscillating magnetic field component of the EM radiation. For IR and Raman spectroscopies, that are employed in this work, typically, only the electric field component is important. [158–160] Transitions coupled to the magnetic part however, are not rare. Although vibrational spectroscopy is traditionally designated for transitions that originate from the vibrations of nuclei, it is however, not limited only to studies of molecular/lattice dynamics. Solid-state spectroscopy is particulary rich here. In addition to lattice excitations, IR and Raman spectroscopy can be used to probe single-ion and cooperative excitations of electronic and magnetic origin, for instance, low-lying crystal field

transitions and magnons. [60–63] Moreover, excitations arising due to the coupling between various degrees of freedom, such as electron-phonon, crystal field-magnon, magnon-phonon and/or electromagnon, constitute a rich field for fundamental investigations. [61, 62, 64, 152] Light scattering and optical absorption are complementary techniques and usually both are employed in studies of elementary and collective excitations in complex materials.

3.1.1 Molecular spectroscopy

a) Harmonic oscillator

A simple model of harmonic oscillator is usually invoked to gain better understanding of vibrations. [158, 159, 161] Taking the simplest case of vibrating diatomic molecule and treating the system quantum mechanically, one can write the Schrödinger equation as:

$$\left(-\frac{\hbar^2}{2\mu'}\frac{d^2}{dx^2} + U(r)\right)\psi = E\psi, \tag{3.1}$$

where μ' is the reduced mass, $\hbar = h/2\pi$, $U(r) = \frac{1}{2}kx^2$ - potential energy with k being a force constant, and x - the displacement from equilibrium (r-r$_e$). Solving this equation with condition that ψ is single-valued, finite and continuous gives the corresponding eigenvalues:

$$E = h\nu\left(n + \frac{1}{2}\right), n = 0, 1, 2... \tag{3.2}$$

with

$$\nu = \frac{1}{2\pi}\left(\frac{k}{\mu'}\right)^{1/2}, \tag{3.3}$$

where ν is the frequency of vibration and n is the vibrational quantum number. [158, 159] In the case of the harmonic potential, the energy states are equidistant and the separation between two successive energy levels is always equal $h\nu$. In

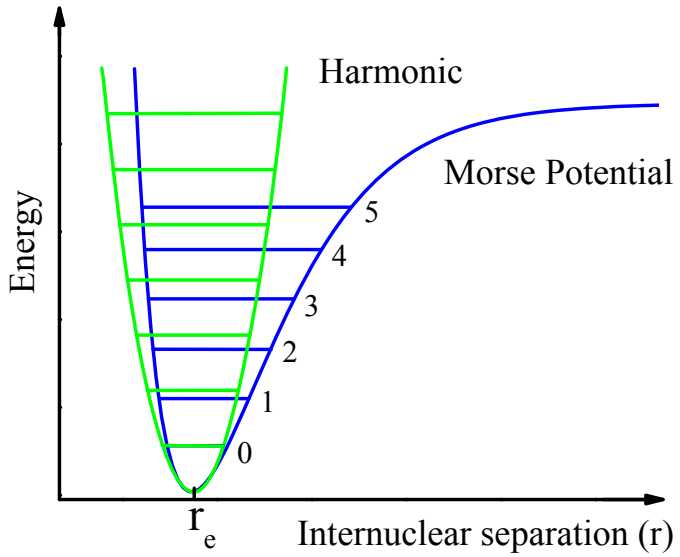

Figure 3.2: Comparison of the harmonic oscillator and anharmonic (Morse) potential. [159]

real molecules this is not the case. The separation between adjacent levels becomes smaller with increasing n. Thus, in practice a more realistic anharmonic (Morse-type) potential is used to describe an actual molecule:

$$U(r) = D_e(1 - e^{-\beta x})^2. \tag{3.4}$$

Here, D_e is the dissociation energy and β measures the curvature at the bottom of the potential well. [158] Figure 3.2 shows a comparison between the potential energy of harmonic and anharmonic oscillator as a function of the internuclear distance, r. As can be seen, the deviation from harmonic oscillator behavior becomes greater at higher vibrational quantum numbers with Morse potential asymptotically approaching the dissociation limit $U(r) = D_e$. Solving the Schrodinger equation for the Morse potential one finds the eigenvalues:

$$E = h\nu_e(n + \frac{1}{2}) + h\nu_e x_e(n + \frac{1}{2}), \tag{3.5}$$

where ν_e is the corrected frequency and $h\nu_e x_e$ defines the magnitude of the anharmonicity. [158, 159, 161]

The harmonic oscillator model provides a good approximation at small values of n, where the difference between harmonic and anharmonic potential is small. However, at higher n, harmonic oscillator approximation is no longer valid. According to quantum mechanics, the vibrational selection rules for the harmonic oscillator only allow transition to adjacent vibrational levels, i.e. $\Delta\nu = \pm 1$ (fundamental transitions). In the anharmonic approximation, transitions involving $\Delta\nu = \pm 2, 3...$ (overtones) are also allowed, although their intensity is much weaker and decreases with increasing $\Delta\nu$. [159]

The harmonic oscillator model can be applied beyond the simple diatomic molecule. It forms the basis for the understanding of complex vibrations in polyatomic molecules and collective oscillations of atoms in solids. The latter is of interest in this work.

b) Infrared absorption and Raman scattering

Infrared absorption

In IR spectroscopy the absorption of light by a medium is quantified by the absorption coefficient α. If the beam of initial intensity I_0 is propagating through the absorbing material of thickness d, then the transmitted radiation I is generally expressed by Beer's law [158]:

$$I = I_0 e^{-\alpha d}. \tag{3.6}$$

Commonly used by spectroscopists infrared transmittance ($\mathcal{T}$) and absorbance (A) are defined as:

$$\mathcal{T} = \frac{I}{I_0} \quad \text{and} \quad A = -ln\frac{I}{I_0} = \alpha d. \tag{3.7}$$

It is important to note that in equations (3.7) the intensity of the radiation I must

be corrected for other effects such as, for example reflectance, so that the difference between I and I_0 arises purely from absorption. For instance, the expression for transmittance with correction to reflectance is given as:

$$\mathcal{T} = \frac{(1-R)^2 e^{-\alpha d}}{1 - R^2 e^{-2\alpha d}}, \tag{3.8}$$

where R is the reflectance at the sample's surface. [162]

For the infrared absorption to take place, the selection rules must be considered. [159, 161] The fundamental selection rule for IR spectroscopy requires a change in the dipole moment of the molecule during the vibration. Quantum mechanically the intensity of the vibrational transition depends on the magnitude of the transition moment integral M:

$$M = \int \psi'^{*}_{vib} \boldsymbol{\mu}(r) \psi''_{vib} dr. \tag{3.9}$$

Here ψ'_{vib} refers to the excited/upper state and ψ''_{vib} to the ground/lower state. The dipole moment is a function of (r) and can be expanded as a Taylor series, $\boldsymbol{\mu}(r)$ about $r = r_e$:

$$\boldsymbol{\mu}(r) = \boldsymbol{\mu}_e + \left.\frac{d\boldsymbol{\mu}(r)}{dr}\right|_{r_e} (r - r_e) + \frac{1}{2} \left.\frac{d^2\boldsymbol{\mu}(r)}{dr^2}\right|_{r_e} (r - r_e)^2 + ... \tag{3.10}$$

Using (3.10) M becomes:

$$M = \boldsymbol{\mu}_e \int \psi'^{*}_{vib} \psi''_{vib} dr + \left.\frac{d\boldsymbol{\mu}(r)}{dr}\right|_{r_e} \int \psi'^{*}_{vib} (r - r_e) \psi''_{vib} dr + ... \tag{3.11}$$

The first term in equation (3.11) is zero because of the orthogonality of the vibrational functions, and thus the second term ($|d\boldsymbol{\mu}/dr|_{r_e} \neq 0$) makes the largest contribution to the magnitude of M and therefore intensity of fundamental vibrational transitions. Higher power terms are neglected. More specifically, the measured IR intensity is

actually proportional to the square of the change in the dipole moment:

$$I \propto |M|^2 \propto \left| \frac{d\boldsymbol{\mu}}{dr} \right|_{r_e}^2 . \tag{3.12}$$

Raman scattering

The origin of the Raman scattering is different from that of IR absorption. In a typical experiment a sample is irradiated by a monochromatic light from a laser (visible or near-infrared) and the scatted light is collected at 90° or 180° angle to the incident beam (called "90° or back-scattering geometries"). Most of the radiation is scattered elastically and has the same frequency as that of the original excitation ν_0 (Rayleigh scattering) however, small amount of the scattered light looses some energy and remains with frequency that is shifted relative to the incident beam, i.e $\nu_S = \nu_0 \pm \nu_x$ (Raman scattering). [158, 159] Here ν_x can correspond to frequencies of rotational, vibrational or electronic transitions. In this section, we will only focus on the most common, vibrational Raman effect. Figure 3.3 shows a schematic energy diagram of Rayleigh and Raman scattering as well as an example of the IR absorption

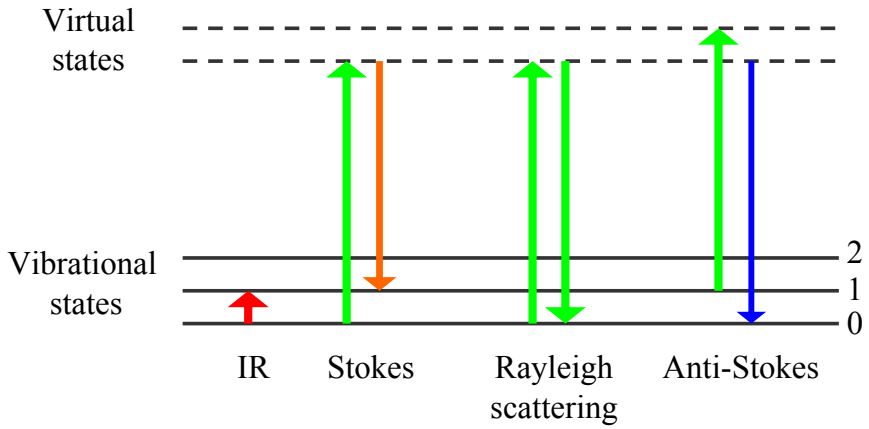

Figure 3.3: An illustration of the IR absorption, Rayleigh scattering, Raman Stokes and anti-Stokes lines with respect to the energy levels involved in each transition. Line colors and thicknesses schematically show frequency and intensity of each transition.

process emphasizing their different nature. In case of Rayleigh process, an elastic scattering from the so-called 'virtual state' (non-resonant Raman) takes place with no change in photon energy. The Raman scattering is an inelastic collision between the molecule and the photon. Here, two types of scattering are possible: Stokes and anti-Stokes. If a molecule is initially in the ground vibrational state, the Stokes scattering ($\nu_S = \nu_0 - \nu_{vib}$) is a result of a transition from a 'virtual state' to an excited vibrational state. In anti-Stokes process ($\nu_S = \nu_0 + \nu_{vib}$), molecule is initially in vibrational excited state and scattered photon is a result of a transition from a 'virtual state' to the vibrational ground state. Under normal conditions (ex. room temperature), the intensity of the Stokes lines is larger than that of the anti-Stokes due to the higher population of the ground vibrational state (Boltzmann distribution law). Therefore for the practical purposes it is customary to record only the Stokes lines.

To describe the nature of the Raman effect a classical theory can be invoked. [158, 159] When a medium is subject to an electric field of strength E, it undergoes a distortion due to the opposite motion of electrons and nuclei governed by the Coulomb interactions. As a result, the applied field induces a dipole moment in a molecule:

$$\boldsymbol{\mu}_{ind} = \alpha^p \boldsymbol{E}^1 = \alpha^p E_0 \cos 2\pi\nu_0 t, \tag{3.13}$$

where the proportionality constant α^p is called polarizability and $\boldsymbol{E} = E_0 \cos 2\pi\nu_0 t$ gives variation of electric field strength with time (t). If a molecule vibrates and modulates this induced dipole moment then the linear dependence of the polarizability

[1] Linear relationship between $\boldsymbol{\mu}_{ind}$ and E is valid if the applied electric field is not too strong. Also, in actual molecules α^p will be a tensor.

on vibrational coordinate can be expressed as:

$$\alpha^p = \alpha_0^p + \left.\frac{d\alpha^p}{dQ_i}\right|_0 Q_i^0 \cos 2\pi\nu_{vib}t. \tag{3.14}$$

Here Q is the vibrational coordinate, Q_i^0 is the vibrational amplitude, and α_0^p and $(d\alpha^p/dQ_i)_0$ are evaluated the equilibrium position. Substituting the equation (3.14) into (3.13) one obtains:

$$\boldsymbol{\mu}_{ind} = \alpha_0^p E_0 \cos 2\pi\nu_0 t + \frac{1}{2}\left.\frac{d\alpha^p}{dQ_i}\right|_0 Q_i^0 E_0[\cos 2\pi(\nu_0 + \nu_{vib})t + \cos 2\pi(\nu_0 - \nu_{vib})t]. \tag{3.15}$$

The first term is responsible for the Rayleigh scattering at ν_0 while the second and third terms correspond to the inelastic Raman scattering, anti-Stokes $(\nu_0 + \nu_{vib})$ and Stokes $(\nu_0 - \nu_{vib})$, respectively. Thus, for the vibration to be Raman-active, the change in polarizability is required (i.e. $(d\alpha^p/dQ_i)_0 \neq 0$). As in the case of IR spectroscopy, the measured Raman intensity is proportional to the square of $(d\alpha^p/dQ_i)$ quantity.

3.1.2 Optical properties of solids

Optical spectroscopy of solids differs from the spectroscopy of liquid or gas phase. It is far more complex due to the periodic arrangement of atoms/ions/molecules in a solid state. Table 3.2 compares the main characteristic features of vibrational spectroscopy of gases, liquids and solids. [163, 164]

The existence of the long-range lattice periodicity in solids leads to the formation of coupled collective excitations (phonons). Phonons are quantized modes of lattice vibrations where motion of the neighboring atoms is not independent of each other. [165] In a 3D crystalline material with N number of atoms per unit cell, lattice vibrations are described in terms of $3N$ branches for the phonon dispersion

Table 3.2: Comparison of the vibrational spectroscopy characteristics in gas, liquid and solid state

Gas phase	Liquid	Crystalline Solid
Free non-interacting rotors, sharp bands	No discrete rotational/vibrational levels, broad bands → molecular dynamics	Long-range periodicity → coupled, collective vibrations (phonons), band shape highly dependent on crystal nature
Both, rotational and vibrational levels can be probed	Strong intermolecular interactions (H-bonding, dipole-dipole, etc.)	Low-frequency lattice vibrations: translational and librational modes
Quantitative information on rotational constants, bond lengths, angles, etc.	Polarization studies - limited information on symmetry of vibrations	Strong intermolecular interactions
Total of $3N-6$, $3N-5$ (linear molecule) vibrations		Polarization studies - details on vibrational symmetry and structure
Selection rules - defined by molecular symmetry, point group analysis		$3N-3$ optical phonons (3 acoustical modes) Dispersion curves over the Brillouin zone
		Selection rules - defined by crystal symmetry, space group analysis
		Surface, size and confinement effects, lattice defects and impurities affect spectral response
		Other fundamental excitations of electronic and magnetic origin + coupled excitations can be probed

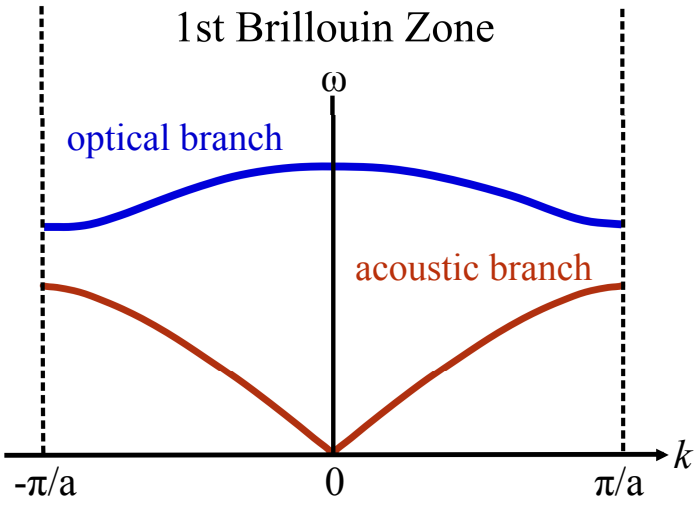

Figure 3.4: Phonon dispersion curves for the simple linear diatomic chain (-A-B-A-B- type), with optical and acoustic branches. [165]

curves. The latter contains three acoustic branches and $3N-3$ optical branches (Fig. 3.4). Optical spectroscopy (IR and Raman) probes excitations at $k = 0$, while their dispersion is usually explored by inelastic neutron scattering techniques. Acoustic phonons correspond to uniform translation of the entire crystal and are analogous to translational modes of a molecule (typically subtracted to find vibrational degrees of freedom). Optical phonons are "internal vibrations" of atoms that are of interest to spectroscopists.

The total number of "active" modes in a crystal is governed by the symmetry of the unit cell as well as the symmetry of the molecule/groups of atoms (local environment). Generally, if the crystal symmetry is lower than the molecular symmetry, appearance of larger number of modes is expected due to mode splitting and activation of silent vibrations. Correlations between molecular→site→space group symmetry can be used to predict number of spectral bands and their nature in each particular case. [166, 167] Many analogies in the nature of the vibrational motion can be drawn between molecular species and molecule-based solids. For instance, sim-

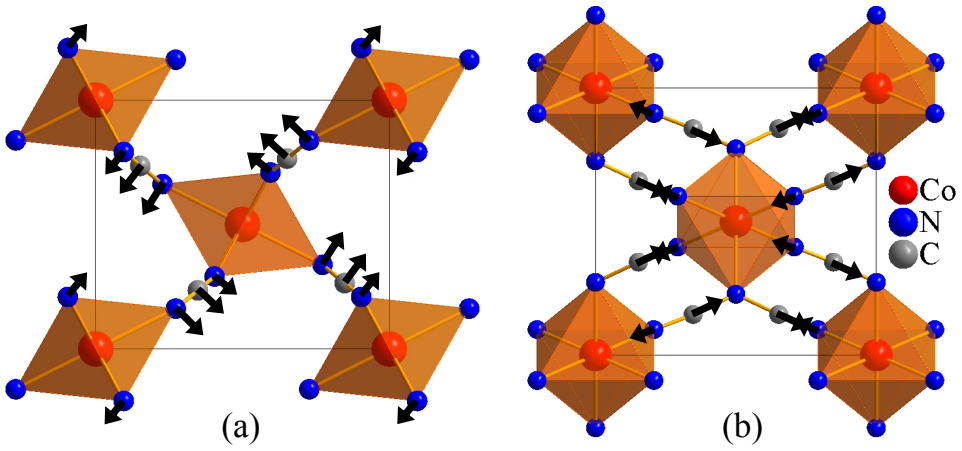

Figure 3.5: A schematic representation of the vibrational displacement patterns for cobalt dicyanamide. (a) Low frequency CoN_6 octahedra counter-rotation mode near 50 cm^{-1}. (b) C≡N stretching vibrational mode near 2215 cm^{-1}.

ple molecular-type vibrations like, C-H, C≡N, C=O stretching bands can be readily identified among phonons. However, other modes such as low frequency metal-ligand bands and lattice modes are generally manifestations of a collective nature of lattice dynamics and can hardly find an equivalent in molecular spectroscopy. Figure 3.5 demonstrates an example of such a collective vibration that involves CoN_6 octahedra counter-rotation in $Co(dca)_2$ compound in comparison to "solid-state analog" of the C≡N stretch.

The study of phonons is an essential part of solid state science. They play a key role in physical properties of solids for instance, in specific heat, thermal, and electrical conductivity. Furthermore, phonons and other elementary/collective excitations provide fundamental information on elastic and optical properties of materials.

Optical constants

The optical constants are the parameters that govern the optical behavior of materials. They reflect properties of the bulk phase rather than of the individual molecules. Experimentally, some observable, such as reflectance, transmittance or light scatter-

ing are used to extract the frequency-dependent optical constants $n(\omega)$ and $\kappa(\omega)$, dielectric function $\varepsilon(\omega)$, optical conductivity $\sigma(\omega)$. These functions are applicable to a large spectral range from microwaves to γ-rays and often provide insight to intrinsic properties of solids.

The important relationships for optical constants are introduced through Maxwell equations (SI units) [168, 169]:

$$\nabla \times \mathbf{E} = -\frac{\partial \mathbf{B}}{\partial t} \tag{3.16}$$

$$\nabla \times \mathbf{H} = \frac{\partial \mathbf{D}}{\partial t} + \mathbf{j} \tag{3.17}$$

$$\nabla \cdot \mathbf{D} = \rho^{ext} \tag{3.18}$$

$$\nabla \cdot \mathbf{B} = 0, \tag{3.19}$$

where $\mathbf{E}$ and $\mathbf{H}$ are the electric and magnetic fields, $\mathbf{D}$ and $\mathbf{B}$ are the displacement field and magnetic induction, ρ^{ext} is charge density induced by external force, and $\mathbf{j}$ is current density.

Working in isotropic media and within the linear approximation, the vectors **E, H, D, B, j** and the polarization $\mathbf{P}$ are connected by the following relationships:

$$\mathbf{D} = \varepsilon\varepsilon_0\mathbf{E} \tag{3.20}$$

$$\mathbf{B} = \mu\mu_0\mathbf{H} \tag{3.21}$$

$$\mathbf{j} = \sigma\mathbf{E} \tag{3.22}$$

$$\mathbf{P} = (\varepsilon - 1)\varepsilon_0\mathbf{E}, \tag{3.23}$$

where ε is the dielectric function, σ is the optical conductivity, μ is the magnetic permeability, ε_0 and μ_0 are vacuum permittivity and permeability, respectively. For

the isotropic and homogeneous media, both ε and σ are scalar quantities rather than tensors.

From Maxwell's equations and relationships (3.20-3.23) we obtain a wave equation for a non-conducting ($\sigma = 0$) and non-magnetic ($\mu = 1$) medium [168–170]:

$$\nabla^2 \mathbf{E} = \frac{\varepsilon}{c^2} \frac{\partial^2 \mathbf{E}}{\partial t^2}. \tag{3.24}$$

Using the plane wave solution

$$\mathbf{E} = \mathbf{E}_0 e^{i(\mathbf{k}\cdot\mathbf{r} - \omega t)}, \tag{3.25}$$

where $\mathbf{k}$ is the complex propagation constant, ω is frequency, and substituting it into equation (3.24) yields:

$$k^2 = \frac{\omega^2}{c^2} \varepsilon(\omega). \tag{3.26}$$

Expressing k by the complex index of refraction $\widetilde{N} = \sqrt{\varepsilon(\omega)}$ gives:

$$k = \frac{\widetilde{N}\omega}{c}. \tag{3.27}$$

Complex index of refraction $\widetilde{N}(\omega)$ is defined by the following expression:

$$\widetilde{N}(\omega) = n(\omega) + i\kappa(\omega) \tag{3.28}$$

and the complex dielectric function:

$$\varepsilon(\omega) = \varepsilon_1(\omega) + i\varepsilon_2(\omega) \tag{3.29}$$

with n and κ being the refractive index and the extinction coefficient, respectively.

The real and imaginary parts of $\widetilde{N}(\omega)$ and $\varepsilon(\omega)$ are related as:

$$\varepsilon_1 = n^2 - \kappa^2, \qquad \varepsilon_2 = 2n\kappa. \tag{3.30}$$

In a solid the EM wave will be attenuated. Substituting equation (3.27) into (3.25) the expression for the damped wave (in one dimension) takes the form of [168–170]:

$$E(x,t) = E_0 e^{i[(\widetilde{N}\omega/c)x - \omega t)]} = E_0 e^{-(\kappa\omega/c)x} e^{i((n\omega/c)x - \omega t)}. \tag{3.31}$$

Here, the first exponential factor in (3.31) describes the decay of the wave in a medium. The intensity of a wave I is proportional to the square of the electric field, i.e EE^*. Comparing this to the expression for the Beer's law (equation (3.6))

$$I = EE^* = I_o e^{-\alpha x} \tag{3.32}$$

gives the relationship between the absorption coefficient α and extinction coefficient κ:

$$\alpha = \frac{2\omega\kappa}{c} = \frac{4\pi\kappa}{\lambda_w}. \tag{3.33}$$

Similarly, α can be related to the imaginary part of the dielectric function as:

$$\alpha = \frac{\varepsilon_2}{cn}. \tag{3.34}$$

Finally, for a medium with finite conductivity the important expressions for dielectric function and absorption coefficient become:

$$\varepsilon(\omega) = 1 + \frac{i\sigma(\omega)}{\omega\varepsilon_0} \tag{3.35}$$

Table 3.3: Relationships between the various response function $\varepsilon(\omega)$, $\sigma(\omega)$, and $\widetilde{N}(\omega)$

Dielectric constant $\varepsilon(\omega)$	Conductivity $\sigma(\omega)$	Refractive index $\widetilde{N}(\omega)$
$\varepsilon = \varepsilon_1 + i\varepsilon_2$ $\varepsilon_1 = 1 - \frac{4\pi\sigma_2}{\omega}$ $\varepsilon_2 = \frac{4\pi\sigma_1}{\omega}$ $n = (\frac{1}{2}((\varepsilon_1^2 + \varepsilon_2^2)^{1/2} + \varepsilon_1))^{1/2}$ $\kappa = (\frac{1}{2}((\varepsilon_1^2 + \varepsilon_2^2)^{1/2} - \varepsilon_1))^{1/2}$	$\sigma = \sigma_1 + i\sigma_2$ $\sigma_1 = \frac{\omega\epsilon_2}{4\pi}$ $\sigma_2 = (1 - \varepsilon_1)\frac{\omega}{4\pi}$ $n = (\frac{1}{2}(((1 - \frac{4\pi\sigma_2}{\omega})^2 + (\frac{4\pi\sigma_1}{\omega})^2)^{1/2} + (1 - \frac{4\pi\sigma_2}{\omega})))^{1/2}$ $\kappa = (\frac{1}{2}(((1 - \frac{4\pi\sigma_2}{\omega})^2 + (\frac{4\pi\sigma_1}{\omega})^2)^{1/2} - (1 - \frac{4\pi\sigma_2}{\omega})))^{1/2}$	$\widetilde{N} = n + i\kappa$ $\varepsilon_1 = n^2 - \kappa^2$ $\varepsilon_2 = 2n\kappa$ $\sigma_1 = \frac{n\kappa\omega}{2\pi}$ $\sigma_2 = (1 - n^2 + \kappa^2)\frac{\omega}{4\pi}$

and

$$\alpha = \frac{\sigma_1}{n\varepsilon_0 c}. \tag{3.36}$$

The conductivity $\sigma(\omega)$ is also a complex function with real σ_1 and imaginary σ_2 components.

Table 3.3 gives a summary of the important relationships between the various response functions $\epsilon(\omega)$, $\sigma(\omega)$, and $\widetilde{N}(\omega)$. [168–170]

3.2 Spectrometers

3.2.1 Bruker IFS 113v and Equinox 55 FTIR spectrometers

Two types of instruments, Bruker IFS 113v Fourier Transform Infrared (FTIR) spectrometer and Bruker IRscope II combined with Bruker Equinox 55 FTIR spectrometer were employed for the majority of the infrared investigation in this work. Each spectrometer contains several important compartments that include: source, interferometer, sample, and detector. The essential component of any FTIR spectrometer is the interferometer. Most of the spectrometers used today have interferometers

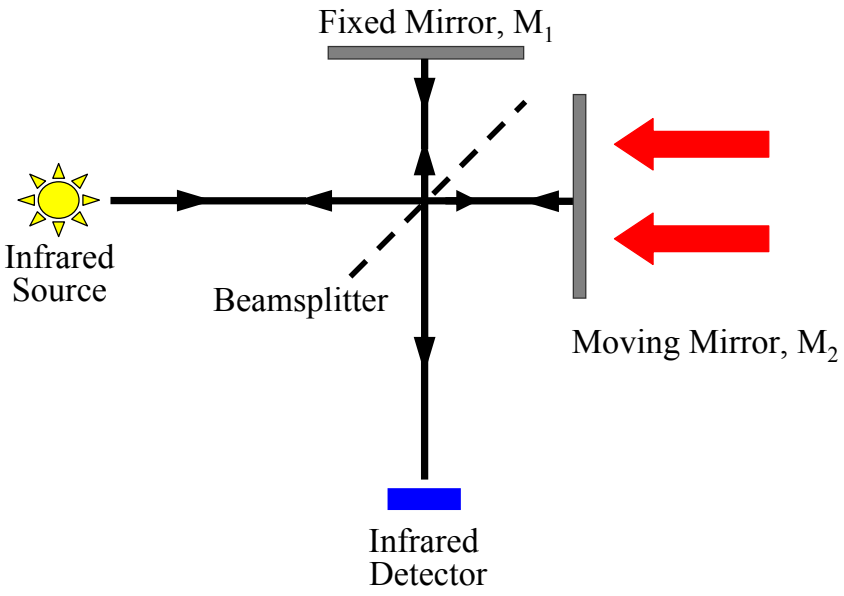

Figure 3.6: Michelson interferometer, schematic view. [172]

designed on the basis of the two-beam interferometer originally invented by Albert Michelson in 1980s. [171] There are many modifications of interferometers that are currently available to address specific applications however, general theory and insight in their operation can be readily understood from basic principles of Michelson interferometer.

a) Michelson interferometer

A schematic diagram of Michelson interferometer is shown in Fig. 3.6. The main purpose of the interferometer is to introduce a path difference between two beams of light and produce an interference pattern. [172] Here, the incident beam of radiation from the external source is split into two parts by a beamsplitter. Half of the radiation is transmitted by the beamsplitter and falls to the movable mirror M_2. The other half is reflected onto the fixed mirror M_1. Both beams return again to the beamsplitter where they recombine. Part of the recombined light returns to the source, while the other part of the recombined beam proceeds through the sample

compartment to the detector. The intensity of the recombined beams $I(x)$ (interferogram function) depends on the path difference between two mirrors, M_1 and M_2 (i.e constructive/destructive interference will take place). The plot of $I(x)$ as a function of the moving mirror displacement x is known as an interferogram. [171,172] Depending on the mirror velocity there are two types of the interferometers: a continuous scan interferometer (mirror moves at constant velocity) or step-scan interferometer (mirror stays at equally spaced points for a short period of time and then moves rapidly between these points). If M_2 travels at a constant velocity, the relationship between the interferogram function $I(x)$ and the source intensity $B(\omega)$ is given by:

$$I(x) = 1/2 \int_0^\infty B(\omega) cos 2\pi\omega dx,$$

where ω is the frequency in wavenumbers. $I(x)$ is the cosine Fourier transform of $B(\omega)$, and contains complete information about the spectrum. The Fourier transform of the interferogram generates the single channel reference spectrum. The typical transmittance/reflectance spectrum is taken as the ratio of the sample spectrum to the reference.

b) Bruker IFS 113v spectrometer

The Bruker IFS 113v is operated under vacuum and incorporates Genzel-type interferometer, which is similar to a Michelson interferometer. [171] The Genzel interferometer is constructed such that the light is focused onto the beamsplitter. Two beams, transmitted and reflected by the beamsplitter proceed to collimating mirrors and then reach the same reflection mirror from opposite sides. Here, as the mirror moves, the distance traveled by light in one arm increases while in the other one decreases. The difference in the optical path length obtained by Genzel interferometer is $4x$ (x is the displacement of the moving mirror) and thus is twice of that obtained

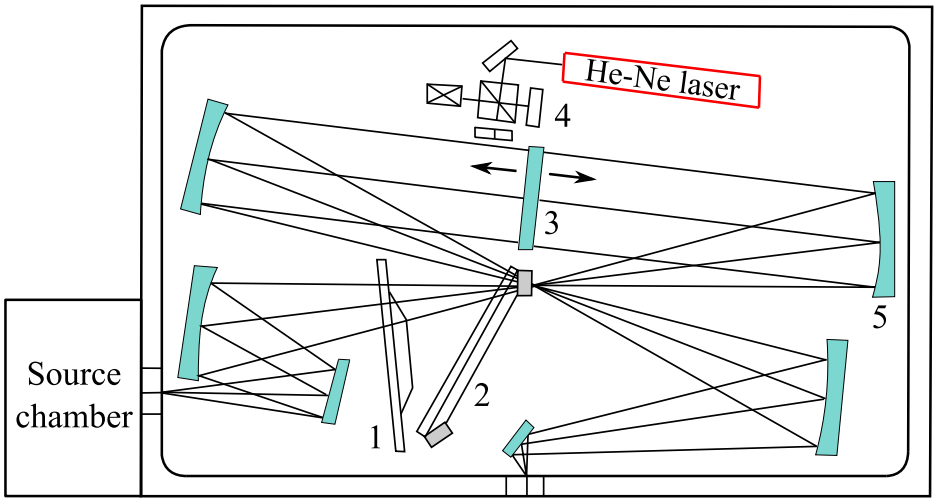

Figure 3.7: Bruker IFS 113v Genzel type interferometer: 1-filter wheel, 2-carousel with beamsplitters, 3-moving two-sided mirror, 4-reference interferometer, 5-spherical mirror. [171]

by Michelson interferometer. Another advantage of this type of the interferometer is the small size of the beamsplitter. Several of them can be mounted simultaneously on the rotating wheel and operated without breaking the vacuum. Small size also reduces unwanted vibrations associated with large diameter beamsplitters. [171] As shown on the Fig. 3.7, in the Bruker IFS 113v, there is also a secondary laser/white light interferometer physically attached to the main Genzel interferometer. The purpose of this reference interferometer is to (i) provide an "optical marker" necessary to initiate the start of spectrum data acquisition, (ii) determine the optical path difference and speed of the main moving mirror with high accuracy. The design is essential for accurate Fourier transformation.

c) Bruker Equinox 55 with microscope

Bruker Equinox 55 FTIR spectrometer in our lab is combined with Bruker IRscope II that has an advantage of studying micro size samples and precise focusing on small areas or crystal edges. There are several objectives (4×, 15×, and 36×) that give more

Table 3.4: Operating parameters of Bruker IFS 113v

Range (cm^{-1})	Source	Beamsplitter	Optical Filter	Polarizer	Detector
8-25	Hg arc	Mylar 100 μ	Black PE	1	bolometer, DTGS-PE
15-50	Hg arc	Mylar 50 μ	Black PE	1	bolometer, DTGS-PE
30-120	Hg arc	Mylar 23μ	Black PE	1	bolometer, DTGS-PE
50-240	Hg arc	Mylar 12μ	Black PE	1	bolometer, DTGS-PE
100-600	Hg arc	Mylar 3.5μ	Black PE	1	bolometer, DTGS-PE
450-4000	Globar	KBr	open	2	photocell, DTGS

PE = polyethylene. Polarizer 1 = wire grid on oriented PE, Polarizer 2 = wire grid on AgBr

flexibility in investigation of tiny sample spots. The spectrometer is operated under N_2 purge and incorporates the RockSolid interferometer. This interferometer is built with retro-reflecting cube corner mirrors that have an advantage of "correcting" any angular tilt of the flat mirrors associated with Michelson-type interferometer. This is an important addition since any tilt of the flat mirror will introduce a mismatch between two beams recombined at the beamsplitter and thus will reduce the overall quality of the data. [173]

Both spectrometers, Bruler 113v and Equinox 55 can be operated in transmittance or reflectance mode and are well suited for polarization studies. Through the appropriate combination of sources, beamsplitters and detectors spectrometers can also be used to acquire the complete spectra in infrared and visible range.

d) Source, beamsplitter, detector, and accessories

There are variety of sources, detectors, beamsplitters available for infrared spectral investigation. In general, measurements in the low frequency range (<600 cm^{-1}) are more complex and require combinations of several sources and beamsplitters. Tables 3.4 and 3.5 lists typical operating parameters used in our lab.

Silicon carbide (Globar) source is the most commonly used source in the infrared range. The emissivity of this source however becomes very weak below $\simeq$100 cm^{-1}

Table 3.5: Operating parameters of Bruker IRscope II

Range (cm^{-1})	Source	Beamsplitter	Detector
600-7500	Globar	KBr	MCT
4000-12000	Tungsten	Quartz	InSb
9000 -17000	Tungsten	Quartz	Si diode

and use of high-pressure mercury lamp is required in low frequency range. [171]

A variety of Mylar beamsplitters of different thicknesses are available for measurements of low frequency spectrum (8-400 cm^{-1}). KBr (potassium bromide) beamsplitter[2] is prevailingly used in the middle-infrared range. The spectra collected with different beamsplitters are merged together to give the whole spectrum in the frequency range of interest. [160]

Deuterated triglycine sulfate (DTGS) is the most commonly used room temperature infrared detector. [160, 171] Although it is inexpensive and very simple in maintenance and operation, the major drawback of the DTGS detector is its slow response and low sensitivity that results in poor signal-to-noise ratios. The improved sensitivity is achieved by liquid-helim and liquid-nitrogen cooled detectors such as Si (or boron-doped silicon) bolometer, MCT (mercury cadmium telluride) and/or InSb (indium antimonide) detectors. For instance, MCT detector used in our lab is 4 times faster and 10 times less noisy than MIR DTGS detector.

3.2.2 Raman instruments

The four major components that a conventional Raman spectrometer consist of, are: source of radiation (laser), sample illumination and collection optics (set of mirrors and lenses), wavelength monochromator and a detector. [158] Figure 3.8(a) displays

[2]Thin coating of Ge (germanium) sandwiched between KBr windows.

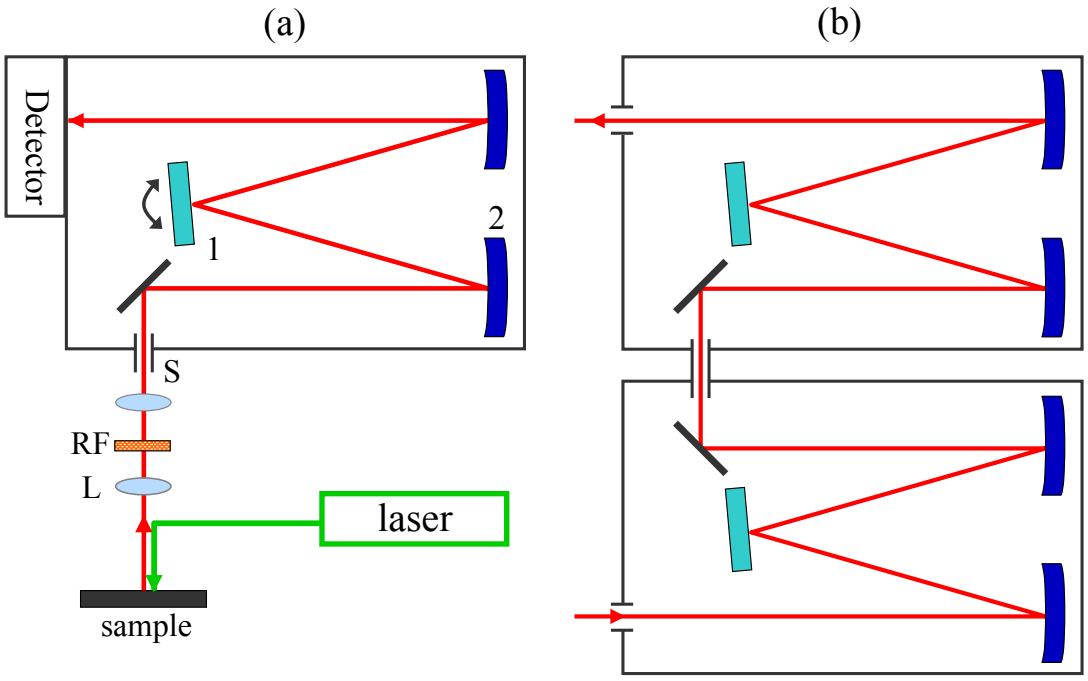

Figure 3.8: (a) Schematic representation of the Raman set-up. RF-Rayleigh filter, L-lens, S-entrance slit, 1-diffraction grating, 2-spherical mirror. (b) Schematic of the double monochromator. [158, 161]

a schematic view of a typical Raman set-up. The emitted radiation from the laser scatters from the sample, passes through the set of lenses/filters and proceeds to the entrance slit. The directed beam falls into the spherical mirror that makes the light beam parallel and further sends it to the diffraction grating. Finally, the focusing mirror directs the diffracted beam towards the detector. The rotation of the grating allows different wavelengths to be directed to the detector and thus the spectrum can be recorded. Grating and width of the slit play the key role in obtaining the maximum spectral resolution. Grating resolution is given as:

$$R_s = \frac{\lambda_w}{\Delta\lambda_w} = N \cdot m, \tag{3.37}$$

where N is the number of illuminated slits and m is the order of the diffraction. To further increases the resolution and reduce the amount of stray light that may interfere with weak Raman scattering, a tandem of monochromators can be employed. A schematic diagram of a double monochromator is shown in Fig. 3.8(b). A triple monochromator allows even better filtering/rejection of the stray light and thus can be used to measure Raman bands located very close to the Rayleigh line. Rayleigh filter (Fig. 3.8(a)) is an essential part of the Raman instrumentation that allows selective elimination of the strong Rayleigh scattering and analysis of the weak Raman scattering. High detection sensitivity and signal-to-noise ratios are achieved by the use of array detectors, usually photodiode arrays or CCD's (charge-coupled-devices). [158, 161]

3.3 Low-Temperature and High-Field Measurements

3.3.1 Low-temperature set up

The low-temperature measurements were carried out with an open-flow cryostat. Cryogenic experiments with the Bruker IFS 113v are performed in combination with an APD Heli-Tran LT-3-110 model system and for the Bruker Equinox 55 with Oxford Instruments Microstat^{He} (Fig. 3.9). [174, 175] Figure 3.10 shows a schematic diagram of the cryogenic system assembly and operation for the LT-3-110 model. The elevated pressure in the helium dewar forces a flow of liquid helium through the transfer line to the cryostat and heat exchanger. The latter serves as a cooling interface for the sample holder. After cooling the sample, the liquid helium evaporates and the gas is led away in two ways: through the helium exhaust port on the side of the cryostat and back through the transfer line with exit at the shield outlet port. This additional return/shield flow helps to keep the transfer line cold.

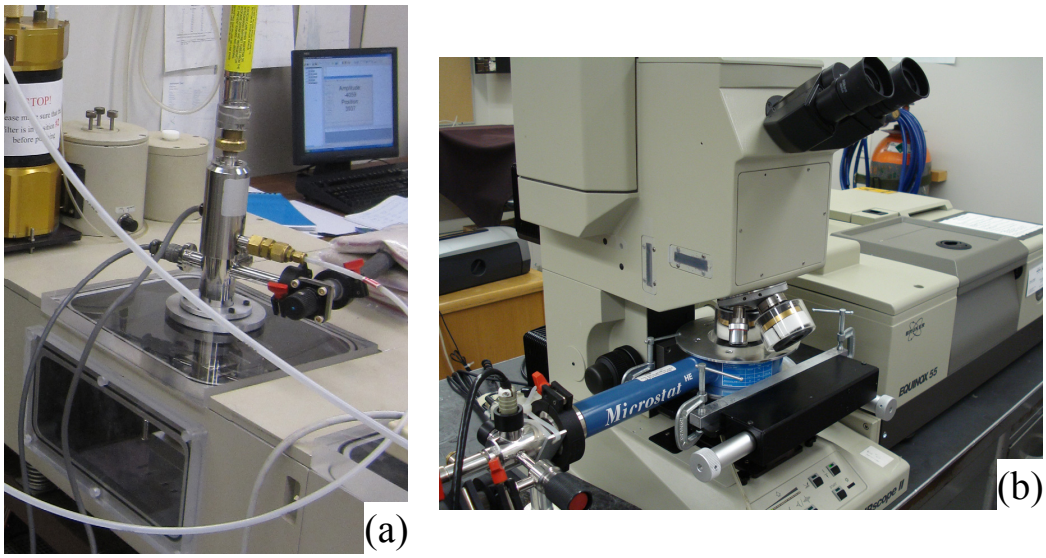

Figure 3.9: (a) and (b) Close-up views of the cryostats mounted for optical measurements in Bruker IFS 113v and Bruker Equinox 55, respectively.

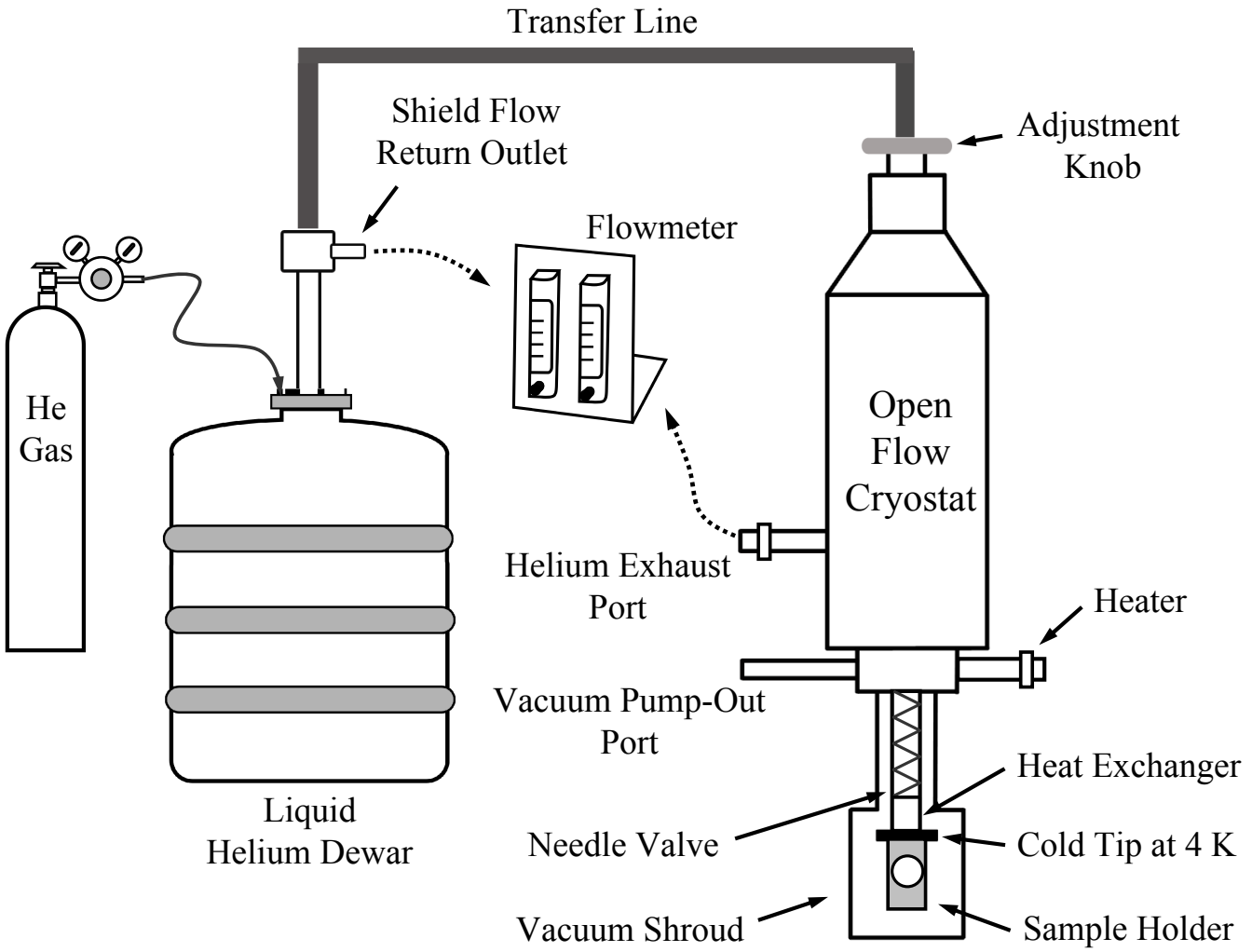

Figure 3.10: Schematic diagram of the low temperature set-up with LT-3-110 Heli-Tran open flow cryostat.

The base of the cryostat is also equipped with a heater to prevent ice buildup and vacuum seal freezing. The overall cooling rate of the sample can be regulated by (i) pressure of the supply dewar, (ii) flowmeter (attached to the helium exhaust port and shield gas outlet) and (iii) adjustment knob that controls the position of the needle valve at the end of the transfer line. The sample of interest is mounted on the heat exchanger/sample holder in vacuum and an optical access is achieved through appropriate windows (Polyethylene, KBr, KRS-5). A thermal sensor and a heater are mounted on the heat exchanger and are used to balance and control the temperature of the sample. To improve the thermal contact, crycon grease is placed between the cold stage of the cryostat and the sample holder. The sample is mounted on the sample holder with GE varnish and silver paste.

3.3.2 Experimental set-up at the NHMFL

The National High Magnetic Field Laboratory (NHMFL) offers unique opportunities to perform cutting edge research at high magnetic fields. For more information, please visit the website of NHMFL at *http://www.nhmfl.gov*. The information given in this section is largely from NHMFL website, Refs. [176–179] and our own experiments. Figure 3.11 shows a schematic representation of the magneto-infrared set-up for the 35 T resistive magnet. The emitted radiation from the IR spectrometer is directed out of the instrument towards the light pipe by an off-axis parabolic mirror. A second mirror in the light pipe, located just above the probe, further diverts the beam by 90° and sends it onto the sample located in the center of the magnet. After the light passes the sample, it is collected by a bolometer inside the probe and transformed into an electric signal. The signal is further amplified, electronically filtered, and sent back to the spectrometer to be processed by a computer. Cooling of the sample is achieved by submerging the probe directly into the liquid helium

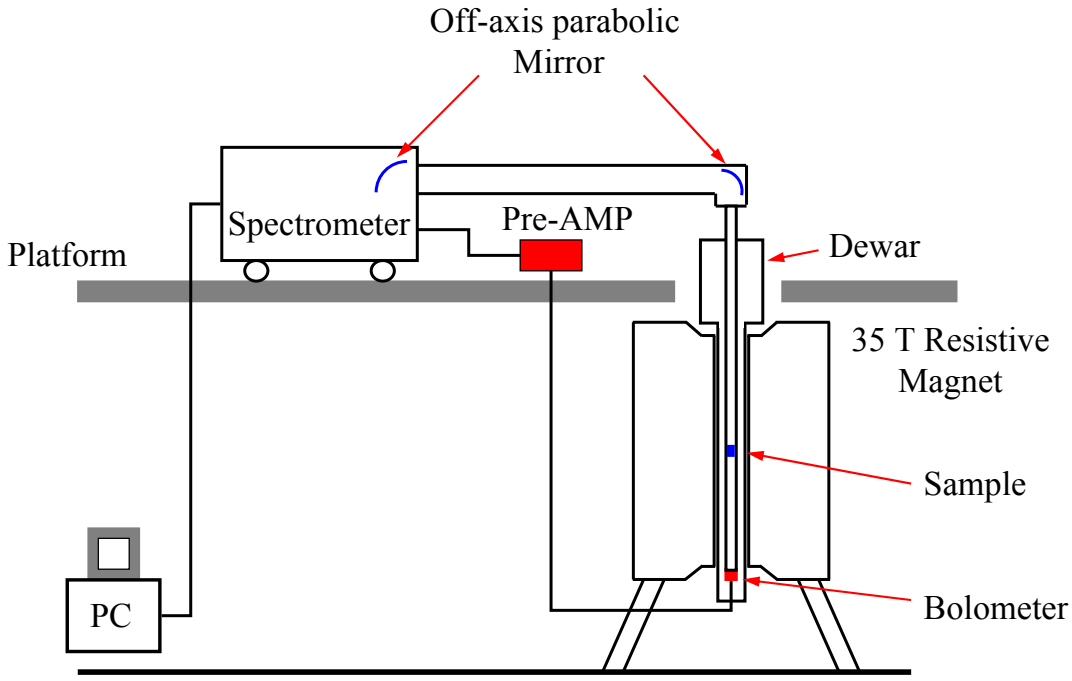

Figure 3.11: Schematic diagram of the magneto-infrared set-up at the NHMFL. [176]

bath. Helium exchange gas is employed to achieve the base temperature.

The magneto-Raman measurements were performed in a backscattering geometry using a Trivista557 triple spectrometer equipped with 1800g/mm grating. Figure 3.12 displays a schematic drawing of the magneto-Raman set-up with a 31 or 35 T resistive magnet. An optical fiber coupled to a 532 nm laser delivers the excitation light to the sample located at the bottom of the probe. The scattered light proceeds to the collection fiber connected to the spectrometer equipped with a liquid nitrogen cooled Spec10 CCD camera. [179] Temperature sensors and a heater are mounted next to the sample holder for precise monitoring and temperature control of the sample. Low temperature is achieved by either immersing the probe directly into the liquid helium bath or blowing cold helium gas through the bottom of the probe. The operating temperature range is 1.6 - 300 K.

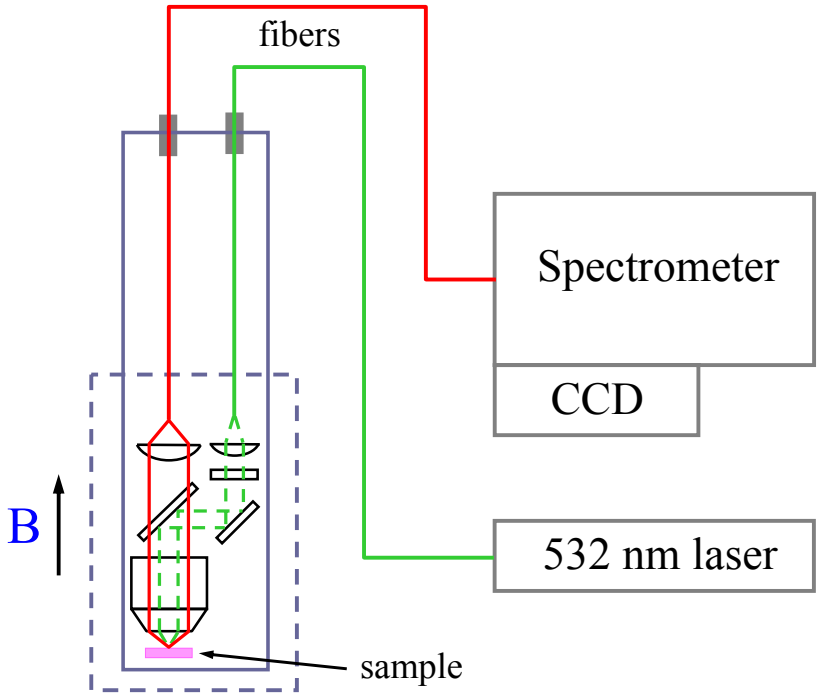

Figure 3.12: A schematic of the magneto-Raman set-up at the NHMFL. An illuminating and collecting system inside the probe is presented as a set of lenses, mirrors and filters. [179]

3.4 Materials of Interest: Measurements and Complementary Calculations

a) Synthetic procedures

The polycrystalline powders of $M(dca)_2$ (dca = $N(CN)_2^-$) materials were provided by Jamie Manson from Eastern Washington University and John Schlueter from Argonne National Laboratory. $[Ru_2(O_2CMe)_4]_3[Cr(CN)_6]$ (Me = CH_3) material was provided by Joel Miller from the University of Utah. The compounds were synthesized with solution based techniques as described previously in the literature. [51, 69, 180]

b) Spectroscopic measurements

Infrared transmittance measurements

Isotropic pellets of $M(dca)_2$ and $[Ru_2(O_2CMe)_4]_3[Cr(CN)_6]$ were prepared by mixing the original powder samples with transparent matrix materials. Pure KCl powder was used as a matrix in the middle-infrared and Raman scattering experiments, whereas paraffin was used in the far infrared regime. To achieve optimum signal and sensitivity, different loading levels were employed. Typical KCl pellets are made in vacuum with a 9 ton press. Special care was taken in case of $Co(dca)_2$ and $[Ru_2(O_2CMe)_4]_3[Cr(CN)_6]$ KCl pellets. Cobalt dicyanamide is predicted to exhibit a pressure-driven transition at $\simeq$0.9 GPa to a new monoclinc phase. [182] Formation of a blue β-phase under pressure is also possible. Therefore, all the pellets were made at pressure of 0.5-0.6 GPa (well below the pressure-driven transition) and checked against unpressed sample spectra. In addition, visual inspection combined with detailed spectroscopic characterization were used to confirm the α-phase nature of our samples and rule out β-phase impurity formation under pressure. Figure 3.13

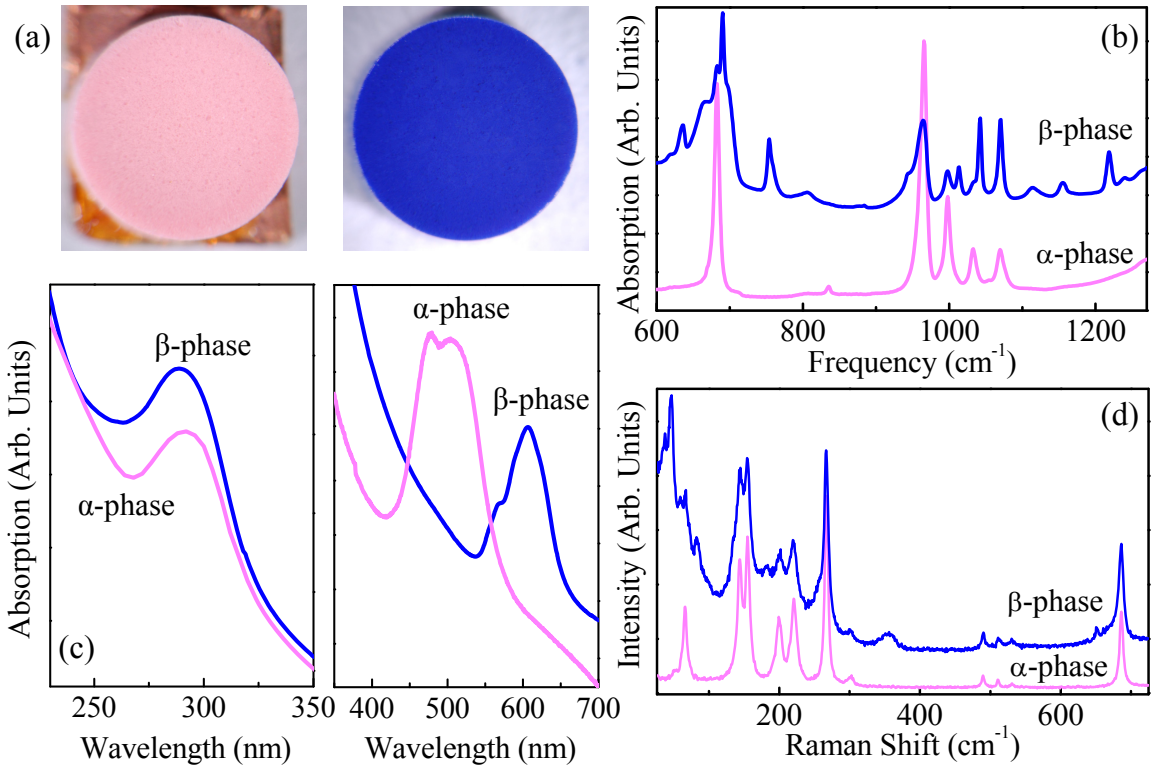

Figure 3.13: (a) Photographs of the pink α- and blue β-forms of $Co(dca)_2$ in KCl. (b, d) Comparison of selected infrared and Raman (λ_w=514 nm) modes for the two phases. The spectra are offset for clarity. (c) Characteristic color band excitations of the α-phase compound near 295, 474 and 518 nm and the 293, 563 and 607 nm absorptions for the β-phase material. [69,70,181] All spectra were measured at room temperature.

compares the α- and as-synthesized β- forms of $Co(dca)_2$ in pressed KCl pellets. Clearly, the two phases are quite different and are easily distinguished according to their vibrational and electronic properties. No β-compound signatures were detected in our samples.

In case of $[Ru_2(O_2CMe)_4]_3[Cr(CN)_6]$ sample, all studied samples displayed some degree of decomposition evident from the appearance of the broad infrared absorption lines in $\simeq$ 1550 and 2080-2090 cm^{-1} regions. [93] The latter does not seem to impact the bulk magnetic properties – either in previous work or in our own measurements. Special care was required, however, for the spectroscopic studies. We found, for instance, that in an alkali halide environment, pressure increases the decomposition rate and thus, as in cobalt dicyanamide, reduced pressure was used for KCl pellet preparation. In addition, to reduce decomposition signatures and access the intrinsic spectral response, magnetic field- and temperature-dependent behavior of the CN vibration at $\simeq$2145 cm^{-1} were checked in an unconventional arrangement (employing a paraffin matrix) and after appropriate background subtraction, found to be consistent with the KCl pellet response. Only after such extensive tests were results regarded as reliable. Our general conclusion is that the vibrational bands characteristic of the decomposition-induced defect states are magnetically inactive.

Spectral resolution of 0.3-1 cm^{-1} was employed for infrared experiments. High field measurements were performed at the NHMFL swiping the field up and down and taking the data in turns, at high and low fields. No spectral hysteresis was observed. The absorption coefficient $\alpha(\omega)$ was calculated from the measured transmittance as $\alpha(\omega) = -\frac{1}{h_s d}\ln(\mathcal{T}(\omega))$, where h_s is sample loading and d is thickness.

Magneto-Raman experiments

Samples used in Raman measurements were in the form of pressed pellets of either pure or KCl mixed sample. The same precaution with pressure as in infrared

measurements was employed. Measurements were performed at the NHMFL using a powered magnet of 31 or 35 T. A 532 nm laser was focused on the sample spot size of $\simeq$20 μm with a power of $\simeq$1.5 mW. Typical resolution was 0.5-1 cm^{-1}. Data were collected with increasing field, and checked against several reference points with decreasing field. Results were found to be the same.

All spectroscopic investigations in high magnetic fields were performed with assistance of Li-Chun Tung, Dmitry Smirnov, Yongjie Wang and Younghee Kim.

c) Magnetization measurements

Isothermal magnetization was measured at the NHMFL Pulsed Magnet Facility at Los Alamos National Laboratory by John Singleton (LANL) and Jamie Manson (EWU) using the set-up described by Goddard *et al.* along with a 65 T short-pulse magnet. [53] Data were collected at temperatures ranging from 0.5-20 K.

d) Lattice dynamics calculations

Theoretical calculations of vibrational frequencies and displacement patterns were done by Alexander Litvinchuk from the University of Houston. Density functional calculations of the electronic ground state were performed within the generalized-gradient approximation using revised Perdew-Burke-Ernzerhof [183] functionals, as implemented in the CASTEP code. [184] The norm-conserving pseudopotentials were used. For self-consistent calculations of the electronic structure the integration over the Brillouin zone was performed over the 1×2×1 Monkhorst-Pack grid in the reciprocal space. [185] The lattice vibrations of $Mn(dca)_2$ were calculated with the linear response method. [186] Mode movies allowed us to visualize the calculated displacement patterns.

e) $Mn(dca)_2$ complementary calculations

Complementary calculations for $Mn(dca)_2$ were carried out by Mike Whangbo at North Carolina State University. In the study of the magnetic structure of $Mn(dca)_2$, spin-polarized density functional calculations were carried out using the projector augmented wave method implemented in the Vienna *ab initio* simulation package [187–189] with the generalized gradient approximation (GGA) [190] for the exchange-correlation functional, the plane-wave cutoff energy of 500 eV, a set of 12 k-points for the irreducible Brillouin zone, and the threshold 10^{-6} eV for energy convergence. Spin density was calculated based on the optimized structure with AFM and FM spin-arrangements, respectively.

f) $Co(dca)_2$: analysis of magnetic properties

Fits to the magnetization and magnon energy calculations were carried out by Jason Haraldsen from the Los Alamos National Laboratory. Calculations were performed using a mean-field approximation and considering the ferromagnetic state and large anisotropy of the cobalt system (Appendix B).

Chapter 4

Quantum Critical Transition Amplifies Magnetoelastic Coupling in $Mn(dca)_2$

Chapter 4 is an adaptation of the research article by T. V. Brinzari *et al.* "Quantum critical transition amplifies magnetoelastic coupling in $Mn[N(CN)_2]_2$", Ref. [191]. To be submitted to an *ACS* journal. Authors' contributions are described in Chapter 3.

In this work, we combined magnetization and magneto-infrared spectroscopy along with spin density and lattice dynamics calculations to explore the properties of the molecule-based magnet $Mn(dca)_2$. We discovered a magnetic quantum critical transition at 30.4 T that drives the system from the canted antiferromagnetic state to the fully polarized state and amplifies magnetoelastic coupling as an intrinsic part of the process. The local lattice distortions, revealed through systematic phonon frequency shifts and detailed analysis of displacement patterns, suggest a combined MnN_6 octahedra distortion + counter-rotation mechanism that reduces antiferromagnetic interactions and accommodates the field-induced state. These find-

ings deepen our understanding of magnetoelastic coupling near a magnetic quantum critical point.

4.1 High Field Quantum Phase Transition in $Mn(dca)_2$

Figure 4.1(a) displays the isothermal magnetization of $Mn(dca)_2$ as a function of magnetic field up to 51 T. The base temperature data shows a linear increase with field above the 0.48 T spin flop transition and a sharp, "elbow-like" transition to saturation at $B_c = 30.4 \pm 0.1$ T where the fully polarized state is achieved. The 4 K data has a similar profile and a 29.8 ± 0.2 T saturation field. This behavior is a signature of a magnetic quantum critical transition. [53, 192] That it occurs at experimentally realizable fields makes it especially attractive. The magnetization in $Mn(dca)_2$ has some similarities with the series of Cu-based metal-organic magnets investigated by Goddard *et al.*, [53] although the linear response in the canted phase of $Mn(dca)_2$ is different than the concavity in the lower dimensional systems. We use mean field theory to relate the observed critical field (B_c) to the exchange interaction as $g\mu_B B_c = |z(2JS)|$. Here, $S = 5/2$ for Mn^{2+}, $z = 8$ is the number of nearest neighbors, $g = 2.0$, and μ_B is the Bohr magneton. We find $J/k_B = -1.0$ K, which compares well with the estimate of $J/k_B = -0.78$ K from heat capacity measurements[1]. [73] Bringing the extracted critical fields together with previously published work [74] allows us to construct the $B-T$ phase diagram (Fig. 4.1(b)). Interestingly, a single value of J cannot simultaneously account for both magnetic energy scales in this system ($T_N = 15.85$ K and $B_c = 30.4$ T). Possible origins include "beyond mean field" corrections [193] or a field-dependent exchange interaction. [248] Spin density calculations reveal an out-of-phase pattern in the low field antiferromagnetic state

[1]Definition of J used in Ref. [73] differs by a factor of 2 from the one used in our work, so we multiply - 0.39 K by 2 for a comparison. Note that some uncertainties in this J may be present due to the challenges in subtracting the lattice contribution to the heat capacity data.

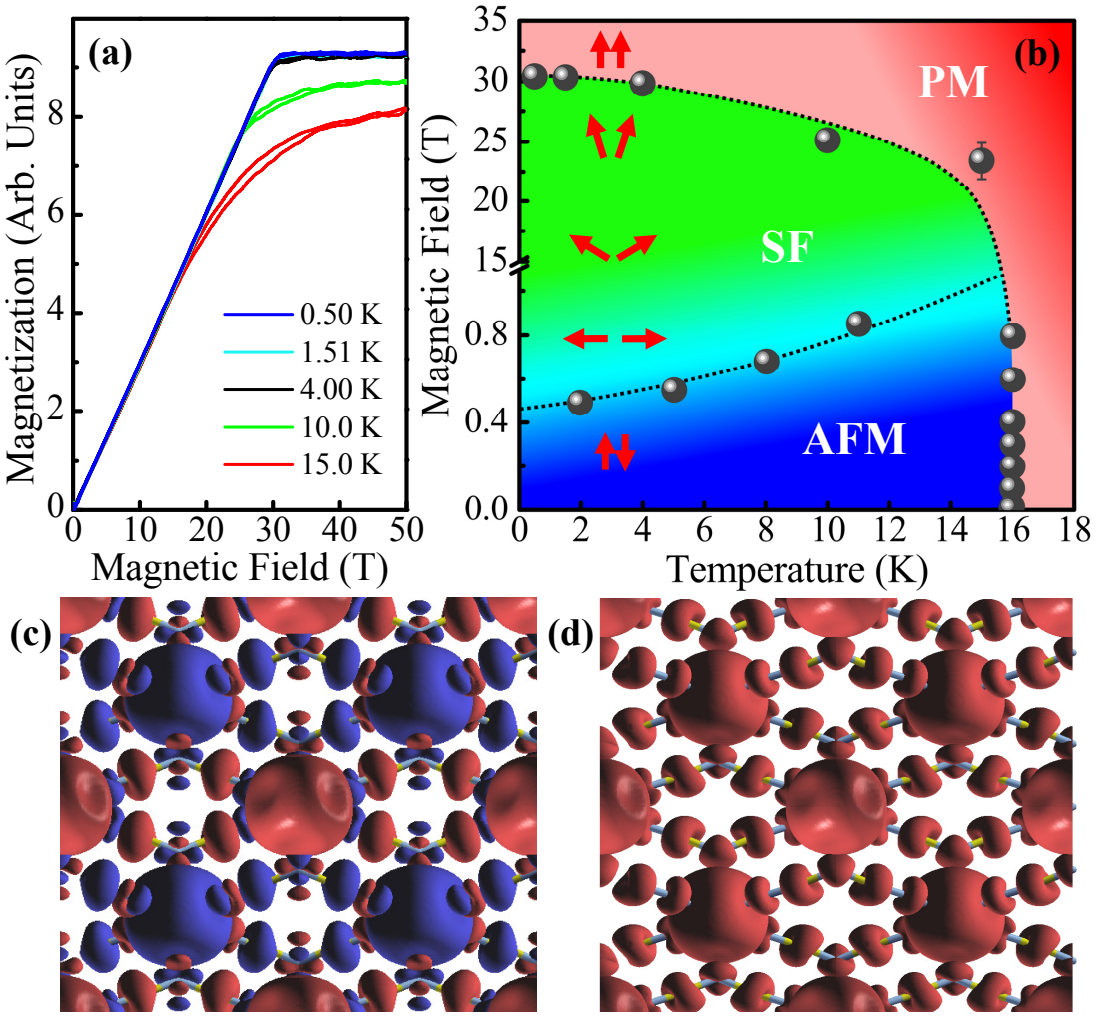

Figure 4.1: (a) Isothermal magnetization of $Mn(dca)_2$. (b) Comprehensive $B-T$ phase diagram displaying antiferromagnetic (AFM), spin-flop (SF), and paramagnetic (PM) phases. The dashed lines guide the eye. Arrows indicate schematic spin configurations for the vertical field. (c, d) Calculated spin density distribution for antiferromagnetic and ferromagnetic states of $Mn(dca)_2$, respectively.

and a uniform density in the high field state (Fig. 4.1(c, d)), with the majority of spin density on the Mn sites in each case.

4.2 Lattice Dynamics and Magneto-Structural Correlations Probed by Infrared Spectroscopy

Figure 4.2(a) displays the low temperature absorption spectrum of $Mn(dca)_2$.[2] A factor group analysis (space group (58) *Pnnm*) predicts 25 infrared active modes $\Gamma = 7B_{1u} + 9B_{2u} + 9B_{3u}$. Based on complementary first principles lattice dynamics calculations and a literature comparison, [194–196] we assign the peaks at 79 and 108 cm^{-1} to lattice modes with dominant Mn displacement, vibrations at 162/167 and 194 cm^{-1} to NMnN bending, features between 220 and 300 cm^{-1} to Mn-N stretching modes + ligand bands, and peaks at around 500 cm^{-1} to NCN in- and out-of plane bending. A complete assignment is presented in Table 4.1. As we shall see, assignment of the field-dependent vibrational modes and an understanding of their displacement patterns is key to teasing out the local lattice distortions and establishing structure-property relationships.

The magneto-infrared response of $Mn(dca)_2$ reveals remarkable sensitivity to the quantum critical transition. To emphasize spectral changes through B_c, we calculated the full field absorption difference spectrum, $\Delta\alpha = \alpha(B = 35\ \mathrm{T}) - \alpha(0\ \mathrm{T})$ (Fig. 4.2(b)).[3] This difference simultaneously highlights striking change and rigid behavior. The exact course of each mode depends on the precise nature of its displacement pattern. Moreover, the field-dependent features either soften or harden systematically with field, a trend that again correlates with the detailed mode mo-

[2]The complete infrared spectrum at 4.6 and 300 K is provided in Appendix A.

[3]Small changes in absolute absorption spectrum sometimes are hard to track, so we use absorption difference to emphasize changes with applied magnetic field.

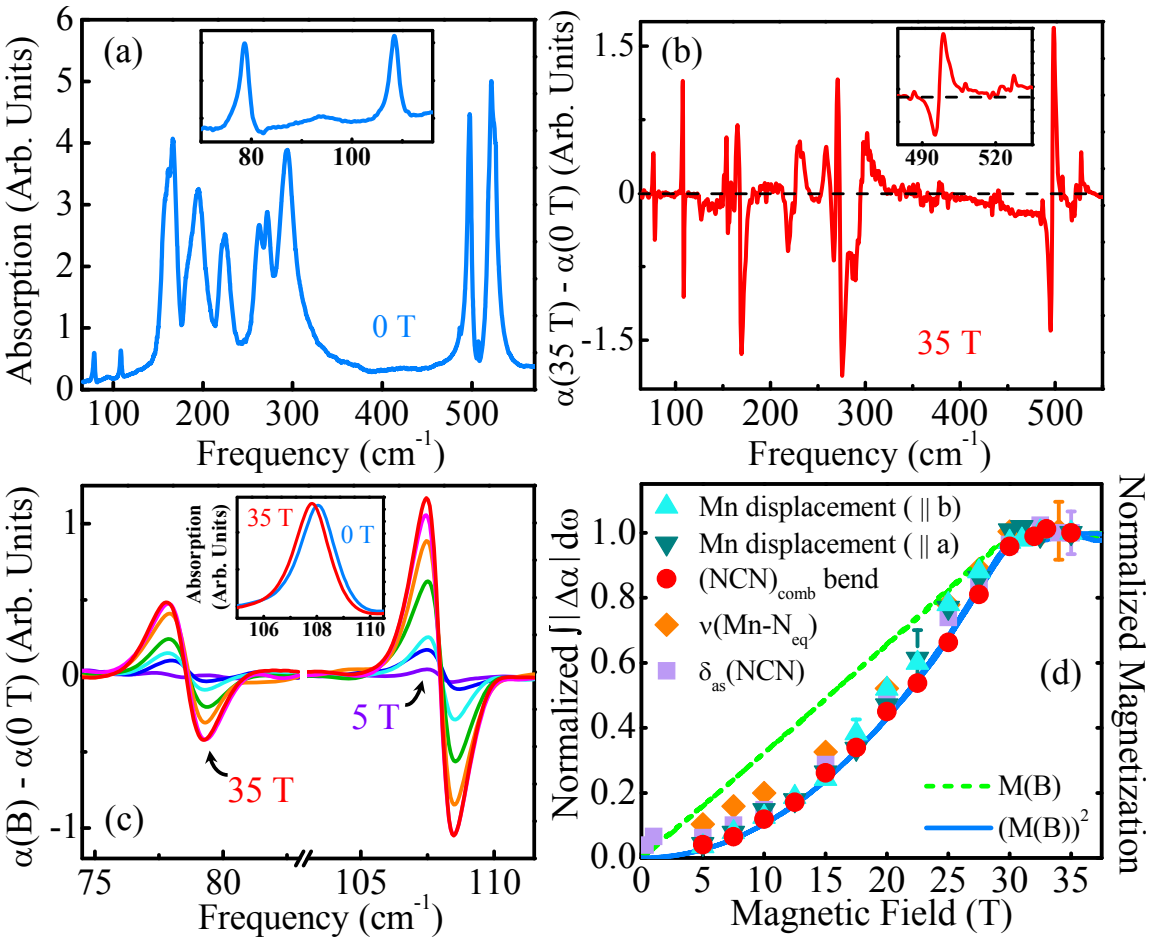

Figure 4.2: (a) $Mn(dca)_2$ absorption spectrum in the far-infrared. Inset: close-up view of the two low frequency Mn displacement modes. (b) Absorption difference spectrum at $B = 35$ T. Inset: close-up view of the absorption difference in the (NCN) bending regime. (c) Close-up view of the absorption difference for the 79 and 108 cm^{-1} lattice modes at 5, 10, 15, 20, 25, 30 and 35 T. The inset highlights the absolute absorption spectrum at 0 and 35 T for the 108 cm^{-1} peak. (d) Normalized integrated absolute absorption difference for several characteristic features as a function of applied field compared with magnetization and the square of the magnetization. All data were measured at liquid helium temperature.

Table 4.1: Assignment of experimentally observed and calculated infrared-active modes for $Mn(dca)_2$ along with the size of the field-induced changes in $|\Delta\alpha|/\alpha$=|(α(35 T) - α(0 T))|/α(0 T) at 4.6 K. Error bars on $|\Delta\alpha|/\alpha$ are $\leq$0.7%.

4.6 K experimental frequency (cm^{-1})	Calculated frequency (cm^{-1})	Symmetry	Assignment	$\lvert\Delta\alpha\rvert/\alpha$, %
79 (w)	82	B_{3u}	lattice mode: Mn displacement along a axis	12 (soften)
108 (w)	88	B_{2u}	lattice mode: Mn displacement along b axis	29 (soften)
162, 167 (m)	183, 197	B_{2u}, B_{3u}	(N_{ax}-Mn-N_{ax}) bends	4 (soften)
194 (m)	230	B_{1u}	(N_{eq}-Mn-N_{eq}) out-of-plane, out-of-phase bend	
224 (m-w)	239	B_{3u}	$\sim$ ν(Mn-N_{eq}) (Mn motion in ab plane) + $\sim$ ν(Mn-N_{ax}) (N, C motion in ab plane)	3 (harden)
263 (m-w)	247	B_{2u}	$\sim$ ν(Mn-N_{ax}) + $\sim$ ν(Mn-N_{eq}) (Mn along a, N_{ax}, C in ab plane)	3 (soften)
272 (m-w)	280	B_{1u}	ν(Mn-N_{eq}) balanced by C motion	7 (soften)
294 (m)	309, 313, 320, 333, 347	B_{2u}, B_{1u}, B_{3u}, B_{3u}, B_{2u}	ligand bands (mostly N motion in-plane and out-of-plane: scissors, rocking, wagging)	2 (harden)
494 (sh)	511	B_{1u}	γ_{as} (NCN)	
497 (m)	513	B_{1u}	δ_{as} (NCN)	5 (harden)
522, 526 (m)	526, 527	B_{2u}, B_{3u}	γ_s (NCN)	0.3, 0.8 (harden)
680 (m)	642, 643	B_{2u}, B_{3u}	δ_s (NCN)	4 (harden)
961 (m)	900, 904	B_{3u}, B_{2u}	ν_s (N-C), N motion also modulates Mn-N_{ax} bond	–
996 (m-w)			(NCN) bend, IR + Raman*	14 (harden)
1042 (w)			(NCN) bend, IR + Raman*	7 (harden)
1065 (w)				4 (harden)
1115 (w)				
1321 (s)	1226	B_{1u}	ν_{as} (N-C), in phase N motion along c axis	4 (soften)
2167 (m-s)				–
2203 (vs)	2066	B_{1u}	ν_{as} (C$\equiv$N)	1 (harden)
2248 (w)				–
2267 (vs)			ν_s (N-C) + ν_{as} (N-C), IR + Raman	6 (harden)
2296 (s), 2324 (m)	2112, 2116	B_{2u}, B_{3u}	ν_s (C$\equiv$N)	–

ν = stretch, γ = out-of-plane bend, δ = in-plane bend.
vw: very weak, w: weak, m: medium, s: strong, vs: very strong, sh: shoulder.
Broad features above 3000 cm^{-1} are assigned as various combination bands of ν(N-C) + ν(C$\equiv$N).
* 1st overtone is symmetry forbidden.

tion. In fact, at heart, $\Delta\alpha$ changes are frequency shifts.[4] As an example, Fig. 4.2(c) displays a close-up view of the absorption difference spectrum for the two low frequency Mn displacement modes. The magnitude of $\Delta\alpha$ increases continuously due to mode softening until it saturates near 30 T. That the majority of the vibrational bands are sensitive to applied field is indicative of the local structure deformations on approach to the magnetic transition. In the discussion below, we focus on the most pronounced spectral changes and what they reveal about the field-induced local lattice distortion.[5]

To quantify changes in the vibrational properties of $Mn(dca)_2$ with magnetic field, we integrate the absolute value of the absorption difference as $\int_{\omega_1}^{\omega_2} |\alpha(B) - \alpha(0\ \mathrm{T})|\, d\omega$ for several representative modes and plot these values along with the magnetization (Fig. 4.2(d)). The field-induced spectral changes grow with increasing field and saturate near 30 T where the transition from canted antiferomagnetic to fully polarized state is complete.[6] In general, magnetoelastic phenomena originate from the magnetic state dependence of the elastic properties, which can vary with magnetization intensity and orientation. For instance, in magnetic alloys, the relationship between volume magnetostriction and magnetization goes as $\frac{\Delta V}{V} \sim ((M(B))^2)$. [197–199] Lattice constants in complex oxides like $BaCo_2V_2O_8$ also display similar dependence. [200] Our work is different in that we employ local probe (rather than bulk) techniques to reveal the microscopic aspects of the local lattice distortion. Comparison of the data in Fig. 4.2(d) shows that $Mn(dca)_2$ is an example of a molecule-based magnet where the field-induced frequency shifts go as $(M(B))^2$, an indication of dominant exchange effects. The strong correlation between the phonon behavior and the

[4]Note that absorption difference takes into account changes in frequency, linewidth and intensity, however, no systematic effects in integrated intensity or linewidth are apparent in our experiment.

[5]The majority of leading modes are located at low frequency, although similar behavior is also observed in the higher frequency modes.

[6]No apparent changes are observed at spin-flop transition at around 0.5 T within our sensitivity. When normalized, all modes show the same trend within our error bars.

square of the magnetization through the magnetic quantum phase transition suggests that lattice flexibility plays an important role in establishing the fully polarized high field state. Similar measurements on the isostructural $Cu(dca)_2$ analog, which is a paramagnet at 4.2 K, show no changes within our sensitivity, indicating that the lattice is essentially rigid with field.[7] [79] These complementary studies demonstrate that magnetoelastic coupling in $Mn(dca)_2$ is associated with the collective phase transition.

Our spectroscopic measurements reveal that some local structure changes are more important than others. In other words, although many infrared-active phonons are sensitive to applied field and display a similar dependence on B, the magnitude of their change through the field-driven transition is not the same. We use relative absorption difference, $|\Delta\alpha|/\alpha$, to quantify the importance of each mode and the local lattice distortion that it represents. The features at 108, 79, and 272 cm^{-1} display the largest changes ($\simeq$29, 12, and 7% in a 35 T field, respectively). The two leading modes involve Mn displacements in a shearing-like pattern along b (108 cm^{-1}) and a (79 cm^{-1}) axes, respectively. The next tier contribution (272 cm^{-1} Mn-N_{eq} vibration with a 7% change) also mainly involves Mn motion but along the c axis. All three modes soften gradually with increasing field. Figure 4.3 displays schematic views of these displacement patterns along with an example of pure ligand mode motion at 497 cm^{-1} with 5% change in field. Several infrared + Raman combination bands (for instance, at 996 and 2267 cm^{-1}, Fig. 4.2(d)) are also very sensitive to the 30.4 T quantum critical transition and suggest the likelihood of a similar magneto-Raman response. While these modes are strongly coupled to the magnetic quantum critical transition, other features (for instance, at 194, 526, 961 and $\simeq$2300 cm^{-1}) are essentially rigid. An example is shown in the inset of Fig. 4.2(b). Here, the out-

[7] Measurements were done in the far infrared range.

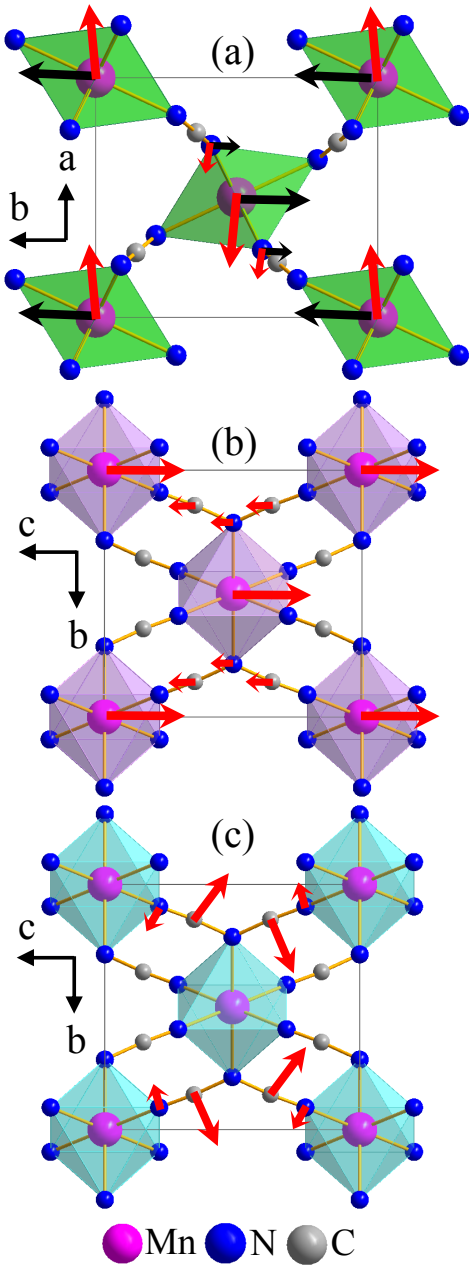

Figure 4.3: Schematic view of representative displacement patterns as predicted by lattice dynamics calculations. Panel (a) shows the calculated Mn displacement patterns that we assign to the 79 and 108 cm^{-1} infrared peaks, panel (b) displays υ(Mn-N_{eq}) assigned to the 272 cm^{-1} peak, and panel (c) shows the in-plane asymmetric δ_{as}(NCN) bend that corresponds to the experimental peak at 497 cm^{-1}. Only the representative arrows of the building units are shown.

of-plane NCN bend displays a strikingly different behavior compared to its in-plane counterpart, indicating that the symmetry of out-of-plane motion undermines the dominant distortion.

A natural framework for understanding the magnetoelastic effect in $Mn(dca)_2$ involves local lattice deformations that modify spin exchange interactions in order to compensate for the increased magnetic energy in the fully polarized state. Analysis of the absorption difference spectra reveals that phonons involving mainly Mn center generally soften with field and, the ligand bands on the contrary, tend to harden on approach to the transition (Table 4.1). This behavior points to a more relaxed MnN_6 octahedra (i.e less strained bond lengths and equally distributed local angles) and slightly compressed NCN linkages in the high field state. Based upon the size of $|\Delta\alpha|/\alpha$ through the 30.4 T magnetic quantum phase transition, the distortion primarily affects the 108 cm^{-1} Mn shearing mode along b (with a 29% change). A similar displacement pattern along a (as represented by the 79 cm^{-1} mode and its 12% change) is a large secondary effect. But why does field-induced transition impact the Mn displacement modes so strongly? Is it because there is a real space Mn displacement along b and a or is it due to a more complicated distortion of the MnN_6 cage? One way to distinguish between the displacement and octahedral deformation pictures is to investigate the peak splitting patterns. Our magneto-infrared spectra provide no evidence for high field symmetry breaking (Fig. 4.2(c)), a finding that rules out simple transition metal center displacement and also the possibility of high field ferroelectric state.[8] [201] We therefore conclude that the primary local lattice distortions through the 30.4 T magnetic quantum phase transition involve deformations of the Mn environment, specifically distortions to the MnN_6 octahedral cage.

[8]No evidence of symmetry breaking within our resolution indicates that if displacement of the Mn from the equilibrium position is present than it should be rather small.

The analysis of high magnetic field data reveals that besides Mn displacement modes, many ligand bands are sensitive to the 30.4 T quantum critical transition. While these changes are not large in terms of $|\Delta\alpha|/\alpha$ (Table 4.1), they can provide important information on modeling various structural effects found in $Mn(dca)_2$. One mechanistic candidate advanced by our first principles calculations and supported by variable temperature structure work [73] is MnN_6 counter-rotation about the c-axis. A schematic view of the octahedral counter-rotation process is shown in Fig. 4.4. It is a well-known distortion pathway for many materials. [201–205] Analysis of the spectral changes in $Mn(dca)_2$ suggests that this is a reasonable model that brings changes in the various MnN_6 and ligand bands together - with the caveat that the MnN_6 octahedra are flexible during counter-rotation due to the three-dimensional network as discussed above. Importantly, our lattice dynamics calculations reveal that the lowest frequency Raman-active vibration has a displacement pattern that mirrors the predicted MnN_6 counter-rotation (Fig. 4.4), providing a natural distortion pathway for the system.[9] Comparison of the relaxed structures of $Mn(dca)_2$ in the antiferromagnetic and ferromagnetic states suggests however, that the rotation will be very small - smaller than 1°. The theoretically predicted Raman phonon frequencies, their symmetries and assignment along with the 300 K Raman spectrum are provided in Appendix A.

The magnetic ground state in $M(dca)_2$ systems is well-known to arise from a delicate balance between competing antiferromagnetic and ferromagnetic superexchange interactions. [75] Superexchange strength depends upon the magnetic orbital overlap in the metal-ligand-metal linkage, which in turn varies with structural parameters such as bond angles and distances. [206] Angular effects are generally recognized to

[9]Unfortunately, a direct check on this process (and the behavior of the low frequency Raman active mode) is impossible at this time due to the limited frequency range of the probe (with the 35 T resistive magnet) at the NHMFL.

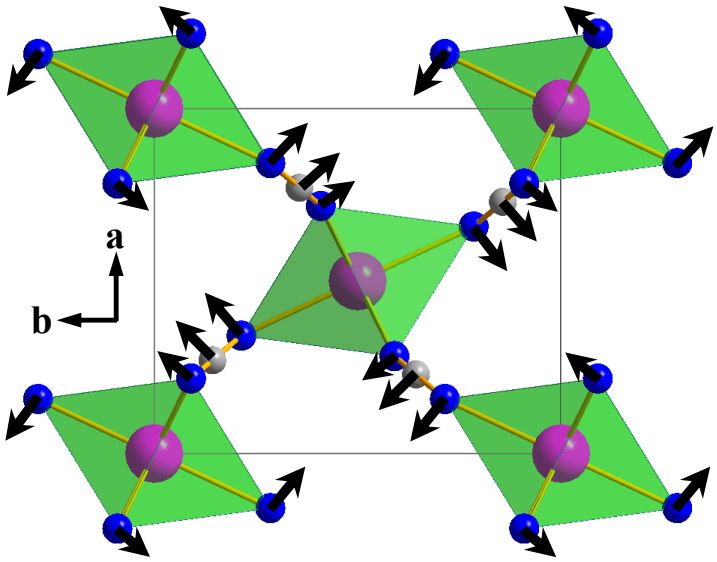

Figure 4.4: A schematic diagram for the theoretically predicted 82 cm^{-1} A_g Raman mode with the octahedra counter-rotation displacement pattern. This displacement provides a natural distortion pathway for the magnetoelastic effect observed in high magnetic field.

be of greater importance than physical distance. To see how MnN_6 counter-rotations change Mn$\cdots$Mn interactions through the 30 T quantum phase transition, we examined the orbital overlap along the main Mn-N≡C-N-Mn superexchange pathway where magnetic orbitals on the metal center overlap with high-lying π_y- and σ-type ligand orbitals. [207] A symmetry analysis suggests that the $t_{2g}(d_{xz}, d_{yz})$–π_y–t_{2g} and $t_{2g}(d_{xy})$–σ–e_g superexchange pathways can be reduced by MnN_6 octahedral rotation. Expressing the total spin exchange J as a sum of J_{FM} and J_{AFM} allows us to understand this relationship in greater detail. Here, J_{FM} is the ferromagnetic contribution, and J_{AFM} is the antiferromagnetic term. Importantly, $J_{\mathrm{AFM}} \sim \frac{t^2}{U_{eff}}$, where t is the hopping (overlap) integral, and U_{eff} is the effective on-site Coulomb repulsion. [208,209] As the field-driven magnetic quantum critical transition forces the system to adopt a fully polarized spin alignment, the energy can be reduced by lattice distortions that effectively decrease t. This reduces J_{AFM}, and consequently, the overall J.

Within this picture, MnN_6 counter-rotation occurs to lower the total energy of

the paramagnetic state forced upon the system by the external magnetic field. Using the prior result [73] that the octahedral tilt is 25.2° at 4.6 K and $B = 0$ T, driving the system into the high field state yields for instance poorer t_{2g}-π_y overlap and a slight increase in the tilting angle.[10] Thus one might speculate that the MnN_6 octahedra counter-rotate to reduce J_{AFM} in the high field state. However, the exchange parameter J of $Mn(dca)_2$ calculated for the antiferromagnetic and ferromagnetic states are practically identical. Perhaps the simplest experimental verification of the MnN_6 tilting process can be seen in the hardening behavior of the NCN bending modes at high field. An additional angular effect that influences the magnetic properties of $Mn(dca)_2$ is distortion of the MnN_6 octahedra. Softening of the 272 cm^{-1} Mn-N_{eq} stretching mode provides support for this process since an increase in the N_{eq}-Mn-N_{eq} angle is consistent with relaxed c-directed Mn motion in the equatorial plane. The resulting decrease in the supplementary angle blue shifts the 224 cm^{-1} ν(Mn-N_{eq}) ab-plane displacement mode (Table 4.1). These combined effects of local structure deformations are invoked to accommodate the developing paramagnetic state imposed by external magnetic field.

Motivated by the discovery of the magnetoelastic coupling through the 30.4 T quantum critical transition, we sought to expose local lattice distortions through the 15.85 K paramagnetic $\rightarrow$ antiferromagnetic transition. [73,74] Our measurements reveal, however, only gradual frequency shifts over the temperature range of investigation with no anomalies at T_N (Fig. 4.5). This indicates that the development of long range antiferromagnetic order in $Mn(dca)_2$ takes place with no significant phonon anomalies (and no substantial lattice involvement). More broadly, it demonstrates that while spin-phonon/lattice mixing is inherently rather small in this material, the presence of a collective magnetic transition that switches the system between two

[10]Here, the tilt angle is defined as the the angle between the equatorial plane of the MnN_6 octahedron form the ac plane (Ref. [73]).

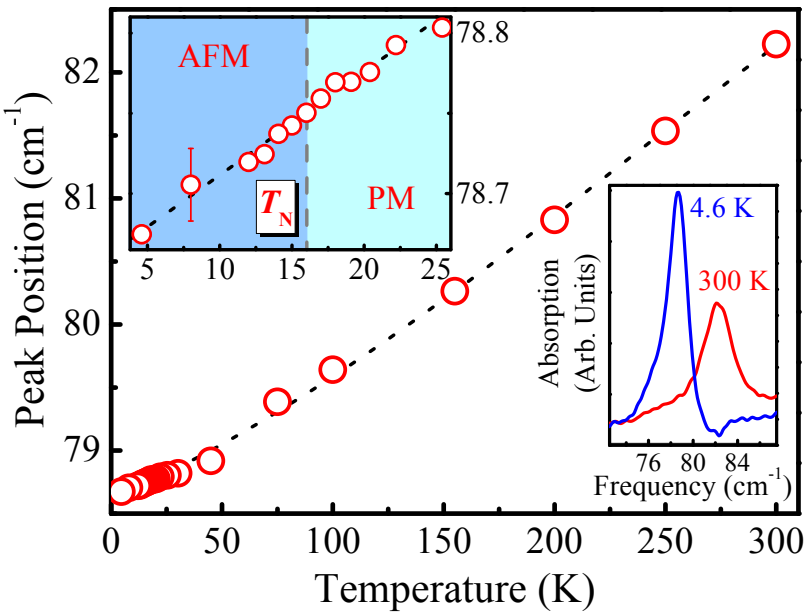

Figure 4.5: An example of the peak position vs. temperature for the low frequency Mn displacement mode in the full range of investigation. Upper inset: frequency change through the 15.85 K Néel transition. The trend is monotonic through T_N. The shaded regions visually separate the antiferromagnetic (AFM) and paramagnetic (PM) phases. Lower inset: absolute absorption of this lattice mode at low and high temperature. (Note: the asymmetric profile of this peak at low temperature is due to the presence of a weak structure hidden underneath the low frequency side of the main feature. It separates at higher temperature). The dotted line guides the eye.

different magnetic states with simultaneous, compulsory adjustment of the superexchange interactions can strongly amplify the effect. This finding is reinforced by our high field data on the isostructural paramagnet $Cu(dca)_2$ and suggests that collective transitions (like a quantum critical or spin flop transition) can be used to control the interplay between charge, structure, and magnetism. [210]

Chapter 5

Electron-Phonon and Magnetoelastic Interactions in Ferromagnetic $Co(dca)_2$

Chapter 5 is an adaptation of the research article by T. V. Brinzari *et al.* "Electron-phonon and magnetoelastic interactions in ferromagnetic $Co[N(CN)_2]_2$", Ref. [211]. To be submitted to an *ACS* journal. Authors' contributions are described in Chapter 3.

Herein, we report the vibrational response of $Co(dca)_2$ under two different external stimuli, magnetic field and temperature, and compare our findings to complementary dynamics calculations and magnetization measurements. Our work reveals a large anisotropy and rich charge-lattice-spin coupling including (i) an avoided crossing between a field-dependent Co^{2+} crystal field excitation and low frequency wagging phonons that we discuss in terms of electron-phonon interactions and (ii) magnetoelastic effects in which the local Co^{2+} environment distorts and the C≡N environment relaxes in response to applied field. These findings broaden our under-

standing of coupling phenomena under extreme conditions and demonstrate rich new aspects of multifunctionality in tunable molecular materials.

5.1 Large Magnetic Anisotropy in $Co(dca)_2$

Figure 5.1 (a) displays the characteristic magnetic hysteresis loop of $Co(dca)_2$ below the 9 K ferromagnetic transition temperature. [69] Measurements in fields up to 60 T (Fig. 5.1(b, c, d)) reveal an initial rapid rise of the magnetization (in fields of a few Tesla) followed by a steady increase and approach to saturation. This behavior can be understood in terms of (i) conventional domain alignment processes followed by (ii) a field-induced quenching of the single-ion anisotropy and (iii) a subsequent increase of the spontaneous magnetization. [104] We can extract the anisotropy by fitting the magnetization below 10 T with a Hamiltonian of the form:

$$\mathcal{H} = -\frac{1}{2}\sum_{i\neq j} J_{ij}\mathbf{S}_i \cdot \mathbf{S}_j - D\sum_i \mathbf{S}_{iz}^2 - g\mu_B B\sum_i \mathbf{S}_{iz}, \tag{5.1}$$

where $J \simeq 4$ K is the exchange interaction, [79] D is the anisotropy energy, g is the electron g-factor, $\mathbf{S}_i$ is the local moment on site i, and B is the external magnetic field.[1] We find $D = 12 \pm 4$ cm^{-1}, a direct consequence of the large Co^{2+} spin-orbit coupling and crystal-field effects. For an octahedrally coordinated Co^{2+} center, the ground state level is $^4T_{1g}$ ($L = 1$ is only partially quenched). Tetragonal distortion combined with spin-orbit coupling acts to split the $^4T_{1g}$ term, producing a manifold of six Kramers doublets (Fig. 5.2). The two lowest doublets are Γ_6 ($M_{S'} = \pm 1/2$) and Γ_7 ($M_{S'} = \pm 3/2$). [78, 212] Previous work demonstrates that only the lowest energy doublet (Γ_6) is populated at base temperature. [79, 80] At 4 K, $Co(dca)_2$ is therefore an effective $S' = 1/2$ system, [79] and a strong magnetic field aligns the

[1] More details on calculations are provided in Appendix B.

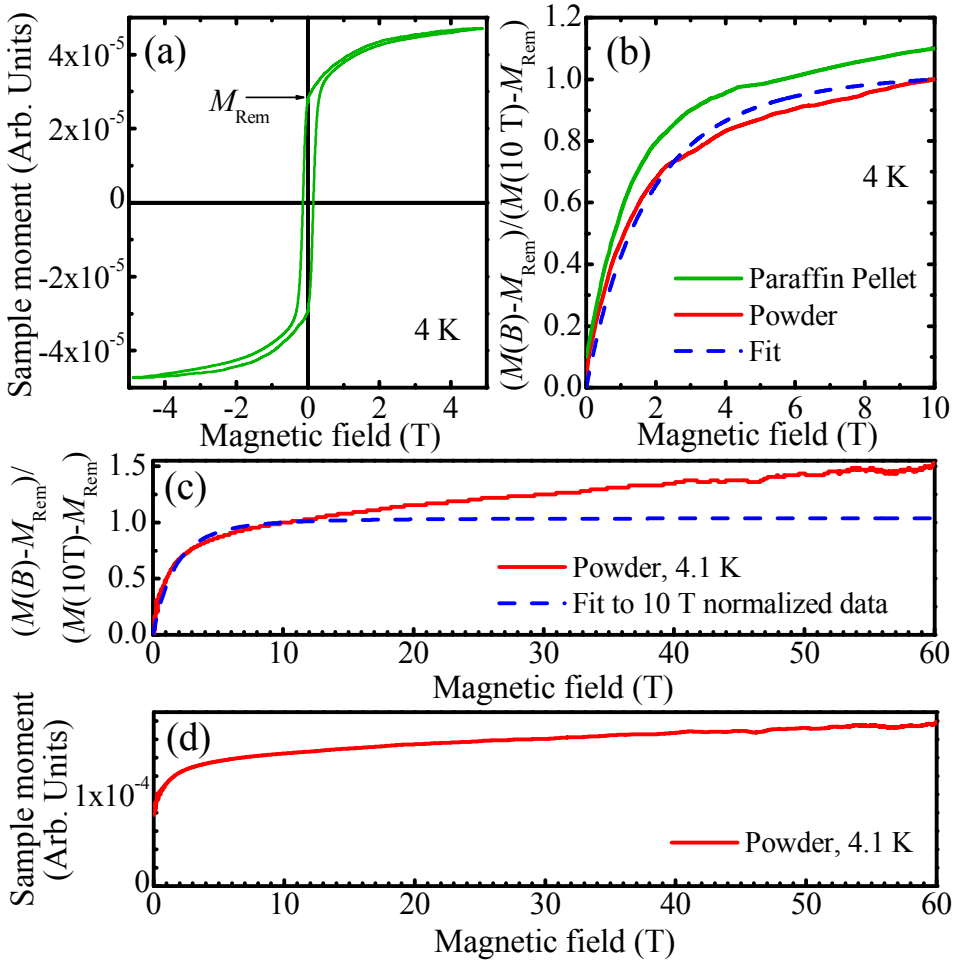

Figure 5.1: (a) Magnetic hysteresis loop of $Co(dca)_2$ in paraffin measured below the 9 K ferromagnetic transition temperature. (b) Normalized magnetization for polycrystalline $Co(dca)_2$ along with a theoretical fit up to 10 T. Also shown is the magnetization of sample mixed with a paraffin matrix. Identical behavior is observed. The paraffin pellet data is offset for clarity. (c) Normalized magnetization of a powder sample along with our model fit up to 60 T displaying a quasi-linear slope after $\simeq$10 T that rises above the $S = 1/2$ magnetization threshold. (d) Absolute magnetization of polycrystalline $Co(dca)_2$ in fields up to 60 T.

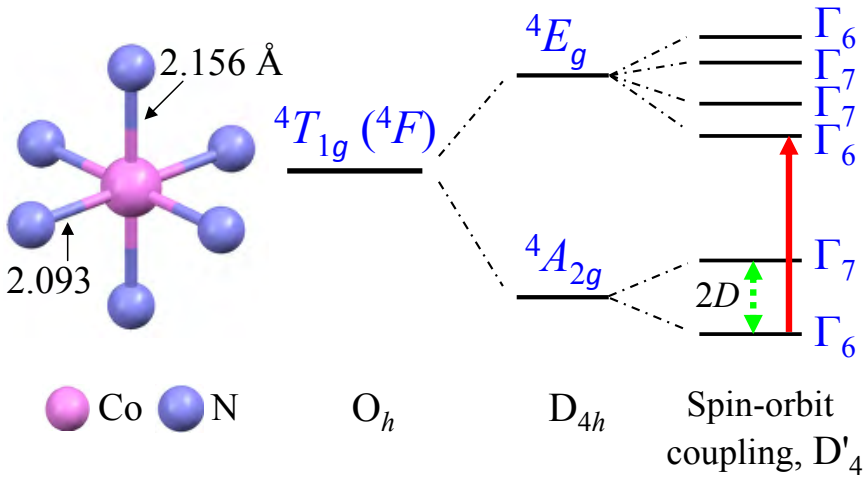

Figure 5.2: Local geometry around the cobalt magnetic center at 1.6 K [79, 80] along with a schematic energy level diagram for the electronic states of the Co^{2+} ion. The $^4T_{1g}$ state of the ^4F free ion term in the octahedral environment is split by a tetragonal distortion (D_{4h}) and spin orbit coupling (D'_4 double group) into six Kramers doublets. The degeneracy will be further removed by exchange and/or external magnetic field. The latter is the Zeeman effect. Here, $2D$ is indicated by the green (dashed) arrow, where D is the anisotropy (12±4 cm^{-1}) extracted from our magnetization measurements. The red (solid) arrow shows a plausible candidate for the 114 cm^{-1} excitation in the Raman spectrum of $Co(dca)_2$.

spins by slowly overcoming the anisotropy. Magnetization continues to increase at higher fields due to partial population of the higher energy $M_{S'} = -3/2$ branch of the Kramers doublet. To further investigate the magnetic properties of $Co(dca)_2$, we employed these parameters (J, D, S') along with $g = 5.34$ (Ref. [80]) to calculate the magnon energy of $Co(dca)_2$. Using a mean-field approximation, we find a zone center one-magnon energy of 12±4 cm^{-1} and predict its slope to be ≃2.5 cm^{-1}/T. Since $\omega_{Mag} = 16JS'(1 - \cos(k_a a/2)) + 2DS' + B$, $\omega_{Mag} = D$ when $S' = 1/2$, $k_a = 0$ and $B = 0$. [213] Here k is the wavevector, a is a lattice constant, and all other parameters are as defined above.

5.2 High Field Spectroscopic Probe of Competing Interactions

Magneto-vibrational spectroscopies are sensitive, microscopic techniques, well-suited to revealing charge-lattice-spin interactions and local lattice distortions. Common signatures include the appearance (or disappearance) of new features, mode splitting, frequency shifts, and changes in linewidth or integrated intensity. [56,62,125,155,214] A factor group analysis for the *Pnnm* space group yields 30 Raman active vibrations $\Gamma_R = 8A_g + 8B_{1g} + 7B_{2g} + 7B_{3g}$ and 25 infrared active modes $\Gamma_{IR} = 7B_{1u} + 9B_{2u} + 9B_{3u}$. [167] Below, we discuss coupling over several degrees of freedom in $Co(dca)_2$ as measured by Raman and infrared vibrational spectroscopies. We assign the observed features in $Co(dca)_2$ using mode frequencies, symmetries, and displacement patterns for the isostructural $Mn(dca)_2$ analog (Chapter 4).

5.2.1 Magneto-Raman signatures of electron-phonon coupling

Figure 5.3(a) displays the magneto-Raman spectrum of $Co(dca)_2$ in the low frequency range[2]. We assign the peaks near 147 and 158 cm^{-1} as phonons with Co-$N_{ax}C_{(2)}$ and Co-$N_{eq(2)}$ wagging motion, respectively (Table 5.1). Figure 5.3(b) summarizes the frequency vs. field trends of these phonons along with the behavior of a strongly field-dependent feature that we assign (below) as a Co^{2+} crystal field excitation. Taken together, these data reveal a dramatic avoided crossing. The sequence of events can be summarized as follows. At low fields, the phonons harden systematically, with 0.6 and 0.3 cm^{-1} frequency shifts at 14 T, respectively. Then a new feature appears

[2]Here, we only focus our discussion on two strong features near 147 and 158 cm^{-1} which display the most intriguing findings. The Raman shift frequency was calibrated using the reference spectrum of the elemental sulfur.

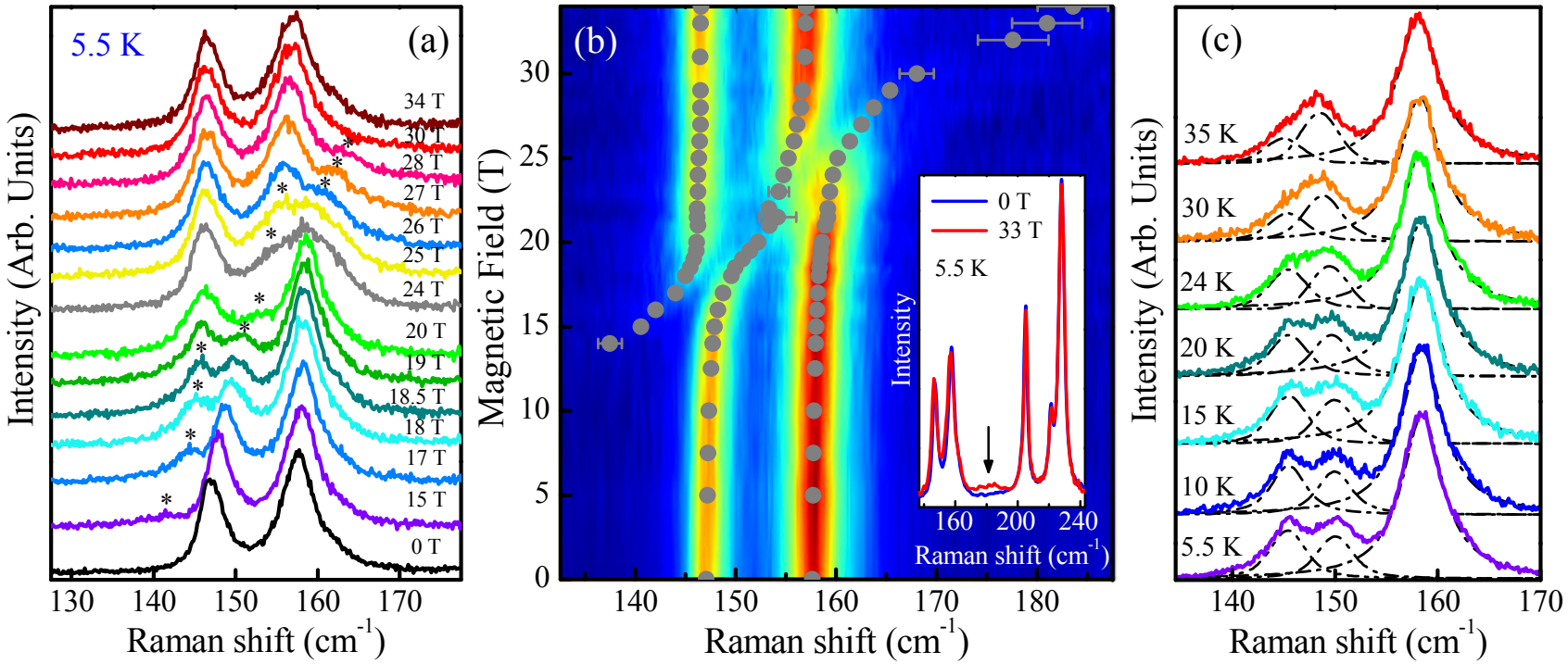

Figure 5.3: (a) Representative magneto-Raman spectra of $Co(dca)_2$ in fields up to 34 T. The strongly field dependent feature that we assign as a Co^{2+} electronic excitation is marked with an asterisk, and the data are offset for clarity. (b) Contour plot of peak intensities as a function of frequency and magnetic field: blue - low intensity, red - high intensity. Dark gray points represent positions extracted by peak fitting technique. Error bars are on the order of symbol size or as indicated. The inset shows an expanded view of the low temperature Raman spectrum along with the development of the broad structure as it approaches the next set of phonons. (c) Temperature dependence of the magneto-Raman spectrum at 18.6±0.1 T along with peak fits tracking the behavior of the Co^{2+} electronic excitation.

Table 5.1: Assignment of selected vibrational peaks for $Co(dca)_2$ along with their magnitude of change in a 35 T magnetic field at low temperature. (R - Raman-active, IR - Infrared-active)

Frequency, (cm^{-1})	Symmetry	Vibrational mode assignment	$\lvert\Delta\alpha\rvert/\alpha$	Behavior with increasing field
147^R	B_{1g}	Co-$N_{ax}C_{(2)}$ wagging type (modulates N_{ax}-Co-N_{eq} angle)		avoided crossing, softening at 35 T ($\simeq$0.5 cm^{-1})
158^R	B_{2g}	Co-$N_{eq(2)}$ wagging (alternatively N_{eq}-Co-N_{eq} rocking)		
289^{IR}	B_{2u}	$\sim \nu$(Co-N_{ax}) + $\sim \nu$(Co-N_{eq}) with ligand component	6 %	harden, non-linear
317^{IR}	$B_{1u}/B_{2u}/B_{3u}$	ligand bands, mostly N motion: scissors, twisting, wagging, rocking	4 %	soften, non-linear
995^{IR}	-	(NCN) bend, combination (IR + Raman)	2 %	harden, $\sim$linear
1320^{IR}	B_{1u}	ν_{as} (N-C), in phase N motion along c axis	1 %	soften, non-linear
2294^{IR}	B_{2u}	ν_s (C$\equiv$N)	6 %	soften, $\sim$linear

in the spectrum. Initially, this structure has very weak intensity but becomes more pronounced as it shifts toward higher frequency and interacts with the phonons. A closer look at intensity and/or integrated area trends clearly demonstrates that this developing feature gains intensity by stealing it from the 147 and 158 cm^{-1} phonons. In other words, growth occurs at the expense of the phonons while maintaining approximately constant total oscillator strength. This behavior indicates that mixing is required to activate or amplify the strongly field-dependent structure. Near 18.5 T, intensity is shared between the 147 cm^{-1} phonon and the new feature, and clear peak repulsion is observed. [215] Once the field-dependent structure moves out of range, the 147 cm^{-1} phonon recovers its strength and red shifts from its zero-field position (Table 5.1). With increasing field, we find a heavily mixed phase with a temporary intensity loss and subsequent recovery of the field-dependent structure as it approaches the 158 cm^{-1} phonon. Mixing and crossing with the second phonon is similar to that of the first, with the maximum interaction taking place near 25 T. At higher field, the intensity of the hybrid Co^{2+} crystal field excitation diminishes, becoming very difficult to track above 30 T.[3] It is likely that at even larger fields this structure reappears and interacts with the next available phonon at $\simeq$205 cm^{-1}. A small feature is indeed seen in our high field spectrum near 180 cm^{-1} (inset, Fig. 5.3(b)), but the weak intensity precludes further discussion.

It is of great interest to understand the nature of the structure that appears near 14 T, gains strength as it passes through the phonons, and diminishes again at higher field. We begin by establishing a few facts. Based upon the observation that no other phonons in our investigated frequency and field range experience similar behavior, we attribute intensity enhancement and avoided crossing to the energetic

[3]It is possible that there is another hidden feature near 162 cm^{-1} that may also interact with field-dependent structure, however its weak intensity makes any further analysis and conclusion highly uncertain.

proximity of the field-dependent structure to the 147 and 158 cm^{-1} phonons. Moreover, the field-induced blue shift of this structure is exceptionally large as compared to the behavior of known phonons in $Co(dca)_2$. From the frequency vs. field data (Fig. 5.3(b)), we extract a slope $d\omega^*/dB$ of $\simeq$1.8 cm^{-1}/T, where ω^* represents the frequency of the field-dependent structure. Extrapolating this trend to zero field, we estimate an unperturbed resonance frequency of 114$\pm$5 cm^{-1}. These magneto-Raman measurements do not, however, reveal a fundamental excitation in this range implying that either (i) the initial peak intensity is extremely weak or (ii) the fundamental excitation is Raman inactive and is activated only through coupling with nearby phonons.

The strikingly strong and quasi-linear dependence of ω^* on magnetic field resembles the Zeeman effect and suggests that the new structure originates from either an electronic or magnetic excitation involving the Co^{2+} center. Energetic considerations combined with temperature studies, however, rule out scenarios involving a field-dependent magnon, multi-magnon, or coupled magnon-phonon excitation (see Appendix B). We therefore assign this structure as a Co^{2+} electronic excitation from the ground state Γ_6 level to the one of the higher lying doublets of the $^4T_{1g}$ term that moves with field as the Zeeman effect comes into play.[4] Such a candidate excitation is shown in Fig. 5.2. Co^{2+} electronic excitations within the $^4T_{1g}$ term have been studied in the past, for example in $CsCoCl_3$ and $CoBr_2$ [60, 62] revealing, for instance, similar crystal field and phonon intensities, field-induced splitting, and energy shifts of about 2.4 cm^{-1}/T in $CsCoCl_3$. In $Co(dca)_2$, unpublished neutron data [216] are also consistent with the presence of a low energy electronic excitation

[4]One can estimate the energy shift in magnetic field as $\delta E = g\mu_B M_{S'} B B_r(x)$ where $B_r(x)$ is the Brillouin function [165] with $x = \frac{g\mu_B B S'}{k_B T}$, and k_B and T are Boltzmann constant and temperature, respectively. For example, for the ground level Γ_6 ($M_{S'} = \pm 1/2$) δE = 42 cm^{-1} at B = 34 T (g = 5.34). The rest of the contribution to the excitation energy shift comes from the splitting of the higher energy levels.

Table 5.2: Symmetry analysis for the Co^{2+} electronic excitations between sublevels of the ${}^4T_{1g}$ ground state of the octahedral environment

Direct product	$D_4{}'$ site symmetry	D_{2h} crystal symmetry
$\Gamma_6 \otimes \Gamma_6$	$\Gamma_1(A_1') \oplus \Gamma_2(A_2') \oplus \Gamma_5(E_1')$	$A_g \oplus B_{1g} \oplus B_{2g} \oplus B_{3g}$
$\Gamma_6 \otimes \Gamma_7$	$\Gamma_3(B_1') \oplus \Gamma_4(B_2') \oplus \Gamma_5(E_1')$	$A_g \oplus B_{1g} \oplus B_{2g} \oplus B_{3g}$
$\Gamma_7 \otimes \Gamma_7$	$\Gamma_1(A_1') \oplus \Gamma_2(A_2') \oplus \Gamma_5(E_1')$	$A_g \oplus B_{1g} \oplus B_{2g} \oplus B_{3g}$

Raman tensor D_{2h} symmetry: $A_g + B_{1g} + B_{2g} + B_{3g}$

between 80 and 120 cm^{-1}. Based on general symmetry considerations, [166] $\Gamma_6 \rightarrow \Gamma_6$ and $\Gamma_6 \rightarrow \Gamma_7$ type excitations are Raman active in all polarizations (Table 5.2 and Appendix B), although in $Co(dca)_2$, the intensity is weak at zero field. As ω^* approaches the phonon energies, however, interaction takes place, and the electronic excitation gains intensity by mixing with the phonons.

We can estimate the electron-phonon interaction energy in $Co(dca)_2$ by fitting the energy vs. field behavior using a model of two coupled oscillators. [61, 215] The general Hamiltonian that describes such a coupled system can be written as:

$$\mathcal{H} = \begin{bmatrix} \omega_{ph} & \lambda' \\ \lambda' & \omega^* \end{bmatrix}, \tag{5.2}$$

where ω_{ph} and ω^* are the phonon and Co^{2+} electronic excitation frequencies, and λ' is the coupling constant. The perturbed energy levels are given as:

$$\omega_{1,2} = \frac{\omega_{ph} + \omega^*}{2} \pm \sqrt{\left(\frac{\omega_{ph} - \omega^*}{2}\right)^2 + \lambda'^2}. \tag{5.3}$$

Taking into account the field dependence of the electronic excitation, best fit to magneto-Raman data (Fig. 5.4) is achieved with the coupling constants of 2 and

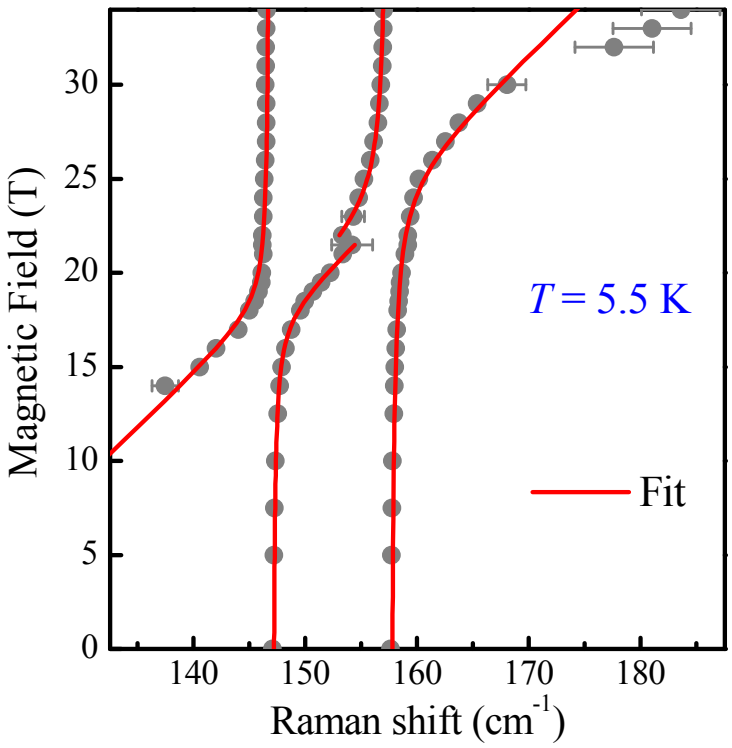

Figure 5.4: Peak position vs. field behavior for the hybridized electronic and phonon excitations in $Co(dca)_2$ probed by magneto-Raman spectroscopy. Red curves are fit to the data using Eq. [5.3].

3 cm^{-1} for the 147 and 158 cm^{-1} phonons, respectively.[5] By comparison, electron-phonon coupling manifests itself in $CoBr_2$ and $FeCl_2$ [62, 214] with mixed oscillator strengths and/or linewidths and coupling constants on the order of 8 cm^{-1}. Finally, the temperature dependence of the magneto-Raman response is in line with our assignment of the 114 cm^{-1} feature as an electronic excitation. Measurements at 18.6 T reveal that this structure persists up to at least 35-40 K and displays no sensitivity to the 9 K Curie temperature (Fig. 5.3(c) and Appendix B), findings that exclude mechanistic scenarios involving magnons.[6] The suppressed intensity of the 114 cm^{-1} electronic excitation at high temperature likely results from thermal broadening effects and a decreased population of the ground state level as the zero-field splitting is slowly overcome (Fig. 5.2). [61, 62, 214, 217]

5.2.2 Infrared properties and magnetoelastic interactions

To investigate the interplay between structure and magnetism, we also measured the magneto-infrared response of $Co(dca)_2$. As a reminder, the magneto-infrared effects that we discuss below involve vibrational modes of ungerade symmetry, distinct from (but complementary to) gerade mode behavior probed in Raman scattering experiments. Figure 5.5(a) displays the far infrared absorption spectrum at $B = 0$ T along with the absorption difference spectrum at full field $\Delta\alpha = \alpha(35\text{ T}) - \alpha(0\text{ T})$.[7] The latter emphasizes field-induced changes in the vibrational response, a rendering that makes it easy to see that modes near 289 and 317 cm^{-1} harden and soften, respectively, with field.[8] Over the full frequency range of our investigation (30-3500 cm^{-1}), we find a total of five structures that develop systematically with applied

[5] We assume individual/separate coupling to each of the phonons.

[6] The second independent sample measured up to 40 K displays analogous behavior with clear signatures of field-dependent feature even at 40 K.

[7] The complete infrared spectrum is provided in the Appendix B.

[8] Our analysis indicates that the observed changes in the absorption difference originate mainly from frequency shifts as compared to intensity or linewidth variations (Appendix B).

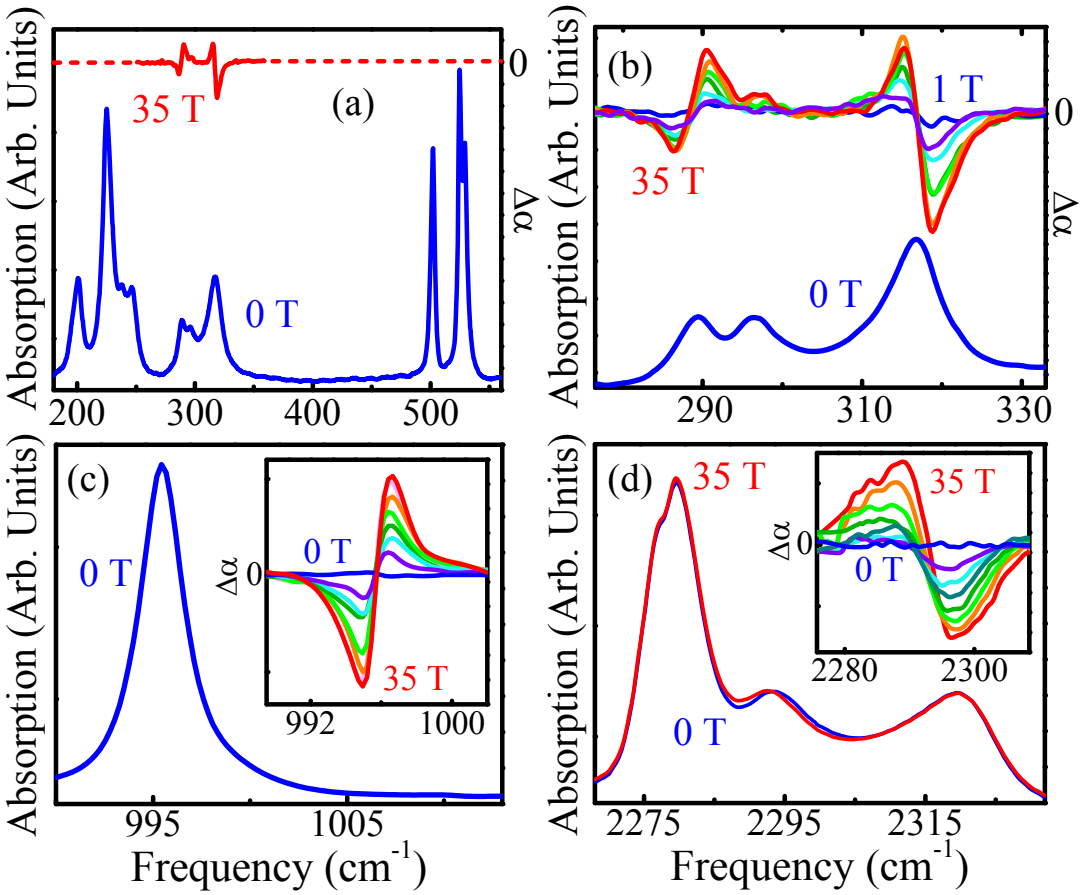

Figure 5.5: (a) Far infrared absorption spectrum of $Co(dca)_2$ along with the full field absorption difference, $\Delta\alpha = \alpha(35\text{ T}) - \alpha(0\text{ T})$. (b, c, d) Close-up views of selected modes at $B = 0$ and/or 35 T along with their absorption differences. For (b), $B =$ 1, 3, 5, 10, 15, 25, 35 T. For the insets of (c) and (d), $B = 0$, 5, 10, 15, 20, 25, 30, 35 T. All spectra were collected at liquid helium temperature.

field. Panels (b), (c), and (d) show close-up views of these trends, and Table 5.1 summarizes our symmetry and mode assignments along with the size of the field-induced changes (as measured by $|\Delta\alpha|/\alpha$).

We quantify changes in the magneto-infrared response by integrating the absolute value of the absorption difference spectrum as $\int_{\omega_1}^{\omega_2} |\alpha(B) - \alpha(0\ \mathrm{T})|\, \mathrm{d}\omega$ and plotting these values with the normalized magnetization (Fig. 5.6). Two distinct trends are immediately apparent. The integrated absorption differences for phonons at 289, 317 and 1320 cm^{-1} rise with the magnetization, whereas data related to the 995 and 2294 cm^{-1} peaks increase quasi-linearly with magnetic field - a trend that is strikingly different from that of the other modes as well as the magnetization. These differences indicate the importance of the mode motion and the nature of the displacement pattern to the field-induced local lattice distortion. One correlation involves mostly dominant nitrogen motion for the Co-$N_{ax/eq}$ stretch at 289 cm^{-1}, the ligand band at 317 cm^{-1}, and the asymmetric N-C stretch at 1320 cm^{-1} vs. dominant carbon motion for the NCN bending combination and C≡N stretch at 995 and 2294 cm^{-1}, respectively. An additional correlation involves proximity to the Co^{2+} magnetic center, which may be responsible for the displacement pattern-dependent rapidly rising (fast) vs. quasi-linear (slow) response of these modes to applied field. This bifurcated behavior is quite different from $Mn(dca)_2$, where all field-dependent vibrational modes display a similar response to the magnetic quantum critical transition at 30 T and map cleanly onto the square of the magnetization (Chapter 4), a finding that illustrates how the manifestation and origin of the magnetoelastic phenomena depend upon the distinct magnetic and electronic ground state.[9]

To expose the field-induced local lattice distortion in $Co(dca)_2$, we evaluated changes in phonon behavior as $|\Delta\alpha|/\alpha = |\alpha(35\ \mathrm{T}) - \alpha(0\ \mathrm{T})|/\alpha(0\ \mathrm{T})$ (Table 5.1).

[9] $Co(dca)_2$ is also different from quantum magnets like $Cu(pyz)(NO_3)_2$ and $Cu(pyz)_2(HF_2)BF_4$ where both out-of-plane pyrazine distortion modes track the magnetization. [54, 156]

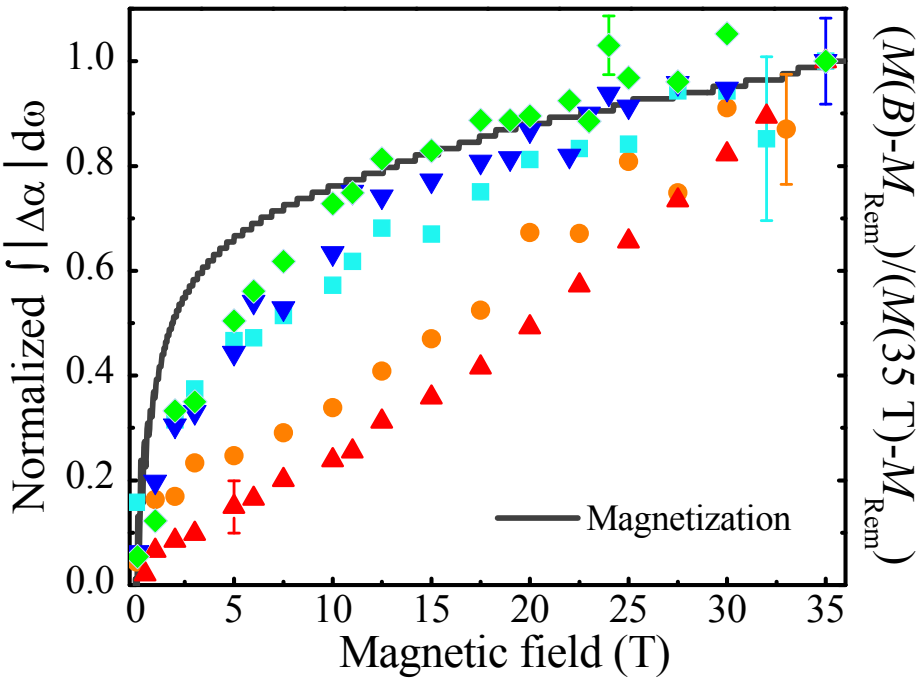

Figure 5.6: Integrated absolute absorption difference as a function of applied field compared with the magnetization. This data has been normalized at 35 T for display purposes. The field-dependent vibrational features show either linear or non-linear growth with field depending on mode character. ▼ - 289 cm^{-1} peak, ♦ - 317 cm^{-1}, ● - 995 cm^{-1}, ■ - 1320 cm^{-1} and ▲ - 2294 cm^{-1} peak. All spectra were collected at liquid helium temperature. Absolute error bars are indicated; relative error bars are smaller.

The later allows us to focus on the most prominent changes and reveal the leading local structure deformations. Our analysis uncovers two infrared-active modes at 289 (the Co-$N_{ax/eq}$ stretch) and 2294 cm^{-1} (the C≡N stretch) with ∼6% changes between 0 and 35 T. In a simple scenario, that involves only these leading modes and considers simple bond length-frequency correlation, the observed hardening of 289 cm^{-1} phonon is indicative of a slightly axially compressed CoN_6 octahedron at high magnetic fields, a situation that is similar to that in $Co_3V_2O_8$. [154] Simultaneous softening of the 2294 cm^{-1} mode indicates a more relaxed ligand environment that likely accommodates the need for distortion around the magnetic center.[10] This general picture of a squashed CoN_6 octahedron environment enabled by flexible ligands is in line with our Raman spectra that show overall softer ligand vibrations in high magnetic field (Table 5.1).

These field-induced local lattice deformations have a counterpart in magnetostriction, an interaction that is well known to occur in ferromagnetic materials. [104,106] Domain alignment and the form effect usually dominate the magnetostriction at low fields (< few Tesla). They are further accompanied by field-induced lattice distortions as magnetization reorients toward the field direction which perturbs the crystal field due to the non-zero spin-orbit coupling. In addition, exchange or volume magnetostriction arises from the dependence of the exchange interaction on interatomic distances. Magnetostriction is, of course, a bulk technique that quantifies changes in unit cell parameters, whereas our work focuses on the magnetoelastic processes that reveal local lattice deformations.

Bringing these findings together exposes several common themes. For instance, Nuttall *et al.* show that pressure drives a ferromagnetic → antiferromagnetic transition in $Co(dca)_2$ - a consequence of the soft lattice and the sensitivity of exchange

[10]The high lability of (C≡N) π-bonding can be responsible for the sensitivity of the C≡N stretching mode to applied field.

interactions to small pressure-induced changes in magnetic orbital overlap. [72] At the same time, neutron diffraction measurements by Lappas *et al.* reveal only subtle changes in unit cell parameters through the 9 K paramagnetic $\rightarrow$ ferromagnetic transition, [75] in line with our variable temperature investigations of phonon behavior that show only gradual changes in the lattice through T_C (Appendix B). These findings clearly illustrate the advantages of magnetic field and pressure as physical tuning parameters for probing magneto-structural correlations in $Co(dca)_2$, insights that can be useful in the design and control of other functional materials.

Chapter 6

Flexible $[Cr(CN)_6]^{3-}$ Octahedron in $[Ru_2(O_2CMe)_4]_3[Cr(CN)_6]$: a Spectroscopic Probe

Chapter 6 is an adaptation of the research article by T. V. Brinzari *et al.* "Magnetoelastic coupling in $[Ru_2(O_2CMe)_4]_3[Cr(CN)_6]$ molecule-based magnet", Ref. [218]. Accepted, *Physical Review B*. Copyright (2012) by the American Physical Society. Authors' contributions are described in Chapter 3.

In this work, we employed infrared and Raman vibrational spectroscopies to explore the lattice dynamics of $[Ru_2(O_2CMe)_4]_3[Cr(CN)_6]$ through the field- and temperature-driven magnetic transitions. The high field work reveals a magnetoelastic component manifested by systematic changes in the C≡N stretching mode and Cr^{3+}-containing phonons as the system is driven away from the antiferromagnetic state. The magnetic intersublattice coalescence transition at $B_c \simeq 0.08$ T, on the contrary, is purely magnetic and takes place with no lattice involvement. Our variable temperature spectroscopy affirms $[Cr(CN)_6]^{3-}$ building block flexibility along with

strengthened intermolecular interactions at low temperature. Based on a displacement pattern analysis, we discuss the local lattice distortions in terms of an adaptable chromium environment and rigid ruthenium dimers. Taken together, these findings reveal the key local lattice distortions that underpin the magnetoelastic properties of this system at high magnetic fields. More generally, our findings may provide insight into behavior of other Cr-containing materials, like Prussian blue analogs and oxides.

6.1 Lattice Dynamics Through the Metamagnetic Transition and Towards the High Field State

The 4.2 K far infrared absorption spectrum of $[Ru_2(O_2CMe)_4]_3[Cr(CN)_6]$ in zero field is shown in Fig. 6.1(a) along with the full field absorption difference $\Delta\alpha = \alpha(B = 35\ \text{T}) - \alpha(0\ \text{T})$. The latter clearly demonstrates the sensitivity of certain modes to magnetic field and the rigidity of others. Figure 6.1(b) illustrates the systematic development of features near 370 and 460 cm^{-1}. Investigation of the higher frequency response (up to 3200 cm^{-1}) reveals only one additional feature near 2145 cm^{-1} that is susceptible to external field (Fig. 6.1(c)). All other infrared-active phonons remain rigid. We interpret these findings in terms of field-induced local lattice distortions.[1]

To transform our experimental findings into a higher-level understanding of local structural deformations, we turn to an assignment of the observed peaks. Group theory predicts $4F_{1u}$ infrared-active vibrations for a $[Cr(CN)_6]^{3-}$ block of an ideal octahedral environment. Previous studies of $[M(CN)_6]^{n-}$-based compounds identified these frequencies as 90-160, 340-350, $\simeq$460 and 2120-2130 cm^{-1}. [219–223] Bringing these literature data together with our independent measurements of model compounds like $K_3[Cr(CN_6]$, we assign the $[Ru_2(O_2CMe)_4]_3[Cr(CN)_6]$ bands near 120,

[1]We attribute the observed phonon response to magnetic field as due to local lattice distortions rather than to dynamic spin-phonon coupling effects.

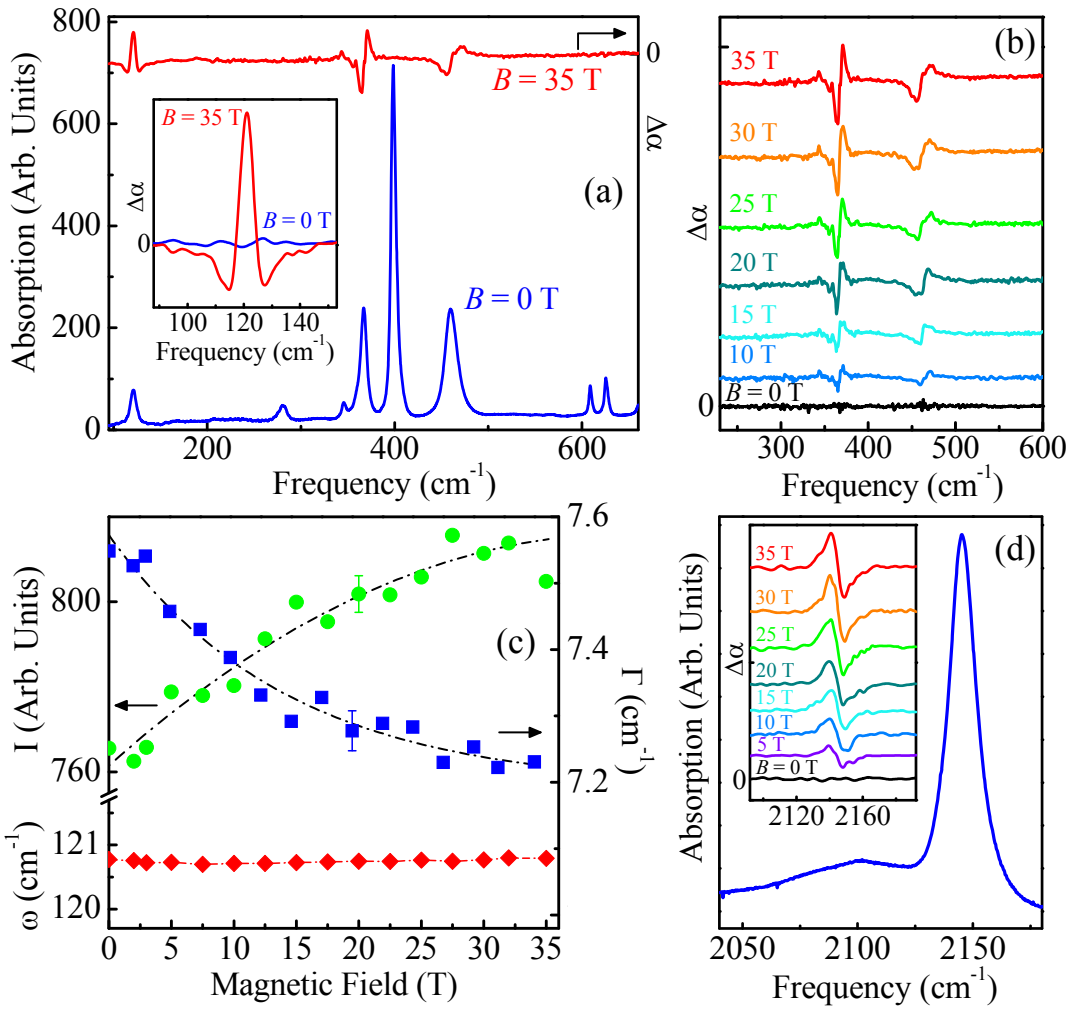

Figure 6.1: (a) Far infrared absorption spectrum of $[Ru_2(O_2CMe)_4]_3[Cr(CN)_6]$ along with the full field absorption difference spectrum $\Delta\alpha = \alpha(B = 35\text{ T}) - \alpha(0\text{ T})$. Inset: Close-up view of $\Delta\alpha$ at $B = 0$ and 35 T for the $\simeq$120 cm^{-1} phonon emphasizing its different shape as compared to the other features. The $B = 0$ T curve demonstrates the sensitivity level of $\Delta\alpha$ calculated using scans before and after the field sweep. (b) $\Delta\alpha$ of the 370 and 460 cm^{-1} modes at representative fields highlighting their vibrational contrast. Data are offset for clarity from the $B = 0$ T curve. (c) Intensity (I), frequency (ω), and linewidth (full width at half maximum, Γ) as a function of field for the δ(C-Cr-C) bend near 120 cm^{-1}. (d) Absorption profile of the ν(C$\equiv$N) stretch at 2145 cm^{-1} along with the corresponding field-induced changes in $\Delta\alpha$ (inset). Data are offset for clarity. All data were measured at liquid helium temperature.

370, 460, 2145 cm^{-1} to the δ(C-Cr-C) bend, ν(Cr-C) stretch, δ(Cr-C-N) bend, and ν(C$\equiv$N) stretch, respectively.[2] The strong peak at $\simeq$400 cm^{-1} is assigned as a ν(Ru-O) stretch. [224] Its second component is expected near 340 cm^{-1} (which overlaps with the ν(Cr-C) band) and probably corresponds to the weak feature near 345 cm^{-1}.[3] [224] This assignment agrees with frequency and intensity variations in independently measured metal-substituted $[Ru_2(O_2CMe)_4]_3[M^{III}(CN)_6]$ (M = Fe, Co) and also the $[Ru_2(O_2CMe)_4]Cl$ parent compound.[4]

Combining mode assignment and displacement pattern information with our magneto-infrared spectra, it is apparent that applied field dominantly affects the octahedral $[Cr(CN)_6]^{3-}$ centers (as evidenced by the sensitivity of the 120, 370, 460 and 2145 cm^{-1} peaks) and barely perturbs modes emanating from the $[Ru_2(O_2CMe)_4]^+$ paddle wheel complex. Interestingly though, the nature of the response is not the same for each mode. Close-up views of the absorption difference spectra (Fig. 6.1(a, b, c)) clearly illustrate the unique features. The 120 cm^{-1} mode is characterized by a sharp peak centered between two minima whereas the 370, 460 and 2145 cm^{-1} features have derivative-like structures. The former lineshape is characteristic of field-induced width and intensity changes, whereas the derivative-like lineshape points to field-induced frequency shifts (with both red and blue shifts observed in $[Ru_2(O_2CMe)_4]_3[Cr(CN)_6]$.

In general, peak position, linewidth, and intensity trends can serve as indicators of phase transitions and their mechanisms. [56, 112, 125, 148, 227] Trends in these

[2]Cr-C stretch and Cr-C-N bend are considered to be mixed with each other and present to some degree in each vibration.

[3]This peak displays very weak temperature dependence (<1 cm^{-1}) and no field dependence within our error bars, a behavior that is quite similar to the 400 cm^{-1} feature, thus providing an additional support for its assignment.

[4]At this moment location of the ν(Ru-N) stretch is uncertain. Feature near 280 cm^{-1} likely corresponds to one of the expected (RuO) deformation bands of weak intensity, while peaks near 620 and higher energy 690 cm^{-1} are assigned to ρ(COO) rocking and δ(COO) bend, respectively. Very weak excitation near 945 cm^{-1} corresponds to ν(C-C) stretch. [224–226]

quantities are particularly useful for revealing magnetoelastic interactions through field-driven transitions. [54, 148, 154, 156] As an example, Fig. 6.1(d) shows the gradually increasing intensity and the simultaneously decreasing linewidth of the 120 cm^{-1} phonon. The peak position remains constant, and total oscillator strength is approximately conserved. This behavior suggests a gradual field-induced reduction of the damping constant (Γ) for the δ(C-Cr-C) vibration. We find $|\Delta\Gamma|/\Gamma(0\ \mathrm{T}) = (\Gamma(35\ \mathrm{T}) - \Gamma(0\ \mathrm{T}))/\Gamma(0\ \mathrm{T}) \approx 4 \pm 0.5\%$.

To reveal the trends in the higher frequency phonons, we calculated the value of the integrated absolute absorption difference $\int_{\omega_1}^{\omega_2} |\alpha(B) - \alpha(0\ \mathrm{T})|\, \mathrm{d}\omega$ (where ω_1 and ω_2 define the frequency range of interest) and plotted these data as a function of magnetic field.[5] The low temperature magnetization ($M(B)$) and the square of the magnetization $(M(B))^2$ are included for comparison (Fig. 6.2). The magnetization data is characterized by a fast initial rise at low fields, a signature of the previously-reported metamagnetic transition, [51, 98] followed by a continuous rise at higher fields as the field slowly overtakes the system anisotropy and exchange interactions. On the other hand, there is no magneto-infrared contrast within our sensitivity through the intersublattice coalescence transition. The lack of change in the infrared pattern at $B_c \simeq 0.08$ T, the critical point where both sublattice moments become aligned, indicates little spin-lattice interaction and a rigid lattice through the magnetic coalescense. This finding may be useful for understanding magneto-structural correlations in other metamagnetic materials in that modeling efforts can focus on spin-only interactions. [52, 228, 229]

Above B_c, the field slowly cants spins away from AFM alignment in competition with the intrasublattice exchange interactions and ruthenium anisotropy. [96, 97] At the same time, there is clear evidence of magnetoelastic interactions in the form of

[5] Small frequency shifts sometimes are hard to track, so we use $\Delta\alpha$ as a more sensitive parameter. We carried out this analysis for all the phonons, including the 120 cm^{-1} feature for comparison.

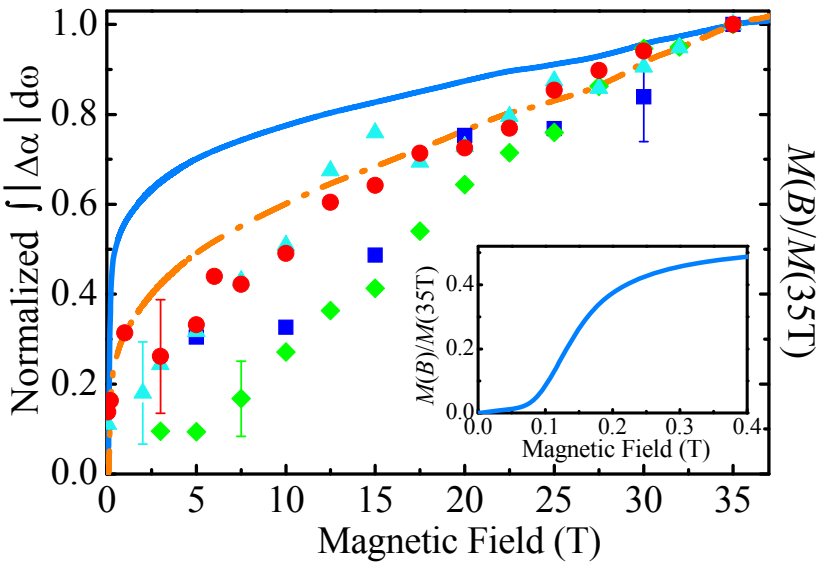

Figure 6.2: Integrated absolute absorption difference vs. applied field compared with the magnetization and the square of the magnetization. The data are normalized to 35 T. (▬) - 4 K magnetization ($M(B)$), (▬·▬) - $(M(B))^2$, ▲ - 120 cm^{-1}, ◆ - 370 cm^{-1}, ■ - 460 cm^{-1} and ● - 2145 cm^{-1} peaks. All magneto-infrared data were collected at 4.2 K. Inset: Close-up view of low field magnetization demonstrating the magnetic intersublattice coalescence transition at $B_c \simeq 0.08$ T. Magnetization measurements up to 60 T do not reveal any additional transitions.

field-dependent phonons (Fig. 6.2), and as in the case of $Mn[N(CN)_2]_2$ (Chapter 4), the magneto-infrared response seems to have a better match with $(M(B))^2$ rather than the magnetization itself. The latter signals the exchange nature of the observed magnetoelastic effect. [137] Using $|\Delta\alpha|/\alpha = |\alpha(35\text{ T}) - \alpha(0\text{ T})|/\alpha$ to quantify the size of the coupling for each type of displacement, we find that the most prominent change, on the order of 2-3% at 35 T, can be attributed to softening of the C≡N stretching mode. Slightly smaller changes are detected for the ν(Cr-C) stretch and the δ(Cr-C-N) bend with 1-2% and 1% changes, respectively. Both modes harden in field. The high magnetic energy scales in $[Ru_2(O_2CMe)_4]_3[Cr(CN)_6]$ allow us to probe only the onset of the spin-lattice interactions. More pronounced magnetoelastic effects are anticipated at higher fields.

The finding of flexible CrC_6 octahedra and soft C≡N linkages can be correlated

with the $[Ru_2(O_2CMe)_4]_3[Cr(CN)_6]$ structural arrangement (Fig. 2.6) where CN ligands bridge the Cr and Ru_2 magnetic centers thereby providing an effective superexchange pathway. [51] Our results reveal that when the applied field is large enough to compete with the AFM superexchange interactions (with energy scale J_c), the process is accompanied by magnetoelastic interactions in which the Cr environment and in particular the bridging CN units change to accommodate the developing magnetic state.[6] Similar cooperative effects occur in other materials. [54, 154, 230] From the direction of the field-induced blue shift of Cr-containing phonons and a simple "frequency-bond distance" correlation, [231,232] the high field local geometry likely consists of a compressed CrC_6 octahedron. There is no evidence for octahedral distortion within our sensitivity, so we conclude that the compression is isotropic, although this finding should be tested to even higher fields.[7] In case of the CN linkages, softening points to an overall more relaxed environment of this unit. The relationship to the bond length however, is more complex and an inverse correlation is indicated as discussed below.

To complement our high field work on ungerade symmetry vibrations, we investigated the magneto-Raman response of $[Ru_2(O_2CMe)_4]_3[Cr(CN)_6]$ with particular interest in the symmetric Ru-Ru and Ru-O modes. Our low temperature Raman spectrum reveals two strong lines near 320 and 360 cm^{-1} and a number of weaker, broader structures whose low intensity precludes detailed investigation. Here, we focus our discussion on two intense features near 320 and 360 cm^{-1} (Fig. 6.3). Based on previous literature data and the insensitivity of these lines to M^{III} (M = Cr, Co, Fe) substitution, we assign them as Ru-Ru and Ru-O stretching bands, respectively. [224] Application of a 35 T field reveals no changes in the behavior of these

[6] Anisotropy associated with crystal field effects is absent for Cr sites (^4A_g ground state).

[7] The weak structure on the left hand side of the 360 cm^{-1} peak in $\Delta\alpha$ is beyond our sensitivity. Higher magnetic fields (>35 T) may reveal its behavior and any signatures of octahedral distortion.

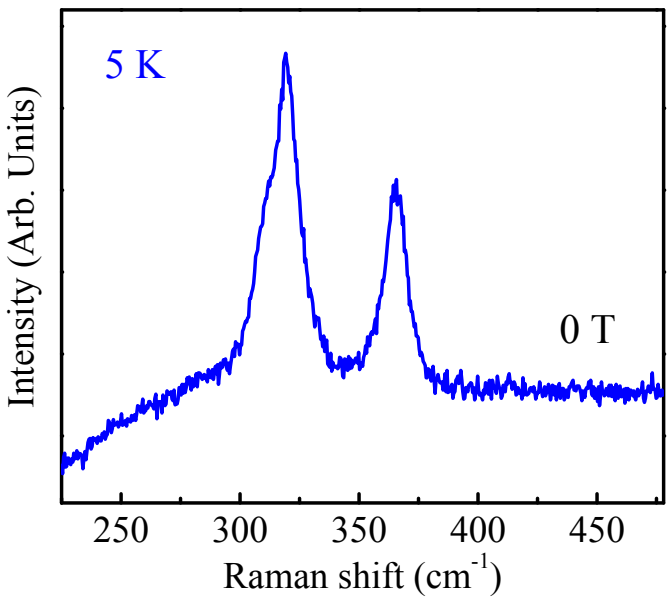

Figure 6.3: Low frequency Raman spectrum of $[Ru_2(O_2CMe)_4]_3[Cr(CN)_6]$ at zero field.

modes within our sensitivity, a finding that is consistent with the magneto-infrared result of a rigid $[Ru_2(O_2CMe)_4]^+$ cluster.

$[Cr(CN)_6]^{3-}$, and hexacyanometalates in general, are attractive and oft-used molecular building blocks. [7,8,233,234] The chemical diversity of polycyanide molecular precursors combined with the tunability of their magnetic properties through flexible M-CN-M linkages led to materials with room temperature and photoinduced magnetism, metamagnetism, spin-crossover, and charge transfer induced transitions. [7–9,12,15,16,228] The magnetoelastic interactions revealed in heterometallic $[Ru_2(O_2CMe)_4]_3[Cr(CN)_6]$ bring additional understanding of magnetostructural correlations in the development of flexible magnetism and tunable properties in materials where the adaptable cyanide ligands provide important control paths for magnetic coupling between metal centers.

6.2 Vibrational Response Through the 33 K Magnetic Ordering Transition

We already demonstrated that external stimuli like magnetic field in combination with vibrational spectroscopy can be used to reveal local lattice distortions. To gain additional insight into magnetoelastic coupling in $[Ru_2(O_2CMe)_4]_3[Cr(CN)_6]$, we examined the variable temperature infrared response. Figure 6.4(a) and 6.5(a) display the full infrared spectrum. Modes that resonate at 116, 361, 449, and 2138 cm^{-1} harden significantly with decreasing temperature (300-10 K), with $\simeq$4, 6, 12, 7 cm^{-1} shifts, respectively. This is in contrast to trends in several other phonons, for example the 398 cm^{-1} mode, with a frequency shift on the order of 1 cm^{-1} (Fig. 6.4(b)). Moreover, frequency vs. temperature behavior is monotonic with no anomalies at or near the 33 K magnetic ordering transition (example: Fig. 6.4(c)). The latter suggests inherently weak spin-lattice coupling in this material that can be amplified and/or revealed by driving the system towards a collective transition using external magnetic field.

Temperature and magnetic field are often considered to be complementary thermodynamic variables, [103] so similarities between the temperature and field behaviors are anticipated. Perhaps the most important of these relates to the $[Cr(CN)_6]^{3-}$ octahedra, which retain their role as flexible building blocks. This finding is consistent with the overall changes in Cr-C and C≡N bond lengths as compared with Ru-O, Ru-N, and Ru-Ru distances. [235] Interestingly, while hardening of ν(Cr-C) and δ(CrCN) bands is in line with a shorter Cr-C distance at 1.8 K, the blue shift of ν(CN) is in contrast to an elongated C≡N bond. Systems in which a "frequency-bond length" correlation breaks down are known, and we attribute the lack of a simple relationship to superimposed bond length, charge, intermolecular force, and

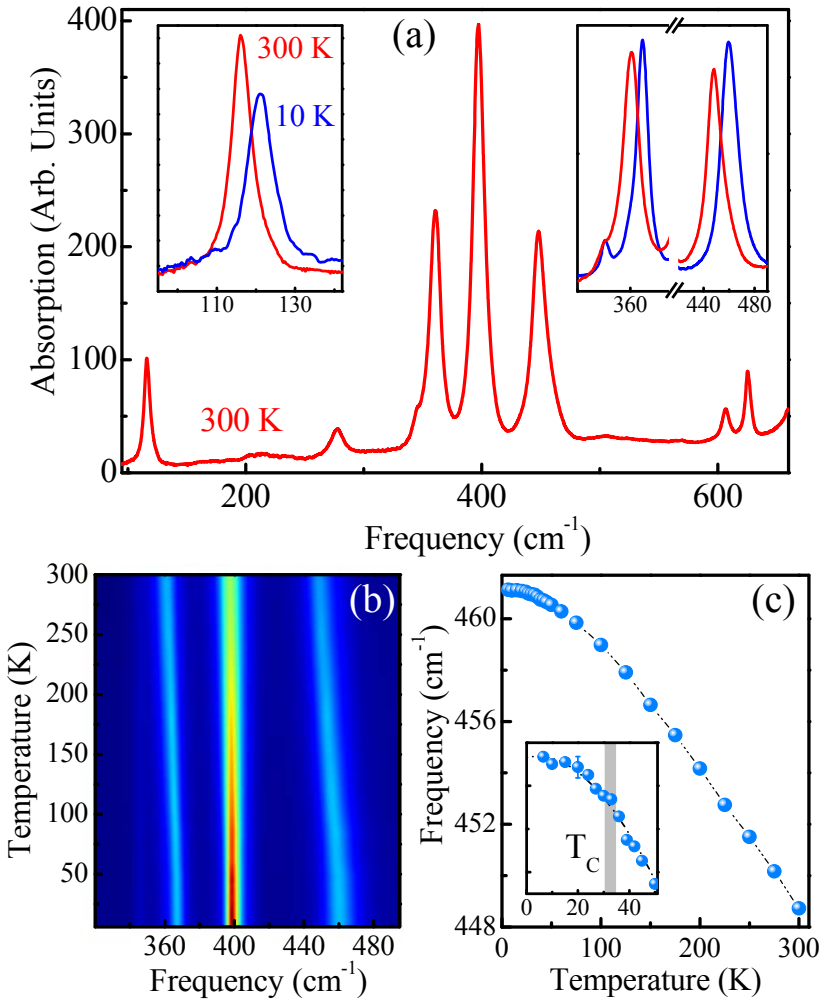

Figure 6.4: (a) The far infrared spectrum of $[Ru_2(O_2CMe)_4]_3[Cr(CN)_6]$ at 300 K. Inset (left): Close-up view of the low frequency δ(C-Cr-C) deformation mode at 300 and 10 K. Inset (right): Close-up view of the ν(Cr-C) and δ(Cr-C-N) modes emphasizing the pronounced frequency shifts between room temperature and 10 K. (b) Image plot of peak intensities as a function of frequency and temperature for the mode cluster near $\simeq$400 cm^{-1}: blue - low intensity, red - high intensity. (c) Frequency vs. temperature behavior for the δ(Cr-C-N) mode. Inset: Close-up view of the systematic frequency variation through the 33 K transition temperature.

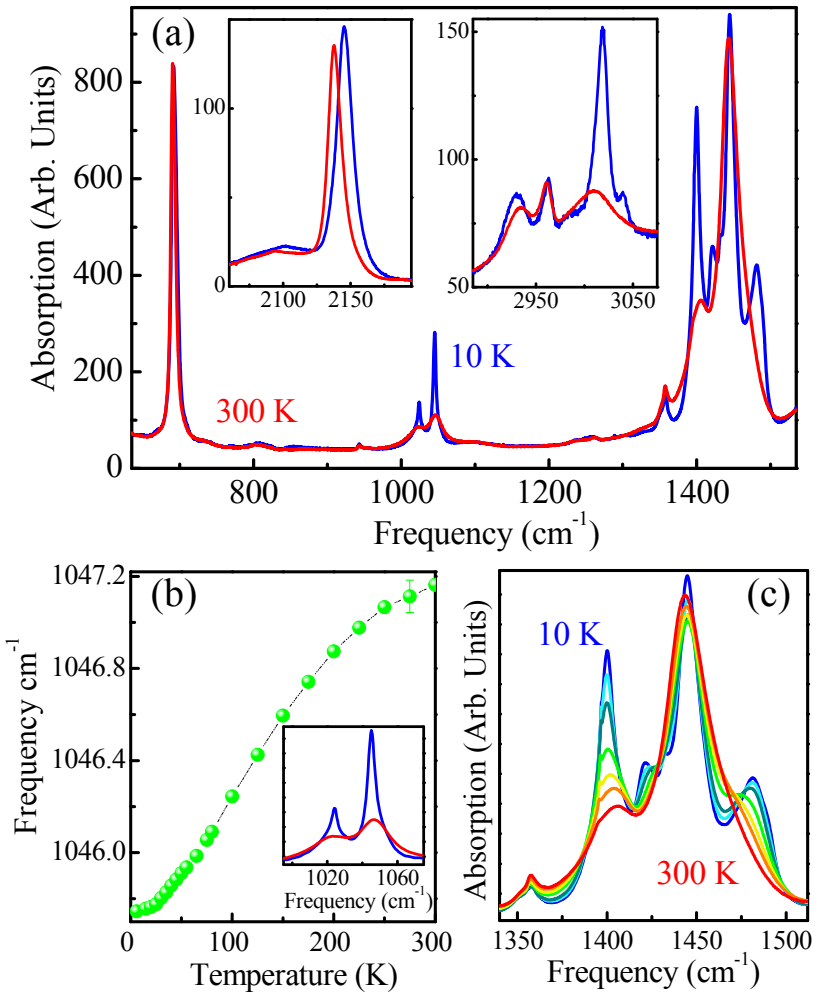

Figure 6.5: (a) Middle-infrared spectrum of the $[Ru_2(O_2CMe)_4]_3[Cr(CN)_6]$ molecular magnet at 300 and 10 K. Insets: Close-up view of the ν(CN) and ν(CH) stretching modes, respectively. (b) Frequency vs. temperature plot for the $\simeq$1040 cm^{-1} peak, displaying an unusual softening. Inset: Close-up view of the high and low temperature spectra near the same peak. (f) Spectral evolution of the $\simeq$1450 cm^{-1} cluster at 10, 30, 50, 100, 150, 200 and 300 K.

collectivity effects. [232, 236–238] In any case, the finding of thermally susceptible $[Cr(CN)_6]^{3-}$ units parallels the situation in magnetic field. Note however, that the overall vibrational behavior is not the same for all features (as seen from the frequency shift of ν(CrC) and δ(CrCN) modes, for example), indicating that even a simple magnetocaloric effect that corresponds to adiabatic change in temperature due to change in field [103] cannot account for these trends. In addition to the frequency shift, the 120 cm^{-1} δ(C-Cr-C) bend also displays damping constant variations (inset, Fig. 6.4(a)) in line with our magnetic field studies. The broader low temperature linewidth in combination with diminished intensity is different than the conventional thermal response (considering simple Bolzmann population factor as an example) and may be indicative of phonon interaction with other excitations and/or states with decreasing temperature. Both temperature and magnetic field seem to suppress this interaction and decouple the phonon.

The $[Ru_2(O_2CMe)_4]_3[Cr(CN)_6]$ temperature dependence reveals several other intriguing trends. For instance, the features near 1045, 1400-1430, and 2930 cm^{-1}, soften down to 10 K (Fig. 6.5), behavior that is opposite to normal lattice contraction tendencies. [235] In addition, the broad cluster of absorptions centered at 1450 cm^{-1} displays interesting fine structure due to simultaneous softening/hardening of the low/high frequency components.[8] Previous work on the $[Ru_2(O_2CMe)_4]_3Cl$ parent compound as well as copper acetate dimer $Cu_2(O_2CMe)_4(H_2O)_2$ allows us to assign modes near 1025 and 1045 cm^{-1} to $\rho(CH_3)$ rocking, the cluster near 1450 cm^{-1} to $\delta(CH_3)$ deformations and $\nu(CO)_{sym/asym}$ stretches, and features centered at 2990 cm^{-1} as $\nu(CH_3)_{sym/asym}$ stretches. [224–226]

Given the nature of these modes and their displacement patterns, the pronounced

[8]The frequency shift of >5 cm^{-1} is observed for some peaks on the low energy side of the 1450 cm^{-1} cluster and >10 cm^{-1} for the component on the high energy part. The exact position of peaks are hard to track above $\simeq$100 K due to their strong overlap.

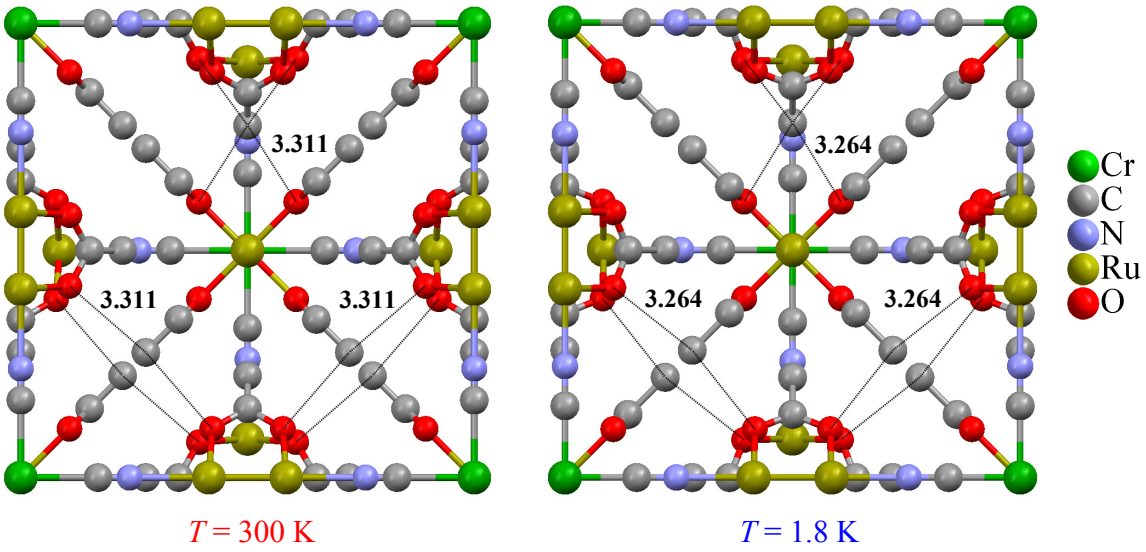

Figure 6.6: $[Ru_2(O_2CMe)_4]_3[Cr(CN)_6]$ crystal structure at 300 and 1.8 K. [235] Dotted/gray lines show examples of intersublattice C···O distances that shorten with decreasing temperature. Hydrogens atoms are omitted for clarity.

changes in the 1450 cm^{-1} cluster of absorptions can be correlated with distortion of the carboxylate unit, specifically relaxation of the CO_2 angle and strengthening of the C-O bond. [235] Previous studies of carboxylato complexes suggest that an increased O-C-O angle leads to a larger splitting of the $\nu(CO)_{sym/asym}$ stretching bands, [239] a result that is in line with the behavior of the 1450 cm^{-1} cluster of absorptions in $[Ru_2(O_2CMe)_4]_3[Cr(CN)_6]$. The latter displays mode softening on its low energy side ($\nu(CO)_{sym}$) and hardening of the high frequency component ($\nu(CO)_{asym}$). We attribute the unusual softening of the selective CH_3-related modes to weak electrostatic intermolecular interactions (for instance of the C-H···O type) that strengthen with decreasing temperature. [59,240] Similar hydrogen-bonding-like interactions involving carboxylate oxygen are present in other diruthenium tetracarboxylates. [88] A closer look at the structure indicates plausible interactions between methyl groups of one sublattice and oxygen atoms of the other. Each methyl group has four short contacts to the neighboring oxygen with C···O distances of 3.311 Å at 300 K (Fig. 6.6). At 1.8 K, C···O distances (3.264 Å) are shorter due to oxygen displacement to-

wards the methyl groups. The latter subsequently affects Ru-O-C and C-O-C angles and the corresponding bond lengths. [235] Stronger intermolecular hydrogen-bonding may foster intersublattice interaction and overall structure stabilization.

Chapter 7

Conclusions

Interest in the foundational aspects of multifunctionality is driving investigation of fundamental coupling mechanisms and structure-property relationships in molecule-based materials. Physical stimuli like magnetic field, pressure, and temperature offer incisive opportunities to tune competing interactions in complex compounds. In this dissertation I present spectroscopic studies of three different types of magnetic systems, $Mn(dca)_2$, $Co(dca)_2$, and $[Ru_2(O_2CMe)_4]_3[Cr(CN)_6]$, through the series of field- and low temperature-driven transformations. The fundamental scientific problems focus the charge-lattice-spin interactions and lattice dynamics with chemical and physical tuning.

We report the discovery of a magnetic quantum phase transition, the development of the complete $B-T$ phase diagram, and the magnetoelastic interaction in $Mn(dca)_2$ molecule-based magnet. From the critical point at $B_c = 30.4$ T we extract the exchange constant $J/k_B \simeq -1.0$ K, in good agreement with the estimate of $J/k_B = -0.78$ K from heat capacity measurements. [73] Importantly, we show that the field-driven antiferromagnetic $\rightarrow$ fully polarized state transition has an intrinsic magnetostructural coupling associated with it. The magnetoelastic interactions are manifested through the sensitivity of majority of the vibrational modes to applied

field, a finding that we analyze in terms of the local structure deformations on approach to new magnetic state. The strong correlation between the phonon behavior and the magnetization through the magnetic quantum phase transition suggests that lattice flexibility plays an important role in establishing the fully polarized high field state. Based on our complementary lattice dynamics calculations and the analysis of displacement patterns, we conclude that the primary local structural changes involve a combined MnN_6 octahedra distortion and a counter-rotation mechanism that relieve the additional magnetic energy imposed by applied field. Our variable temperature studies on the other hand, demonstrate that the development of long range antiferromagnetic order in $Mn(dca)_2$ at 15.85 K takes place with no substantial lattice involvement, indicating that spin-lattice mixing is inherently weak in this material. Thus, in addition to revealing how the magnetic quantum critical transition amplifies spin-lattice interactions in this molecule-based material, we show that applied field mediates the delicate interplay between these interactions to reversibly tune and control the ground state. The local lattice distortions that take place through the quantum phase transition in $Mn(dca)_2$ have counterparts in ferroelectric perovskites, multiferroics, photo-magnetic metal cyanides, and hexahalometallates like, A_2TeX_6 where similar structural and coupling processes contribute to their functionality. [201–205, 241, 242]

To gain further understanding of variable coupling phenomena in molecule-based magnets we probe magnetic field- and temperature-induced changes in the vibrational properties of $Co(dca)_2$ and compare our findings with lattice dynamics calculations and magnetization measurements. We find large magnetic anisotropy D=12$\pm$4 cm^{-1}, a direct consequence of the substantial Co^{2+} spin-orbit coupling and crystal-field effects. Furthermore, our spectroscopic studies reveal two classic signatures of charge-lattice-spin interactions: (i) electron-phonon coupling in which electronic excitation

interacts with the optical phonons and (i) magnetoelastic coupling in which magnetostriction effects manifest themselves in the microscopic phonon response. The interaction between electronic and lattice degrees of freedom is evident as a field-driven avoided crossings of the low-lying Co^{2+} crystal field excitation with the low frequency ligand phonons. We find the energy of the electronic transition to be 114±5 cm^{-1} and the corresponding electron-phonon coupling constants to be 2-3 cm^{-1}. The spin-lattice interaction reveals itself in a sensitivity of selective vibrational modes to applied magnetic field. The dominant effects are seen in the ν(Co-N) and ν(CN) stretching bands signaling a local lattice deformation in the Co^{2+} environment and bridging linkages. Taken together, these findings demonstrate that the intrinsic coupling processes in $Co(dca)_2$ are exceptionally tunable and take place over multiple energy scales, findings that add to the rich character of $M^{II}(dca)_2$ molecule-based magnets. More generally, this work broadens our understanding of coupling in multifunctional materials, where many exotic properties derive from charge-lattice-spin interactions rather than a separation of the different degrees of freedom.

To understand the structure-property relationship in a heterometallic system with interpenetrating magnetic networks, we combined high field vibrational spectroscopies with an analysis of mode displacement patterns and trends to reveal the magnetoelastic coupling in $[Ru_2(O_2CMe)_4]_3[Cr(CN)_6]$. We find that high magnetic field competes with antiferromagnetic exchange interactions and distorts the $[Cr(CN)_6]^{3-}$ molecular unit. Systematic changes in ν(CN) and the Cr-containing phonons provide evidence for overall $[Cr(CN)_6]^{3-}$ flexibility and, more specifically, a slightly compressed CrC_6 octahedron and relaxed CN linkages, distortions that accommodate the developing magnetic state. The sublattice coalescence transition at $B_c \simeq 0.08$ T, by contrast, takes place without substantial spin-lattice interactions, indicating its pure magnetic origin. Variable temperature spectroscopy reinforces the finding of

an adaptable chromium environment that strengthens gradually at low temperature. The understanding of magnetoelastic coupling in $[Ru_2(O_2CMe)_4]_3[Cr(CN)_6]$ provides insight into other chromium-containing materials where spin-lattice interactions contribute to ground state stabilization. [243–245] Moreover, distinctions between elastic vs. rigid molecular units and adaptable vs. static crystal environments are useful where building block choices figure into the design and control of materials for technological applications. [35, 233]

Taken together, these comprehensive findings extend our knowledge on competing interactions in magnetic molecular solids and provide additional impetus to profound investigation of their tunable behavior. Moreover, they offer fundamental insight into the behavior of higher-energy scale materials like transition metal oxides, where interactions over multiple energy scales impact a variety of physical properties. In addition, these results are also relevant to understanding of more complicated processes in which magnetic field acts as a tuning parameter like multiferroicity, [246,247] multiple magnetization plateaus, [248, 249] and skyrmion lattice development. [250]

Bibliography

Bibliography

[1] J. M. D. Coey, *Magnetism and Magnetic Materials* (Cambridge University Press, New York, 2010).

[2] J. S. Miller and A. J. Epstein, Angew. Chem. Int. Ed. Engl. **33**, 385 (1994).

[3] D. Pinkowicz, S. Chorąży, and O. Stefańczyk, Science Progress **94**, 139 (2011).

[4] S. J. Blundell and F. L. Pratt, J. Phys.: Condens. Matter **16**, R771 (2004).

[5] J. S. Miller, Chem. Soc. Rev. **40**, 3266 (2011).

[6] J. S. Miller, Dalton Trans. 2742 (2006).

[7] M. Verdaguer, A. Bleuzen, V. Marvaud, J. Vaissermann, M. Seuleiman, C. Desplanches, A. Scuiller, C. Train, R. Garde, G. Gelly, C. Lomenech, I. Rosenman, P. Veillet, C. Cartier, and F. Villain, Coord. Chem. Rev. **190-192**, 1023 (1999).

[8] S. M. Holmes and G. S. Girolami, J. Am. Chem. Soc. **121**, 5593 (1999).

[9] Ø. Hatlevik, W. E. Buschmann, J. Zhang, J. L. Manson, and J. S. Miller, Adv. Mater. **11**, 914 (1999).

[10] J. M. Manriquez, G. T. Yee, R. S. McLean, A. J. Epstein, J. S. Miller, Science, **252**, 1415 (1991).

[11] K. I. Pokhodnya, A. J. Epstein, and J. S. Miller, Adv. Mater. **12**, 410 (2000).

[12] O. Sato, T. Iyoda, A. Fujishima, and K. Hashimoto, Science **272**, 704 (1996).

[13] O. Sato, S. Hayami, Y. Einaga, and Z.-Z. Gu, Bull. Chem. Soc. Jpn. **76**, 443 (2003).

[14] P. Gutlich, Y. Garcia, and H. A. Goodwin, Chem. Soc. Rev. **29**, 419 (2000).

[15] W. Kosaka, K. Nomura, K. Hashimoto, and S. Ohkoshi, J. Am. Chem. Soc. **127**, 8590 (2005).

[16] M. G. Hilfiger, M. Chen, T. V. Brinzari, T. M. Nocera, M. Shatruk, D. T. Petasis, J. L. Musfeldt, C. Achim, and K. R. Dunbar, Angew. Chem. Int. Ed. **49**, 1410 (2010).

[17] R. Sessoli, Nature Chem. **2**, 346 (2010).

[18] S. Ohkoshi, K. Imoto, Y. Tsunobuchi, S. Takano, and H. Tokoro, Nature Chem. **3**, 564 (2011).

[19] C. Mathonière, S. G. Carling, D. Yusheng, and P. Day, J. Chem. Soc., Chem. Commun. 1551 (1994).

[20] W. E. Buschmann, S. C. Paulson, C. M. Wynn, M. Girtu, A. J. Epstein, H. S. White, and J. S. Miller, Chem. Mater. **10**, 1386 (1998).

[21] R. Sessoli, D. Gatteschi, A. Caneschi, and M. A. Novak, Nature **365**, 141 (1993).

[22] G. Christou, D. Gatteschi, D. N. Hendrickson, and R. Sessoli, MRS Bull. **25**, 66 (2000).

[23] A. Caneschi, D. Gatteschi, N. Lalioti, C. Sangregorio, R. Sessoli, G. Venturi, A. Vindigni, A. Rettori, M. G. Pini, and M. A. Novak, Angew. Chem., Int. Ed. **40**, 1760 (2001).

[24] L. Bogani, A. Vindigni, R. Sessoli, and D. Gatteschi, J. Mater. Chem. **18**, 4750 (2008).

[25] L. Bogani and W. Wernsdorfer, Nature Mat. **7**, 179 (2008).

[26] C. Rovira, Chem. Eur. J. **6**, 1723 (2000).

[27] A. Shapiro, C. P. Landee, M. M. Turnbull, J. Jornet, M. Deumal, J. J. Novoa, M. A. Robb, and W. Lewis, J. Am. Chem. Soc. **129**, 952 (2007).

[28] I. Ratera and J. Veciana, Chem. Soc. Rev. **41**, 303 (2012).

[29] S. Chittipeddi, K. R. Cromack, J. S. Miller, A. J. Epstein, Phys. Rev. Lett. **58**, 2695 (1987).

[30] J. -H. Her, P. W. Stephens, J. Ribas-Ariño, J. J. Novoa, W. W. Shum, and J. S. Miller, Inorg. Chem. **48**, 3296 (2009).

[31] K. S. Min, A. L. Rhinegold, and J. S. Miller, Inorg. Chem. **44**, 8433 (2005).

[32] W. Dong, L. -N. Zhu, H. -B. Song, D. -Z. Liao, Z. -H. Jiang, S. -P. Yan, P. Cheng, S. Gao, Inorg. Chem. **43**, 2465 (2004).

[33] M. Verdaguer and G. Girolami, in *Magnetism: Molecules to Materials V*, edited by J. S. Miller and M. Drillon (Wiley-VCH, Weinheim, 2005), p. 283.

[34] S. Ferlay, T. Mallah, R. Ouahes, P. Veillet, and M. Verdaguer, Nature **378**, 701 (1995).

[35] H. Tokoro and S. Ohkoshi, Dalton Trans. **40**, 6825 (2011).

[36] H. Tamaki, Z. J. Zhong, N. Matsumoto, S. Kida, M. Koikawa, N. Achiwa, Y. Hashimoto, and H. Okawa, J. Am. Chem. Soc. **114**, 6974 (1992).

[37] C. Mathonière, C. J. Nuttall, S. G. Carling, and P. Day, Inorg. Chem. **35**, 1201 (1996).

[38] E. Coronado, J. R. Galán-Mascarós, C. J. Gómez-García, and V. Laukhin, Nature **408**, 447 (2000).

[39] J. R. Galán-Mascarós and E. Coronado, C. R. Chimie **11**, 1110 (2008).

[40] D. N. Basov, R. D. Averitt, D. van der Marel, M. Dressel, and K. Haule, Rev. Mod. Phys. **85**, 471 (2011).

[41] M. Dressel, Quantum criticality in organic conductors? Fermi liquid versus non-Fermi-liquid behaviour. J. Phys.: Condens. Matter **23**, 293201 (2011). (Published 5 July 2011, doi:10.1088/0953-8984/23/29/293201)

[42] P. K. Siwach, H. K. Singh, and O. N. Srivastava, J. Phys.: Condens. Matter. **20**, 273201 (2008).

[43] T. T. A. Lummen, P. Chen, M. O. Ramirez, E. Barnes, N. J. Podraza, J. L. Musfeldt, and V. Gopalan, *Optical probing of spin-charge-lattice coupling in multiferroics* in *Multiferroics: Synthesis, Characterization and Applications*, edited by R. Ramesh and M. Lane (Wiley) *Accepted for publication.*

[44] T. J. Liu, J. Hu, B. Qian, D. Fobes, Z. Q. Mao, W. Bao, M. Reehuis, S. A. J. Kimber, K. Prokeˇ, S. Matas, D. N. Argyriou, A. Hiess, A. Rotaru, H. Pham, L. Spinu, Y. Qiu, V. Thampy, A. T. Savici, J. A. Rodriguez, and C. Broholm, Nature Mater. **9**, 716 (2010). (doi:10.1038/nmat2800)

[45] S. M. Dunaevskiĭ, Magnetic Phase Diagrams of Manganites in the Electron Doping Region. Phys. Solid State **46**, 193 (2004). Translated from Fiz. Tverd. Tela **46**, 193 (2004).

[46] S. E. Sebastian, N. Harrison, C. D. Batista, L. Balicas, M. Jaime, P. A. Sharma, N. Kawashima, and I. R. Fisher, Nature **441**, 617 (2006).

[47] R. C. Rai, J. Cao, S. Brown, J. L. Musfeldt, D. Kasinathan, D. J. Singh, G. Lawes, N. Rogado, R. J. Cava, and X. Wei, Phys. Rev. B **74**, 235101 (2006). (http://link.aps.org/abstract/PRB/v74/e235101)

[48] A. M. Kadomtseva, S. S. Krotov, Yu. F. Popov, and G. P. Vorob'ev, Low Temp. Phys. **32**, 709 (2006).

[49] B. Lorenz, F. Yen, M. M. Gospodinov, and C. W. Chu, Phys. Rev. B **71**, 014438 (2005).

[50] M. Ohkawa, A comparative review of physical properties in the hydrated cobaltate superconductor. Physica B **405**, 3057-3062 (2010). (http://dx.doi.org/10.1016/j.physb.2010.04.028)

[51] T. E. Vos, Y. Liao, W. W. Shum, J.-H. Her, P. W. Stephens, W. M. Reiff, and J. S. Miller. J. Am. Chem. Soc. **126**, 11630 (2004).

[52] G. Lazari, T. C. Stamatatos, C. P. Raptopoulou, V. Psycharis, M. Pissas, S. P. Perlepes, and A. K. Boudalis. Dalton Trans. 3215, (2009).

[53] P. A. Goddard, J. Singleton, P. Sengupta, R. D. McDonald, T. Lancaster, S. J. Blundell, F. L. Pratt, S. Cox, N. Harrison, J. L. Manson, and J. A. Schlueter, New J. Phys. **10**, 083025 (2008).

[54] J. L. Musfeldt, L. I. Vergara, T. V. Brinzari, C. Lee, L. C. Tung, J. Kang, Y. J. Wang, J. A. Schlueter, J. L. Manson, and M. -H. Whangbo, Phys. Rev. Lett. **103**, 157401 (2009).

[55] J. L. White, C. Lee, Ö. Günaydın-Şen, L. C. Tung, H. M. Christen, Y. J. Wang, M. M. Turnbull, C. P. Landee, R. D. McDonald, S. A. Crooker, J. Singleton, M. -H. Whangbo, and J. L. Musfeldt, Phys. Rev. B **81**, 052407 (2010).

[56] X. S. Xu, J. de Groot, Q. -C. Sun, B. C. Sales, D. Mandrus, M. Angst, A. P. Litvinchuk, and J. L. Musfeldt, Phys. Rev. B **82**, 014304 (2010).

[57] J. F. Karpus, C. S. Snow, R. Gupta, H. Barath, S. L. Cooper, and G. Cao, Phys. Rev. B **73**, 134407 (2006).

[58] A. Speghini, M. Bettinelli, U. Caldiño, M. O. Ramírez, D. Jaque, L. E. Bausá, and J. García Solé. J. Phys. D: Appl. Phys. **39**, 4930 (2006).

[59] T. V. Brinzari, C. Tian, G. J. Halder, J. L. Musfeldt, M. -H. Whangbo, and J. A. Schlueter, Inorg. Chem. **48**, 7650 (2009).

[60] W. Breitling, W. Lehmann, T. P. Srinivasan, R. Weber, and U. Dürr, Solid State Commun. **24**, 267 (1977).

[61] T. D. Kang, E. Standard, K. H. Ahn, A. A. Sirenko, G. L. Carr, S. Park, Y. J. Choi, M. Ramazanoglu, V. Kiryukhin, and S.-W. Cheong, Phys. Rev. B **82**, 014414 (2010).

[62] D. J. Lockwood, G. Mischler, I. W. Johnstone, and M. C. Schmidt, J. Phys. C: Solid State Phys. **12**, 1955 (1979).

[63] Ch. Kant, T. Rudolf, F. Schrettle, F. Mayr, J. Deisenhofer, P. Lunkenheimer, M. V. Eremin, and A. Loidl, Phys. Rev. B **78**, 245103 (2008).

[64] R. V. Aguilar, A. B. Sushkov, C. L. Zhang, Y. J. Choi, S. -W. Cheong, and H. D. Drew, Phys. Rev. B **76**, 060404(R) (2007).

[65] C. A. Helms, J. F. Scott, and D. J. Toms, J. Raman Spectrosc. **8**, 335 (1979).

[66] J. S. Miller and J. L. Manson, Acc. Chem. Res. **34**, 563 (2001).

[67] S. R. Batten and K. S. Murray, Coord. Chem. Rev. **246**, 103 (2003).

[68] J. L. Manson, in *Magnetism: Molecules to materials V*, edited by J. S. Miller and M. Drillon (Wiley-VCH, Weinheim, 2005), p. 71.

[69] J. L. Manson, C. R. Kmety, Q. Huang, J. W. Lynn, G. M. Bendele, S. Pagola, P. W. Stephens, L. M. Liable-Sands, A. L. Rheingold, A. J. Epstein, and J. S. Miller, Chem. Mater. **10**, 2552 (1998).

[70] M. Kurmoo and C. J. Kepert, New. J. Chem. **22**, 1515 (1998).

[71] S. R. Batten, P. Jensen, C. J. Kepert, M. Kurmoo, B. Moubaraki, K. S. Murray, and D. J. Price. J. Chem. Soc., Dalton Trans. 2987 (1999).

[72] C. J. Nuttall, T. Takenobu, Y. Iwasa, and M. Kurmoo, Mol. Cryst. and Liq. Cryst. **343**, 227 (2000).

[73] C. R. Kmety, Q. Huang, J. W. Lynn, R. W. Erwin, J. L. Manson, S. McCall, J. E. Crow, K. L. Stevenson, J. S. Miller, and A. J. Epstein, Phys. Rev. B **62**, 5576 (2000).

[74] J. L. Manson, C. R. Kmety, F. Palacio, A. J. Epstein, and J. S. Miller, Chem. Mater. **13**, 1068 (2001).

[75] A. Lappas, A. S. Wills, M. A. Green, K. Prassides, and M. Kurmoo, Phys. Rev. B **67**, 144406 (2003).

[76] D. O. Demchenko, A. Y. Liu, E. Z. Kurmaev, L. D. Finkelstein, V. R. Galakhov, A. Moewes, S. G. Chiuzbaian, M. Neumann, C. R. Kmety, and K. L. Stevenson, Phys. Rev. B **69**, 205105 (2004).

[77] H. Köhler, *Chemistry of Pseudohalides*, edited by A. M. Golub, H. Köhler, and V. V. Skopenko (Elsevier, Amsterdam, 1986).

[78] O. Kahn, *Molecular magnetism* (VCH, New York, 1993).

[79] C. R. Kmety, J. L. Manson, S. McCallc, J. E. Crow, K. L. Stevensond, and A. J. Epstein, J. Magn. Magn. Mater. **248**, 52 (2002).

[80] C. R. Kmety, J. L. Manson, Q. Huang, J. W. Lynn, R. W. Erwin, J. S. Miller, and A. J. Epstein, Phys. Rev. B **60**, 60 (1999).

[81] J. L. Manson, D. W. Lee, A. L. Rheingold, and J. S. Miller, Inorg. Chem. **37**, 5966 (1998).

[82] F. A. Cotton, N. F. Curtis, C. B. Harris, B. F. G. Johnson, S. J. Lippard, J. T. Mague, W. R. Robinson, and J. S. Wood, Science **145**, 1305 (1964).

[83] F. A. Cotton, C. A. Murillo, and R. A. Walton, *Multiple Bonds between Metal Atoms*, edited by F. A. Cotton, C. A. Murillo, and R. A. Walton (3rd ed., Springer, New York, 2005).

[84] T. Nguyen, A. D. Sutton, M. Brynda, J. C. Fettinger, G. J. Long, and P. P. Power, Science, **310**, 844 (2005).

[85] Y. -C. Tsai, H. -Z. Chen, C. -C. Chang, J. -S. K. Yu, G. -H. Lee, Y. Wang, and T. -S. Kuo, J. Am. Chem. Soc. **131**, 12534 (2009).

[86] J. G. Norman, Jr., G. E. Renzoni, and D. A. Case, J. Am. Chem. Soc. **101**, 5256 (1979).

[87] M. Mikuriya, D. Yoshioka, and M. Handa, Coord. Chem. Rev. **250**, 2194 (2006).

[88] M. A. S. Aquino, Coord. Chem. Rev. **248**, 1025 (2004).

[89] Y. Liao, W. W. Shum, and J. S. Miller. J. Am. Chem. Soc. **124**, 9336 (2002).

[90] J. S. Miller, T. E. Vos, and W. W. Shum, Adv. Mater. **17**, 2251 (2005).

[91] D. Yoshioka, M. Mikuriya, and M. Handa, Chem. Lett. **31**, 1044 (2002).

[92] T. E. Vos and J. S. Miller, Angew. Chem. Int. Ed. **44**, 2416 (2005).

[93] B. S. Kennon, K. H. Stone, P. W. Stephens, and J. S. Miller. CrystEngComm. **11**, 2185 (2009).

[94] T. Maeda, M. Mito, H. Deguchi, S. Takagi, W. Kaneko, M. Ohba, and H. Okawa, Polyhedron **24**, 2497 (2005).

[95] L. Egan, K. Kamenev, D. Papanikolaou, Y. Takabayashi, and S. Margadonna, J. Am. Chem. Soc. **128**, 6034 (2006).

[96] R. S. Fishman, S. Okamoto, W. W. Shum, and J. S. Miller. Phys. Rev. B **80**, 064401 (2009).

[97] R. S. Fishman and J. S. Miller. Phys. Rev. B **83**, 094433 (2011).

[98] W. W. Shum, J. N. Schaller, and J. S. Miller. J. Phys. Chem. C **112**, 7936 (2008).

[99] W. W. Shum, J. -H. Her, P. W. Stephens, Y. Lee, and J. S. Miller. Adv. Mater. **19**, 2910 (2007).

[100] R. S. Fishman, W. W. Shum, and J. S. Miller. Phys. Rev. B **81**, 172407 (2010).

[101] A. G. Olabi, and A. Grunwald, Mater. Des. **29**, 469 (2008).

[102] A. V. Andreev and N. V. Mushnikov, in *Concise encyclopedia of magnetic and superconducting materials*, edited by K. H. J. Buschow (2nd ed., Elsevier, Amsterdam, 2005), p. 766.

[103] *Magnetism: fundamentals*, edited by E. du Trémolet de Lacheisserie, D. Gignoux, and M. Schlenker (Springer Science, Boston, 2005).

[104] E. W. Lee, Rep. Prog. Phys. **18**, 184 (1955).

[105] Y. Shapira, R. D. Yacovitch, C. C. Becerra, S. Foner, E. J. McNiff, Jr., and D. R. Nelson, Phys. Rev. B **14**, 3007 (1976).

[106] E. Callen and H. B. Callen, Phys. Rev. B **139**, A455 (1965).

[107] Y. Shapira and N. F. Oliveira, Jr., Phys. Rev. B **18**, 1425 (1978).

[108] J. W. Bray, L. V. Interrante, I. S. Jacobs, and J. Bonner, in *Extended Linear Chain Compounds*, edited by J. S. Miller (Plenum, New York, 1983), Vol 3.

[109] M. Hase, I. Terasaki, and K. Uchinokura, Phys. Rev. Lett. **70**, 3651 (1993).

[110] J. W. Bray, H. R. Hart, Jr. , L. V. Interrante, I. S. Jacobs, J. S. Kasper, G. D. Watkins, S. H. Wee, and J. C. Bonner, Phys. Rev. Lett. **35**, 744 (1975).

[111] H. Kuroe, T. Sekine, M. Hase, Y. Sasago, K. Uchinokura, H. Kojima, I. Tanaka, and Y. Shibuya, Phys. Rev. B **50**, 16468 (1994).

[112] P. H. M. van Loosdrecht, J. P. Boucher, G. Martinez, G. Dhalenne, and A. Revcolevschi, Phys. Rev. Lett. **76**, 311 (1996). (http://link.aps.org/abstract/PRL/v76/p311)

[113] I. Loa, S. Gronemeyer, C. Thomsen, and R. K. Kremer, Solid State Commun. **99**, 231 (1996).

[114] M. N. Popova, A. B. Sushkov, S. A. Golubchik, A. N. Vasil'ev, and L. I. Leonyuk, Phys. Rev. B **57**, 5040 (1998).

[115] A. Damascelli, D. van der Marel, G. Dhalenne, and A. Revcolevschi, Phys. Rev. B **61**, 12063 (2000). (http://link.aps.org/abstract/PRB/v61/p12063)

[116] U. Fano, Phys. Rev. **124**, 1866 (1961).

[117] A. R. Goñi, T. Zhou, U. Schwarz, R. K. Kremer, and K. Syassen, Phys. Rev. Lett. **77**, 1079 (1996).

[118] P. H. M. van Loosdrecht, J. P. Boucher, G. Martinez, G. Dhalenne, and A. Revcolevschi, J. Appl. Phys. **79**, 5395 (1996).

[119] I. Loa, S. Gronemeyer, C. Thomsen, and R. K. Kremer, Z. Phys. Chem. (Munich) **201**, 333 (1997).

[120] K. Takehana, T. Takamasu, M. Hase, and G. Kido, and K. Uchinokura, Phys. Rev. B **62**, 5191 (2000).

[121] Y. Yamashita and K. Ueda, Phys. Rev. Lett. **85**, 4960 (2000).

[122] O. Tchernyshyov, R. Moessner, and S. L. Sondhi, Phys. Rev. B. **66**, 064403 (2002).

[123] S. -H. Lee, C. Broholm, T. H. Kim, W. Ratcliff II, and S. -W. Cheong, Phys. Rev. Lett. **84**, 3718 (2000).

[124] M. T. Rovers, P. P. Kyriakou, H. A. Dabkowska, G. M. Luke, M. I. Larkin, and A. T. Savici, Phys. Rev. B. **66**, 174434 (2002).

[125] A. B. Sushkov, O. Tchernyshyov, W. Ratcliff II, S. W. Cheong, and H. D. Drew, Phys. Rev. Lett. **94**, 137202 (2005).

[126] T. Rudolf, Ch. Kant, F. Mayr, J. Hemberger, V. Tsurkan, and A. Loidl, New J. Phys. **9**, 76 (2007).

[127] R. V. Aguilar, A. B. Sushkov, Y. J. Choi, S. -W. Cheong, and H. D. Drew, Phys. Rev. B. **77**, 092412 (2008).

[128] Ch. Kant, J. Deisenhofer, T. Rudolf, F. Mayr, F. Schrettle, A. Loidl, V. Gnezdilov, D. Wulferding, P. Lemmens, and V. Tsurkan, Phys. Rev. B **80**, 214417 (2009). (http://link.aps.org/abstract/PRB/v80/e214417)

[129] J. Deisenhofer, P. Lemmens, in *Introduction to frustrated magnetism: materials, experiments, theory*, edited by C. Lacroix, P. Mendels, and F. Mila (Springer-Verlag, Berlin, 2011), p. 107.

[130] W. Baltensperger and J. S. Helman, Helv. Phys. Acta **41**, 668 (1968).

[131] D. J. Lockwood and M. G. Cottam, J. Appl. Phys. **64**, 5876 (1988).

[132] X. K. Chen, J. C. Irwin, and J. P. Franck, Phys. Rev. B **52**, R13130 (1995).

[133] J. S. Lee,T. W. Noh, J. S. Bae, I. -S. Yang, T. Takeda, and R. Kanno, Phys. Rev. B **69**, 214428 (2004).

[134] Ch. Kant, F. Mayr, T. Rudolf, M. Schmidt, F. Schrettle, and J. Deisenhofer, A. Loidl, Eur. Phys. J. Special Topics **180**, 43 (2010).

[135] T. R. McGuire and W. A. Crapo, J. Appl. Phys. **33**, 1291 (1962).

[136] W. S. Ferreira, J. Agostinho Moreira, A. Almeida, M. R. Chaves, J. P. Araújo, J. B. Oliveira, J. M. Machado Da Silva, M. A. Sá, T. M. Mendonça, P. Simeão Carvalho, J. Kreisel, J. L. Ribeiro, L. G. Vieira, P. B. Tavares, and S. Mendonça, Phys. Rev. B **79**, 054303 (2009).

[137] E. Granado, A. Garca, J. A. Sanjurjo, C. Rettori, I. Torriani, F. Prado, R. D. Sanchez, A. Caneiro, and S. B. Oseroff, Phys. Rev. B **60**, 11879 (1999).

[138] A. P. Litvinchuk, M. N. Iliev, V. N. Popov, and M. M. Gospodinov, J. Phys.: Condens. Matter **16**, 809 (2004).

[139] J. Laverdière, S. Jandl, A. A. Mukhin, V. Yu. Ivanov, V. G. Ivanov, and M. N. Iliev, Phys. Rev. B **73**, 214301 (2006).

[140] J. F. Karpus, R. Gupta, H. Barath, S. L. Cooper, and G. Cao, Phys. Rev. Lett. **93**, 167205 (2004).

[141] R. Gupta, M. Kim, H. Barath, S. L. Cooper, and G. Cao, Phys. Rev. Lett. **96**, 067004 (2006).

[142] F. Wang and A. Vishwanath, Phys. Rev. Lett. **100**, 077201 (2008).

[143] M, K. Singh, W. Prellier, H. M. Jang, and R. S. Katiyar, Solid State Commun. **149**, 1971 (2009).

[144] A. F. García-Flores, E. Granado, H. Martinho, R. R. Urbano, C. Rettori, E. I. Golovenchits, V. A. Sanina, S. B. Oseroff, S. Park, and S. -W. Cheong, Phys. Rev. B **73**, 104411 (2006).

[145] J. H. Lee, L. Fang, E. Vlah, X. Ke, Y. W. Jung, L. F. Kourkoutis, J.-W. Kim, P. J. Ryan, T. Heeg , M. Roeckerath, V. Goian, M. Bernhagen, R. Uecker, P. C. Hammel, K. M. Rabe, S. Kamba, J. Schubert, J. W. Freeland, D. A.

Muller, C. J. Fennie, P. Schiffer, V. Gopalan, E. Johnston-Halperin, and D. G. Schlom, Nature **466**, 954 (2010).

[146] J. Cao, L. I. Vergara, J. L. Musfeldt, A. P. Litvinchuk, Y. J. Wang, S. Park, and S. -W. Cheong, Phys. Rev. Lett. **100**, 177205 (2008).

[147] Y. Narumi, K. Katsumata, U. Staub, K. Kindo, M. Kawauchi, C. Broennimann, H. Toyokawa, Y. Tanaka, A. Kikkawa, T. Yamamoto, M. Hagiwara, T. Ishikawa, and H. Kitamura, J. Phys. Soc. Jpn., **75**, 075001 (2006).

[148] M. Kim, X. M. Chen, Y. I. Joe, E. Fradkin, P. Abbamonte, and S. L. Cooper, Phys. Rev. Lett. **104**, 136402 (2010).

[149] S. Mukherjee, A. Garg, and R.Gupta, J. Phys.: Condens. Matter **23**, 445403 (2011).

[150] J. Lorenzana and G. A. Sawatzky, Phys. Rev. Lett. **74**, 1867 (1995).

[151] T. M. Holden, W. J. L. Buyers, E. C. Svensson, R. A. Cowley, M. T. Huthchingsts, D. Hukini, and R. W. H. Stevenson, J. Phys. C: Solid St. Phys. **4**, 2127 (1971).

[152] A. Pimenov, A. A. Mukhin, V. Yu. Ivanov, V. D. Travkin, A. M. Balbashov, and A. Loidl, Nat. Phys. **2**, 97 (2006).

[153] A. B. Sushkov, M. Mostovoy, R. Valdés Aguilar, S.-W. Cheong, and H. D. Drew, J. Phys.: Condens. Matter **20**, 434210 (2008).

[154] L. I. Vergara, J. Cao, L.-C. Tung, N. Rogado, F. Yen, Y. Q. Wang, R. J. Cava, B. Lorenz, Y.-J. Wang, and J. L. Musfeldt, Phys. Rev. B **81**, 012403 (2010).

[155] M. Kim, X. M. Chen, X. Wang, C. S. Nelson, R. Budakian, P. Abbamonte, and S. L. Cooper, Phys. Rev. B **84**, 174424 (2011).

[156] Ö. Günaydın-Şen, C. Lee, L. C. Tung, P. Chen, M. M. Turnbull, C. P. Landee, Y. J. Wang, M. -H. Whangbo, and J. L. Musfeldt, Phys. Rev. B **81**, 104307 (2010).

[157] A. B. Sushkov, J. L. Musfeldt, Y. J. Wang, R. M. Achey, and N. S. Dalal, Phys. Rev. B **66**, 144430 (2002).

[158] J. R. Ferraro, K. Nakamoto, and C. W. Brown, *Introductory Raman Spectroscopy* (2nd ed., Academic Press, San Diego, 2003).

[159] P. F. Bernath, *Spectra of Atoms and Molecules* (Oxford University Press, New York, 1995).

[160] B. C. Smith, *Fundamentals of Fourier Transform Infrared Spectroscopy* (2nd ed., CRC Press, Taylor and Francis Group, LLC., Boca Raton, 2011).

[161] P. J. Larkin, *Infrared and Raman spectroscopy: principles and spectral interpretation* (Elsevier, San Diego, 2011).

[162] K. D. Mielenz and R. Mavrodineanu, J. Res. Natl. Bur. Stand. Sec. A **77**, 699, (1973).

[163] P. M. A. Sherwood, *Vibrational Spectroscopy of solids* (Cambridge University Press, Cambridge, 1972).

[164] N. J. Everall, in *Handbook of Vibrational Spectroscopy*, edited by J. M. Chalmer and P. R. Griffiths (John Wiley and Sons Ltd, Chichester, 2002), Vol. 1, p. 141.

[165] C. Kittel, *Introduction to Solid State Physics* (Wiley, New York, 2005).

[166] F. A. Cotton, *Chemical Applications of Group Theory*. (2nd ed., Wiley-Interscience, New York, 1971).

[167] W. G. Fateley, F. R. Dollish, N. T. McDevitt, and F. F. Bentley, *Infrared and Raman selection rules for molecular and lattice vibrations: the correlation method* (Wiley-Interscience, New York, 1972).

[168] F. Wooten, *Optical Properties of Solids* (Academic Press, New York, 1972).

[169] H. Kuzmany, *Solid-State Spectroscopy*, (2nd ed., Springer, Berlin, 2009).

[170] M. Fox, *Optical Properties of Solids* (Oxford University press, New York, 2001).

[171] P. R. Griffiths and C. Homes, in *Handbook of Vibrational Spectroscopy*, edited by J. M. Chalmer and P. R. Griffiths (John Wiley and Sons Ltd, Chichester, 2002), Vol. 1, p. 326.

[172] P. R. Griffiths, J. A. de Haseth, *Fourier transform infrared spectrometry* (2nd ed., John Wiley and Sons Inc, Hoboken, 2007).

[173] A. Simon, J. Gast, and A. Keens, U.S. Patent No. 5,309,217 (3 May 1994).

[174] *Microstatat^{He} and Optistat^{CF-V}*. Oxford Instruments, 1 (1996).

[175] *LT-3-110 and LT-3B-110 technical manual*. APD cryogenics Inc.

[176] H. K. Ng, and Y. J. Wang, in *Physics Phenomena at High Magnetic Field-II*, edited by Z. Fisk, L. Gor'kov, D. Meltzer, and R. Schrieffer (World Scientific, Singapore, 1995).

[177] G. -F. Li, *FTIR Spectroscopic Studies of Spin-Peierles Materials*, Master's Thesis, State University of New York at Binghamton, 1997.

[178] Z. -T. Zhu, *Spectroscopic Studies of Charge Density Wave Bronzes and Fullerene Polymers*, Ph.D Dissertation, State University of New York at Binghamton, 2001.

[179] Y. Kim, Y. Ma, A. Imambekov, N. G. Kalugin, A. Lombardo, A. Ferrari, J. Kono, and D. Smirnov, Phys. Rev. B **85**, 121403(R) (2012).

[180] J. L. Manson, C. R. Kmety, A. J. Epstein, and J. S. Miller, Inorg. Chem. **38**, 2552 (1999).

[181] P. Jensen, S. R. Batten, G. D. Fallon, B. Moubaraki, K. S. Murray, and D. J. Price, Chem. Commun. 177 (1999).

[182] J. A. Schlueter, *et al.* Unpublished results.

[183] B. Hammer, L. B. Hansen, and J. K. Norskov, Phys. Rev. B **59**, 7413 (1999).

[184] S. J. Clark, M. D. Segall, C. J. Pickard, P. J. Hasnip, M. I. J. Probert, K. Refson, and M. C. Payne, Z. Kristallogr. **220**, 567 (2005).

[185] H. J. Monkhorst, and J. D. Pack, Phys. Rev. B **13**, 5188 (1976).

[186] K. Refson, S. J. Clark, and P. R. Tulip, Phys. Rev. B **73**, 155114 (2006).

[187] G. Kresse and J. Hafner, J. Phys. Rev. B **47**, 558 (1993).

[188] G. Kresse, and J. Furthmüller, Comput. Mater. Sci. **6**, 15 (1996).

[189] G. Kresse, and J. Furthmüller, Phys. Rev. B **54**, 11169 (1996).

[190] J. P. Perdew, K. Burke, and M. Ernzerhof, Phys. Rev. Lett. **77**, 3865 (1996).

[191] T. V. Brinzari, P. Chen, Q. -C. Sun, J. Liu, L. -C. Tung, Y. J. Wang, J. Singleton, J. A. Schlueter, J. L. Manson, M. -H. Whangbo, A. P. Litvinchuk, and J. L. Musfeldt. *In preparation.*

[192] P. Gegenwart, J. Custers, C. Geibel, K. Neumaier, T. Tayama, K. Tenya, O. Trovarelli, and F. Steglich, Phys. Rev. Lett. **89**, 056402 (2002).

[193] T. Fries, Y. Shapira, F. Palacio, M. C, Morón, G. J. McIntyre, R. Kershaw, A. Wold, and E. J. McNiff, Jr., Phys. Rev. B **56**, 5424 (1997).

[194] M. Kuhn and R. Mecke, Chem. Ber. **94**, 3010 (1961).

[195] H. Köhler, A. Kolbe, and G. Lux, Z. anorg. allg. Chem. **428**, 103 (1977).

[196] B. Jürgens, H. A. Höppe, and W. Schnick, Solid State Sci. **4**, 821 (2002).

[197] P. P. M. Meincke, Can. J. Phys **48**, 859 (1970).

[198] G. Hausch, Phys. Stat. Sol. A **18**, 735 (1973).

[199] Y. Nakamura, J. Magn. Magn. Mater. **31-34**, 829 (1983).

[200] S. Kimura, Y. Narumi, N. Terada, Y. Tanaka, M. Iwaki, K. Katsumata, M. Hagiwara, K. Kindo, Z. He, T. Taniyama, M. Itoh, H. Toyokawa, T. Ishikawa, and H. Kitamura, J. Phys. Soc. Jpn. **79**, 043706 (2010).

[201] N. A. Benedek, A. T. Mulder, C. J. Fennie, J. Solid State Chem. and references therein, *in press*.

[202] J. F. Scott, Rev. Mod. Phys. **46**, 83 (1974).

[203] P. Bouvier, J. Kreisel, J. Phys.: Condens. Matter **14**, 3981 (2002).

[204] A. Palewicz, R. Przenioslo, I. Sosnowska, and A. W. Hewat, Acta. Cryst. **B63**, 537 (2007).

[205] X. J. Liu, Y. Moritomo, T. Matsuda, H. Kamioka, H. Tokoro, and S. Ohkoshi, J. Phys. Soc. Jpn. **78**, 013602 (2009).

[206] J. B. Goodenough, *Magnetism and the Chemical Bond* (Wiley, New York, 1963).

[207] A. Escuer, F. A. Mautner, N. Sanz, and R. Vicente, Inorg. Chem. **39**, 1668 (2000).

[208] P. W. Anderson, *Solid State Physics*, edited by F. Seitz and D. Turnbull (Academic Press, New York and London, 1963), Vol. 14, p. 99.

[209] M. -H. Whangbo, H. -J. Koo, and D. Dai, J. Solid State Chem. **176**, 417 (2003).

[210] C. Peng, N. Lee, S. McGill, S. -W. Cheong, and J. L. Musfeldt, Phys. Rev. B **85**, 174413 (2012).

[211] T. V. Brinzari, J. T. Haraldsen, P. Chen, Q. -C. Sun, Y. Kim, L. -C. Tung, A. P. Litvinchuk, J. A. Schlueter, D. Smirnov, J. L. Manson, J. Singleton, and J. L. Musfeldt. *In preparation.*

[212] A. S. Litvinenko, E. A. Mikhaleva, S. V. Kolotilov, and V. V. Pavlishchuk, Theor. Exp. Chem. **46,** 422 (2011).

[213] J. T. Haraldsen and R. S. Fishman, J. Phys.: Condens. Matter **21**, 216001 (2009).

[214] I. W. Johnstone, D. J. Lockwood, G. Mischler, J. R. Fletcher, C. A. Bates, J. Phys. C: Solid State Phys. **11**, 4425 (1978).

[215] W. Frank and P. von Brentano, Am. J. Phys. **62**, 706 (1994).

[216] Manson, J. L. *et al.* unpublished results.

[217] H. Rho, M. V. Klein, and P. C. Canfield, Phys. Rev. B **69,** 144420 (2004).

[218] T. V. Brinzari, P. Chen, L. -C. Tung, Y. Kim, D. Smirnov, J. Singleton, Joel S. Miller, and J. L. Musfeldt, *Accepted* Phys. Rev. B.

[219] L. H. Jones, Inorg. Chem. **2**, 777 (1963).

[220] I. Nakagawa and T. Shimanouchi, Spectrochim. Acta A **26**, 131 (1969).

[221] I. Nakagawa, Bull. Chem. Soc. Jpn. **46**, 3690 (1973).

[222] O. Zakharieva-Pencheva and V. A. Demetiev, J. Mol. Struct. **90**, 241 (1982).

[223] S. -K. Park, C. -K. Lee, S. -H. Lee, and N. -S. Lee, Bull. Korean Chem. Soc. **23**, 253 (2002).

[224] V. M. Miskowski, T. M. Loehr, and H. B. Gray, Inorg. Chem. **26**, 1098 (1987).

[225] A. M. Heyns, J. Mol. Structure, **11**, 93, (1972).

[226] Y. Mathey, D. R. Greig, and D. F. Shriver, Inorg. Chem. **21**, 3409 (1982).

[227] C. M. Hartwig, E. Wiener-Avnear, and S. P. S. Porto, Phys. Rev. B **5**, 79 (1972).

[228] A. Marvilliers, S. Parsons, E. Rivière, J. -P. Audière, M. Kurmoo, and T. Mallah, Eur. J. Inorg. Chem. 1287 (2001).

[229] D. Zhang, H. Wang, Y. Chen, Z. -H. Ni, L. Tian, and J. Jiang, Inorg. Chem. **48**, 11215 (2009).

[230] Y. Narumi, N. Terada, Y. Tanaka, M. Iwaki, K. Katsumata, K. Kindo, H. Kageyama, Y. Ueda, H. Toyokawa, T. Ishikawa, and H. Kitamura, J. Phys. Soc. Jpn. **78**, 043702 (2009).

[231] F. D. Hardcastle and I. E. Wachs, J. Raman Spectrosc. **21**, 683 (1990).

[232] D. Cremer, A. Wu, A. Larsson, and E. Kraka, J. Mol. Model. **6**, 396 (2000).

[233] D. R. Talham, M. W. Meisel, Chem. Soc. Rev. **40**, 3356 (2011).

[234] X. -Y. Wang, C. Avendaño, and K. R. Dunbar, Chem. Soc. Rev. **40**, 3213 (2011).

[235] R. S. Fishman, J. Campo, T. E. Vos, J. S. Miller, *submitted* Phys Rev B.

[236] I. Loa, K. Syassen and R. K. Kremer, Solid State Commun. **112**, 681 (1999).

[237] Z. V. Popović, V. Stergiou, Y. S. Raptis, M. J. Konstantinović, M. Isobe, Y. Ueda, and V. V. Moshchalkov, J. Phys.: Condens. Matter **14**, L583 (2002).

[238] K. Ishida and F. C. Hawthorne, Am. Mineral. **96**, 566 (2011).

[239] G. B. Deacon and R. J. Phillips, Coord. Chem. Rev. **33**, 227 (1980).

[240] S. Brown, J. Cao, J. L. Musfeldt, M. M. Conner, A. C. McConnell, H. I. Southerland, J. L. Manson, J. A. Schlueter, M. D. Phillips, M. M. Turnbull, and C. P. Landee, Inorg. Chem. **46**, 8577, (2007).

[241] G. P. O'Leary and R. G. Wheeler, Phys. Rev. B **1**, 4409 (1970).

[242] M. Loukil, A. Ben Salah, and A. Kabadou, J. Alloys Compd. **L10-L13**, 488 (2009).

[243] M. Matsuda, C. de la Cruz, H. Yoshida, M. Isobe, and R. S. Fishman, Phys. Rev. B **85**, 144407 (2012).

[244] K. Penc, N. Shannon, and H. Shiba, Phys. Rev. Lett. **93**, 197203 (2004).

[245] H. Ueda, H. A. Katori, H. Mitamura, T. Goto, and H. Takagi, Phys. Rev. Lett. **94**, 047202 (2005).

[246] Y. Tokunaga, S. Iguchi, T. Arima, and Y. Tokura, Phys. Rev. Lett. **101**, 097205 (2008).

[247] Y. J. Choi, C. L. Zhang, N. Lee, and S. -W. Cheong, Phys. Rev. Lett. **105**, 097201 (2010).

[248] J. Schnack, M. Brüger, M. Luban, P. Kgerler, E. Morosan, R. Fuchs, R. Modler, H. Nojiri, R. C. Rai, J. Cao, J. L. Musfeldt, and X. Wei, Phys. Rev. B **73**, 094401 (2006).

[249] H. Kageyama, K. Yoshimura, R. Stern, N. V. Mushnikov, K. Onizuka, M. Kato, K. Kosuge, C. P. Slichter, T. Goto, and Y. Ueda, Phys. Rev. Lett. **82**, 3168 (1999).

[250] A. B. Butenko, A. A. Leonov, U. K. Rößler, and A. N. Bogdanov, Phys. Rev. B **82**, 052403 (2010).

Appendix

Appendix A

Supplemental Material for $Mn(dca)_2$

A.1 Variable Temperature Lattice Dynamics

Figure A.1.1 displays the complete infrared spectrum of $Mn(dca)_2$ at 300 and 4.6 K. Our temperature studies demonstrate that several features, for instance, lattice modes at 79 and 108 cm^{-1}, NMnN bend at 165 and NCN bend near 500 cm^{-1}, soften with decreasing temperature, a behavior in contrast to normal lattice contraction. At the same time, ν(CN) modes (excluding the 2324 cm^{-1} feature) and ν(Mn-N) stretching vibrations (Table 4.1) harden at low temperatures, a trend that is different from the increased bond lengths determined by neutron diffraction at 4.6 K. [73] The later suggests that simple correlations between bond lengths and resonance frequencies are not applicable in this material as expected in case of extended solids due to the collective nature and coupling of neighboring vibrational modes. Other effects such as, charge, intermolecular interactions and occurrence of bent bonds seem also to be important in this and other similar cases. [232]

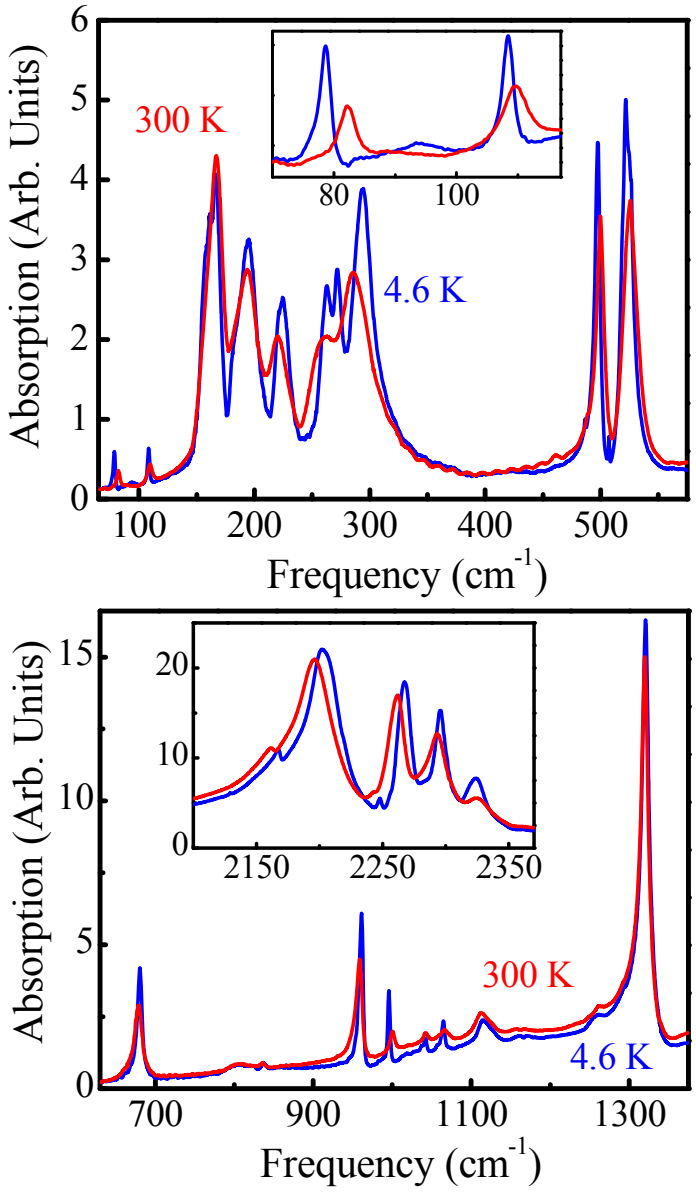

Figure A.1.1: Infrared absorption spectrum at 300 and 4.6 K of $Mn(dca)_2$ along with close-up views of the low frequency lattice modes and C≡N stretches.

A.2 Raman Response of $Mn(dca)_2$

Table A.2.1 summarizes the predicted Raman-active modes of $Mn(dca)_2$ from our dynamics calculations. Frequencies, symmetries and assignments are given. Figure A.2.1 displays the experimental Raman spectrum at 300 K.

Table A.2.1: Theoretically predicted Raman frequencies for $Mn(dca)_2$

Calculated frequency (cm^{-1})	Symmetry	Assignment
82	A_g	lattice mode: MnN_6 counter-rotation in ab plane along c
102, 103	B_{2g}, B_{3g}	lattice mode: MnN_6 counter-rotation along N_{ax}-Mn-N_{ax}, in $\simeq ac$ plane
182	B_{1g}	ligand bands (mostly N motion in-plane and out-of-plane: scissors, rocking, wagging, twisting) + ν_{sym}(Co-N)*
190	B_{2g}	
200	B_{3g}	
209	A_g	
221	B_{1g}	
228	B_{2g}	
229	B_{1g}	
230	B_{3g}	
310	A_g	
335	A_g	
346	B_{1g}	
485, 487	B_{2g}, B_{3g}	δ_{as}(NCN)
504, 506	B_{2g}, B_{3g}	γ_{as}(NCN)
509, 524	A_g, B_{1g}	γ_s(NCN)
647, 648	A_g, B_{1g}	δ_s(NCN)
893, 910	B_{1g}, A_g	ν_s(N-C)
1220, 1222	B_{3g}, B_{2g}	ν_{as}(N-C)
2044, 2046	B_{3g}, B_{2g}	ν_{as}(C≡N)
2111, 2124	A_g, B_{1g}	ν_{sym}(C≡N)

*ν_{sym}(Co-N) stretches correspond to 209 and 229 cm^{-1} modes.

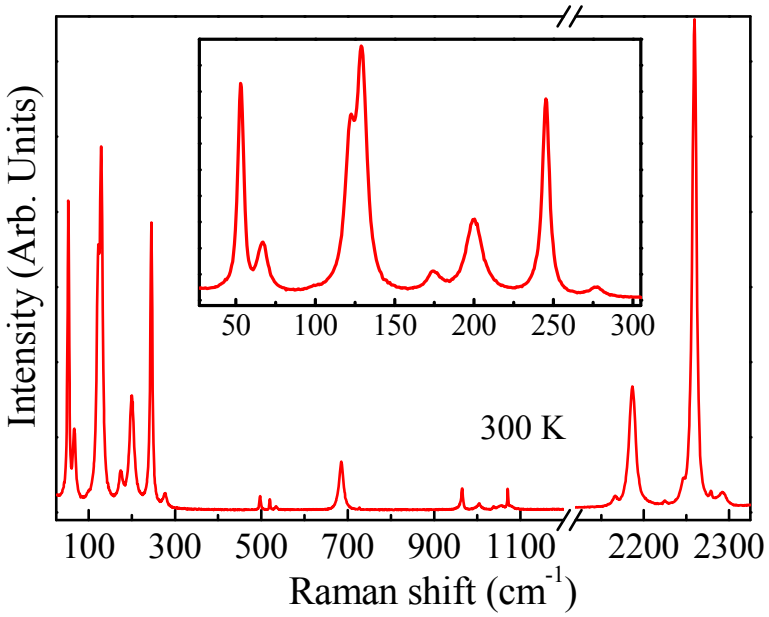

Figure A.2.1: Experimental Raman spectrum of the $Mn(dca)_2$. Inset: Close-up view of the low frequency part of the spectrum. The strong band at 53 cm^{-1} is tentatively assigned to the MnN_6 counter-rotational mode of A_g symmetry.

Appendix B

Supplemental Material for $Co(dca)_2$

B.1 Magnetization and Magnon Calculations

$Co(dca)_2$ has a ferromagnetic ground state and strong spin-orbit coupling. If we model the spin-orbit coupling through an easy-axis anisotropy along the c-axis and include both an external magnetic field and a simple ferromagnetic superexchange ($J \simeq 4$ K (0.35 meV or 2.8 cm^{-1})), then the Heisenberg Hamiltonian can be written as:

$$\mathcal{H} = -\frac{1}{2}\sum_{i\neq j} J_{ij}\mathbf{S}_i \cdot \mathbf{S}_j - D\sum_i \mathbf{S}_{iz}^2 - g\mu_B B\sum_i \mathbf{S}_{iz}, \tag{B.1.1}$$

where $\mathbf{S}_i$ is the local moment on site i, D is the anisotropy energy, and B is the external magnetic field. Due to the strong anisotropy, we treat the system classically and find the magnetization ($M(B)$) for a powder sample to be:

$$M(B) = \tfrac{g\mu_B S}{V}\cos(\theta) = \frac{g\mu_B S}{V}\,\frac{\sqrt{32\,D^2S^2 - 2\,(g\mu_B B)^2\pi^2 + 2\,g\mu_B B\,\pi\,\left((g\mu_B B)^2\pi^2 + 32\,D^2S^2\right)^{1/2}}}{8DS}. \tag{B.1.2}$$

Equation [B.1.2] was used to fit the experimental magnetization below 10 T to obtain $D = 12 \pm 4$ cm^{-1}. Fits to higher field probe the contribution of additional (higher lying) states.

By ignoring quantum fluctuations, we determine the magnon energies within a mean-field approximation and evaluate the Hamiltonian using a Holstein-Primakoff expansion. [213] For the ferromagnetic phase on a cubic lattice, the magnon dispersion ω_m along the a direction is given by:

$$\omega_m = 16JS\left[1 - \cos\left(\frac{k_a a}{2}\right)\right] + 2DS + g\mu_B B. \tag{B.1.3}$$

In the case of Raman spectroscopy (at $k_a = 0$), the magnon energy is given by $\omega_m = 2DS + g\mu_B B$ and $\Delta\omega_m/\Delta B = g\mu_B \simeq 2.5$ cm^{-1}/T. Thus, the zero-field value for the magnon at $k_a = 0$ is found to be 12 ± 4 cm^{-1}.

B.2 Electronic vs. Magnetic Models of ω^* in the Magneto-Raman Response of Co(dca)$_2$

To reveal the nature of the strongly field-dependent feature (ω^*) in the magneto-Raman spectrum of Co(dca)$_2$, we considered both electronic and magnetic coupling models. As described in the main text, the electronic model assigns ω^* to a Co^{2+} crystal field excitation and invokes an electron-phonon coupling mechanism to reveal it. The electronic origin of ω^* is consistent with energetic considerations and temperature dependence of the magneto-Raman response (Fig. B.2.1 and Fig. 5.3 (c) main text). A second candidate mechanism involved assignment of ω^* as hybrid magnon-phonon excitation. Although the experimental evidence argues against a magnetic origin, we summarize this approach here for the interested reader.

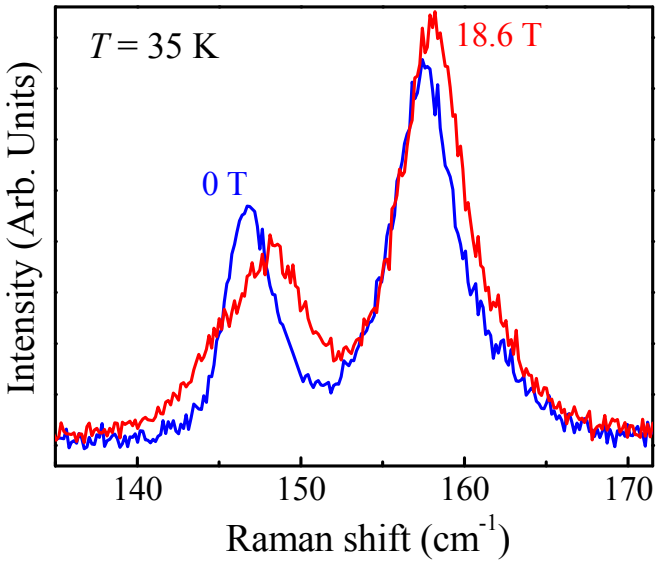

Figure B.2.1: An example of the 35 K Raman response at $B = 0$ and 18.6±0.1 T, clearly showing the 147 cm^{-1} perturbed phonon at high field. The latter is the result of phonon interaction with the resonating field dependent structure that persists well above 9 K Curie temperature. This behavior clearly rules out any magnetic origin of ω^* and supports our assignment of an electronic excitation.

To analyze the possibility of a magnetic origin of ω^*, we also tested a magnon-phonon coupling mechanism. In this picture, the magnon-phonon energy ω_{mp} can be described as a perturbation from the normal phonon energy ω_p by a coupled magnon. This is described as:

$$\omega_{mp} = \omega_p + c\ \omega_m, \tag{B.2.1}$$

where ω_m is the magnon energy and c is the coupling constant. As discussed in the previous section, we already have a prediction for ω_m. The coupling constant and the corresponding phonon energy can be found from the field-dependence of ω^*. By examining the change in position with magnetic field, we find that:

$$\frac{\Delta\omega_{mp}}{\Delta B} = c\frac{\Delta\omega_m}{\Delta B}. \tag{B.2.2}$$

If this mechanism is operative in $Co(dca)_2$, measurements should reveal the magnon-

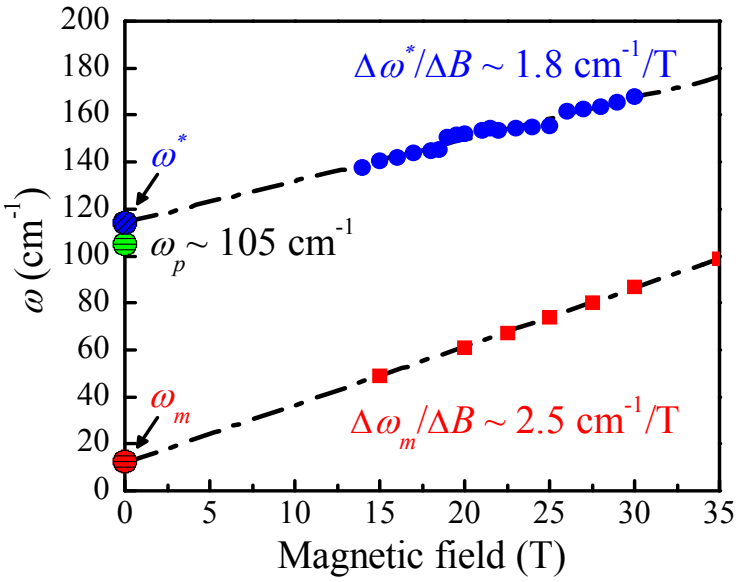

Figure B.2.2: The experimental values of ω^* (circles) and simulated (square) $\omega(k_a = 0)$ as a function of B. The striped circles at $B = 0$ T denote the zero-field values for the predicted magnon (red), hypothetical magnon-phonon (blue), and the 105 cm^{-1} phonon needed to make this model work (green).

phonon energy, its changes with field, the signature of the unperturbed phonon, and of course, the magnon itself.

Let's compare the predictions of the magnetic model to our experimental findings. The Raman spectra show that $\Delta\omega^*/\Delta B = g\mu_B \simeq 1.8$ cm^{-1}/T. Assuming $\omega^* = \omega_{mp}$ and using Eq. [B.2.2], this corresponds to a coupling constant of $\simeq 0.72$. From the extrapolated zero-field value for the ω^* (114±5 cm^{-1}) and magnon (12±4 cm^{-1}) energies, the coupled phonon energy should be 105±6 cm^{-1} (Fig. B.2.2). There is, however, no Raman-active peak at or near that energy. The closest available phonons are located near 66 and 52 cm^{-1}, incompatible with the extracted 105±6 cm^{-1} (Fig. 3.13(d) (main text)). Although infrared spectra reveal a weak lattice mode near 102 cm^{-1} (Fig. B.4.1), ungerade symmetry of this vibration prevents mixing with gerade symmetry magnons and subsequent mixing with Raman-active phonons. The temperature dependence of ω^* (Fig. 3(c) in the main text and Fig. B.2.1), specifically

the lack of sensitivity to the ordering temperature and the persistence well above the Curie temperature, is also inconsistent with its assignment as a magnon-phonon excitation. This is the strongest evidence against a magnon-phonon coupling picture and is in agrement with heat capacity studies that indicate negligible short range spin correlations above $\simeq$15 K. [79]

B.3 Symmetry Analysis of Low-Lying Co^{2+} Electronic Excitations

To complement our discussion on Raman activity of the low-lying Co^{2+} electronic excitations we demonstrate group theory analysis for the formal C_{2h} site symmetry of the Co^{2+} ion. Figure B.3.1 shows the corresponding energy level diagram and Table B.3.1 demonstrates the symmetry of plausible $(\Gamma_3 + \Gamma_4) \rightarrow (\Gamma_3 + \Gamma_4)$ excitation. According to this analysis the low-lying excitations within the ${}^4T_{1g}$ term are Raman allowed in all polarizations, the finding that is equivalent to the case of D_4 symmetry approximation (Table 5.2 (main text)).

Table B.3.1: Symmetry analysis for the low-lying Co^{2+} electronic excitations

Direct product	C_2' site symmetry	D_{2h} crystal symmetry
$(\Gamma_3 + \Gamma_4) \otimes (\Gamma_3 + \Gamma_4)$	$2\Gamma_1(A') \oplus 2\Gamma_2(B')$	$A_g \oplus B_{1g} \oplus B_{2g} \oplus B_{3g}$

Raman tensor for D_{2h} symmetry: $A_g + B_{1g} + B_{2g} + B_{3g}$

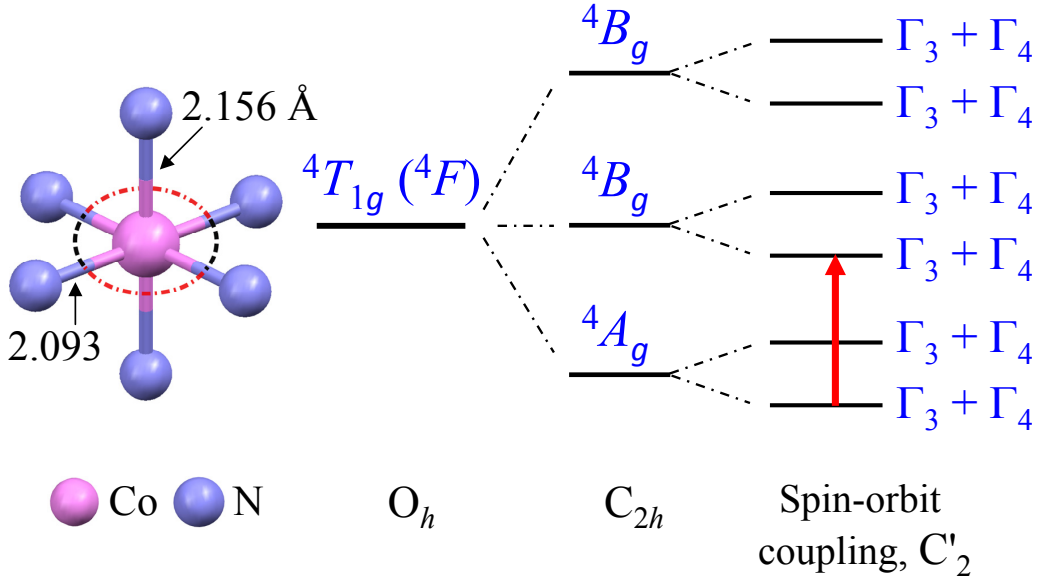

Figure B.3.1: Schematic energy level diagram for the Co^{2+} ion demonstrating the combined effect of symmetry lowering and spin-orbit coupling on the $^4T_{1g}$ ground state in the octahedral environment. Deviation from the D_{4h} site symmetry arises from nonequivalent local angles around Co^{2+} ion (as indicated by red and black). The arrow indicates a plausible Raman-active low energy excitation.

B.4 $Co(dca)_2$ Infrared Response Through the 9 K Magnetic Ordering Temperature

Figure B.4.1 displays the full infrared spectrum of $Co(dca)_2$. As expected from symmetry considerations, the overall response is similar to that of isostructural $Mn(dca)_2$.

The variable temperature response of $Co(dca)_2$ allowed us to investigate vibrational property changes through the magnetic ordering transition. High and low temperature spectra are presented in Fig. B.4.1, and Fig. B.4.2 shows an example of peak position vs. temperature for the 317 cm^{-1} ligand band (Table 5.1 (main text)). This particular phonon hardens gradually with decreasing temperature. No anomalies in this or any other spectral feature are observed through the 9 K ferromagnetic transition indicating that long range ordering is established without any major local lattice distortions. Interestingly, several features, for instance the Co displacement modes at 102 and 133 cm^{-1}, the NCN bends at 502 and near 527 cm^{-1}, and a combination band at 995 cm^{-1} soften with decreasing temperature, a trend that is opposite to normal lattice contraction and similar to the situation in $Mn(dca)_2$. This behavior may be indicative of angular relaxation or alternatively, a more complex dependence of the phonon frequency where besides bond lengths/angles other contributions such as coupling to neighboring modes, charge effects and/or intermolecular forces must be taken into account.

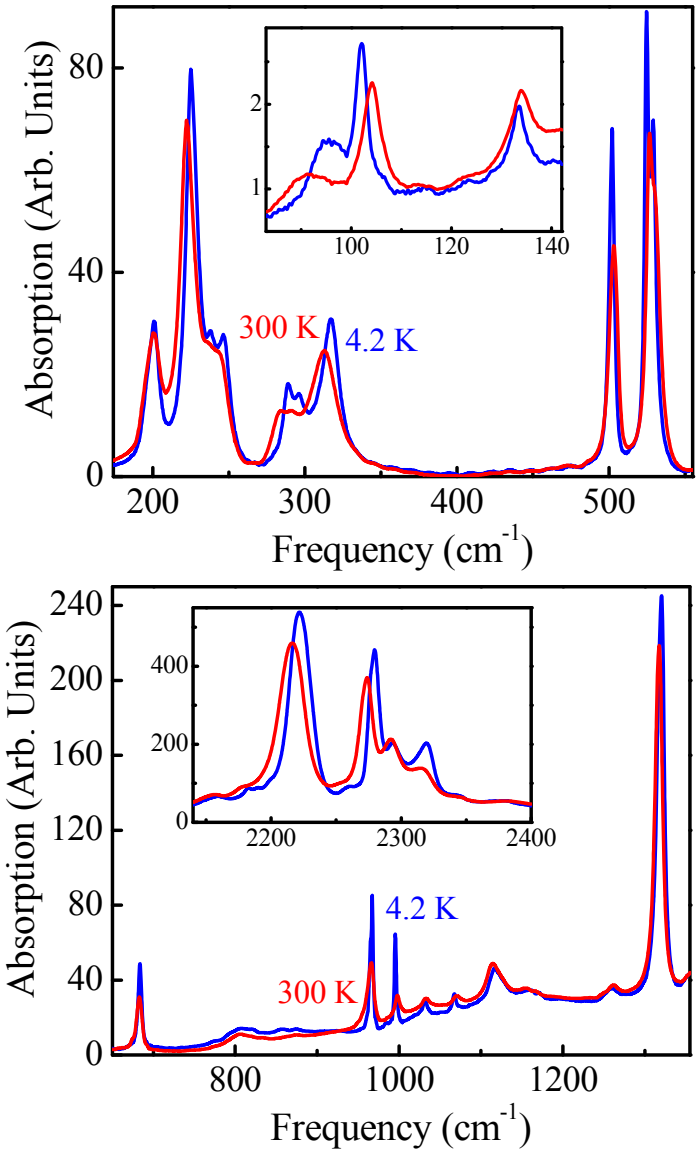

Figure B.4.1: Infrared spectrum of $Co(dca)_2$ at 300 and 4.2 K.

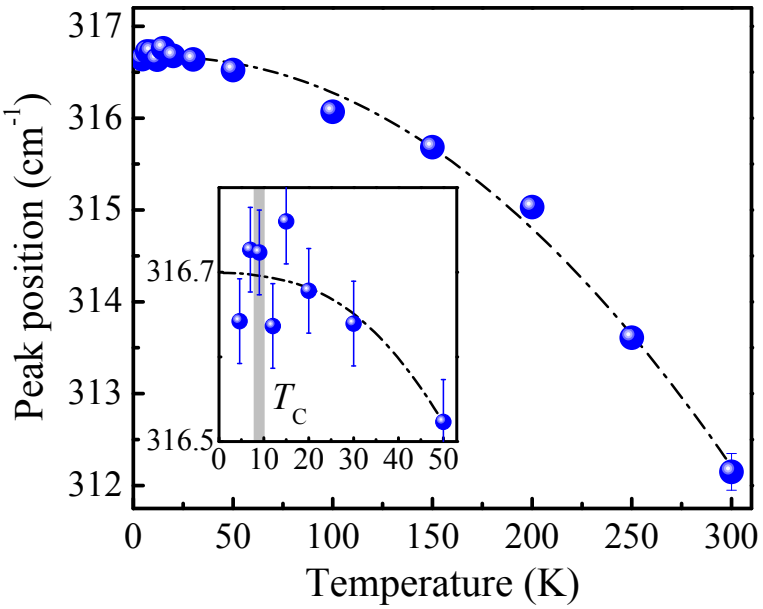

Figure B.4.2: Temperature dependence of the 317 cm^{-1} ligand phonon. Inset: Close-up view near the 9 K ferromagnetic transition. No phonon anomalies due to magnetic ordering transition (gray vertical line) are observed within our sensitivity. Dashed lines guide the eye.

B.5 Analysis of the Field-Induced Spectral Changes: Integrated Absorption Differences vs. Frequency Shifts

Figure B.5.1 compares the integrated absorption difference and frequency shift data for the infrared-active 2294 cm^{-1} ν(CN) stretching mode of $Co(dca)_2$. The field-dependent trends are identical within error bars indicating that (i) either quantity can be used to track high field changes and that (ii) the dominant contribution to the absorption difference spectrum ($\Delta\alpha$) comes from a field-induced frequency shift. ν(CN) displays the largest field-dependent change, $|\Delta\alpha|/\alpha \simeq 6$ % and $|\Delta\omega| \simeq 1$ cm^{-1}, making it a good choice for testing (and potentially distinguishing) the two approaches. We find, however, that normalized $|\Delta\alpha|$ and $|\Delta\omega|$ carry equivalent information and that the former is superior when frequency shifts are small. Other

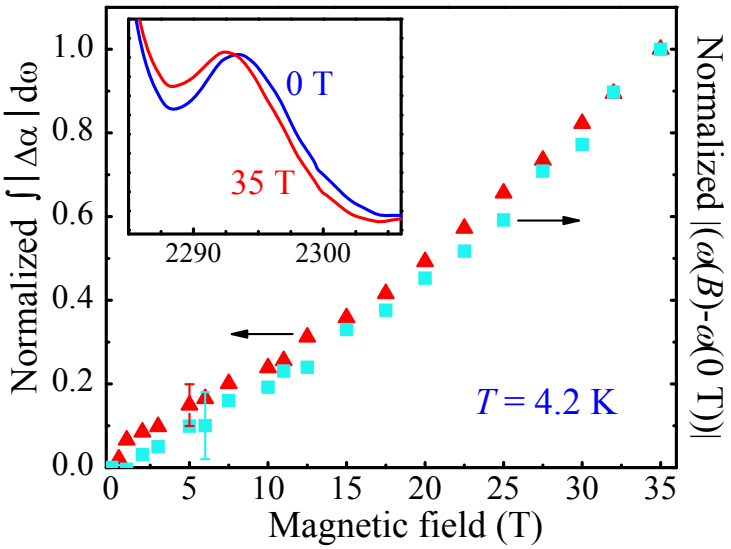

Figure B.5.1: Comparison of the integrated absorption difference and frequency shift data for the ν(CN) stretching mode of $Co(dca)_2$. These quantities are normalized to 35 T and display similar behavior with field. Inset: Close-up view of the absolute absorption at $B = 0$ and 35 T.

modes display similar behavior although the magnitude of their frequency shifts is smaller (making the error bars much larger). We therefore use normalized absorption difference in this work to quantify magneto-infrared effects.

Vita

Tatiana Brinzari was born in Chisinau, Moldova. She attended Moldova State University between 2000 and 2006, where she received Licentiate (B.S.) and M.S degrees in Chemistry. In Spring 2007, she entered the graduate program at the Department of Chemistry, University of Tennessee, Knoxville. She joined Dr. Janice Musfeldt's group to begin research in the field of spectroscopic investigations of complex materials, such as transition metal oxides and magnetic molecular solids. Tatiana Brinzari received a Doctor of Philosophy Degree in Chemistry from the University of Tennessee in Fall 2012.